Quantum measurement backaction and upconverting microwave signals with mechanical resonators

by

R. W. Peterson

B.S., University of Minnesota, 2011

M.S., University of Colorado, 2014

A thesis submitted to the

Faculty of the Graduate School of the

University of Colorado in partial fulfillment

of the requirements for the degree of

Doctor of Philosophy

Department of Physics

2017

This thesis entitled:
Quantum measurement backaction and upconverting microwave signals with mechanical resonators
written by R. W. Peterson
has been approved for the Department of Physics

_____

Prof. Cindy Regal

_____

Prof. Konrad Lehnert

Date _____

The final copy of this thesis has been examined by the signatories, and we find that both the content and the form meet acceptable presentation standards of scholarly work in the above mentioned discipline.

Peterson, R. W. (Ph.D., Physics)

Quantum measurement backaction and upconverting microwave signals with mechanical resonators

Thesis directed by Prof. Cindy Regal

The limits of optical measurement and control of mechanical motion are set by the quantum nature of light. The familiar shot noise limit can be avoided by increasing the optical power, but at high enough powers, the backaction of the randomly-arriving photons' radiation pressure can grow to become the dominant force on the system. This thesis will describe an experiment showing how backaction limits the laser cooling of macroscopic drumhead membranes, as well as work on how these membranes can be used to upconvert microwave signals to optical frequencies, potentially preserving the fragile quantum state of the upconverted signal.

Dedication

To my parents Wendy and Bruce, and my sister Amelia

Acknowledgements

My years in graduate school at JILA have been both tremendously challenging and rewarding. I have many to thank for their support, guidance, and friendship over the years, extending far beyond when I first came to Boulder six years ago. I would begin by thanking my parents for teaching me the virtues of honesty and patience, and allowing me the profound freedom to make my own choices as a child. My family has always supported my goals and accomplishments—I have always felt that I've had the wind at my back. Of my years in high school, I am most grateful to my teachers Charlie Leibfried and Jim Stellmaker, who showed me the beauty of music, as well as the power of consistent practice to transform yourself.

I owe my initial development as a researcher primarily to my undergraduate advisor, Shaul Hanany, and his students. From my time in his group, I learned how to work independently, how to be uncompromising on details, and how to radically reject Minnesota nice. I also thank Tamara Diedrich for the chance to try geology research and fieldwork at NRRI in Duluth, and Edwin Kan for the introduction to nanofabrication at the wonderful Cornell cleanroom.

I could not be happier with my decision to come to Boulder, and the opportunity to work in Cindy's lab. Besides learning optics, I've learned from her how to tell a story with data, to both clearly explain results and speak to their broader relevance. I appreciate the trust and freedom she has given me and the rest of the lab, as well as the support we have inevitably required. Tom patiently spent years of his postdoc sharing his arcane knowledge of cavity design, analog electronics, and quantum measurement with me. I am also grateful to the rest of the lab—in the early years Adam, Ben, Brian, and the rest of us fit on one bench. As the lab has grown, seating at

restaurants has become more difficult, though far offset by the pleasure of working with Nir, Tom, Ran, Oliver, and Max, as well as Mark, Yiheng, Tobias, and the rest on the atom experiment. It has also been a pleasure to know and work with some of the undergraduates in the lab, among them Christine, Alec, Josh, Randall, and Gabriel.

My work on microwave upconversion has also given me the opportunity to work closely with Konrad and his group, from whom I have received an appreciated second dose of wisdom. I thank Reed, Brad, Pete, Tim, and Andrew for teaching me the nuances of microwave photons, filling the fridge over the weekend, and above all being a pleasure to work with. The JILA shops have provided essential help throughout my PhD; the upconversion experiment has provided them with perhaps the most unresonable and technically demanding projects of my time here, which they have nevertheless completed with their renowned skill.

The years in graduate school would not have been superlative without my friends and their companionship, both in Boulder and Duluth. I cherish our times together, including the night hikes, clandestine home renovation, daily lunch in the H-Bar, sailing Lake Superior, and canoeing the Boundary Waters. I would especially single out those that suffered the most: my roommates in Beefcake Manor during the four years I spent there. Finally, I thank my wife Charlie for her support, especially in the final months I spent writing up while while we planned our future.

Contents

Chapter

Tables

Table

Figures

Figure

Chapter 1

Introduction

> "Yet even though light is so weightless we have given its name to that condition, it presses against what it falls on, just as wind, which we cannot see, pushes the arms of a mill.
>
> *The Book of the New Sun*, Gene Wolfe

The past several years have seen tremendous progress in cavity optomechanics, the field of study concerning the effect of light's radiation pressure on mechanical motion. One of the major themes underlying this progress is the arrival of optomechanical systems in the quantum regime. This encompasses both the quantum nature of the optical measurement process itself, as well as quantum motion of the mechanical resonators. The arrival of optomechanical systems with parameters sufficient to encounter these regimes allowed for experimental demonstration of many longstanding predictions of how quantum mechanics can both limit and enhance measurement [1, 2]. There has been advancement along several fronts, from fundamental studies of the quantum mechanics of position measurement, to applications of quantum measurement in sensitive position detection such as gravitational wave observatories, to the use of mechanical motion as a link between quantum systems across the electromagnetic spectrum, potentially linking future quantum networks of superconducting qubits, atoms, and ions.

From one point of view, the recent achievements of cavity optomechanics bring the long-standing and exquisite quantum control over atoms and ions to a new regime: tangible, macroscopic objects whose vibrational modes behave in ways that are manifestly quantum. One of the

membrane resonators used in our experiments is shown in Fig. 1.1, illustrating its visible size. In one of the experiments discussed in this thesis, a vibrational mode of a drumhead resonator was coupled so strongly to the light field controlling it, that its link to its physical environment became negligible as it entered into thermal equilibrium with the quantum noise of the light bouncing off of it [3]. In atomic physics, this corresponds to Doppler-limited cooling, something experimentally demonstrated 31 years previously [4]. The relation of the field of optomechanics to earlier work in atomic physics on photon recoil and position measurement is explored in detail in Ref. [5]. In addition to bringing quantum control to macroscopic objects, a unique feature of radiation pressure is that it is fundamentally a non-resonant process. Photons, no matter their frequency, all carry momentum. Though visible or near-infrared photons may carry tens of thousands of times as much energy than a microwave-frequency photon, both optical and microwave light have been used in the most state-of-the-art experiments in optomechanics. Practically speaking, both the mechanical mode and the light are engineered into resonant structures to enhance the interaction, but the freedom to choose the nature of these structures allows for many opportunities. This is in contrast to atoms and ions, whose resonances are set by nature. The uniformity of these resonances allow for applications like ultraprecise clocks, explorations of many-body physics, and building near-ideal quantum systems from the ground up [6, 7, 8], but these experiments must use wavelengths particular to the atom or ion species to address them. In our case, the choice of wavelength was partially based on existing availability of low-noise laser components at 1064 nm. Different priorities might suggest other wavelengths, such as the broad tunability of a Ti:Sapphire laser from 700 to 1000 nm, or operation in the telecom band at 1550 nm to benefit from the absorption minimum in silica fiber-optic cables for networking applications. In this thesis, we also describe work where our membrane resonator is coupled to microwave light at 7 GHz, which is in the band of operation of superconducting circuits, a promising platform for quantum information [9, 10, 11].

The story of optomechanics in its current form begins in early studies of gravitational wave detection. The so-called ponderomotive effect of light, that is, its ability to damp the periodic motion of a mechanical object reflecting or absorbing electromagnetic radiation, was first explored

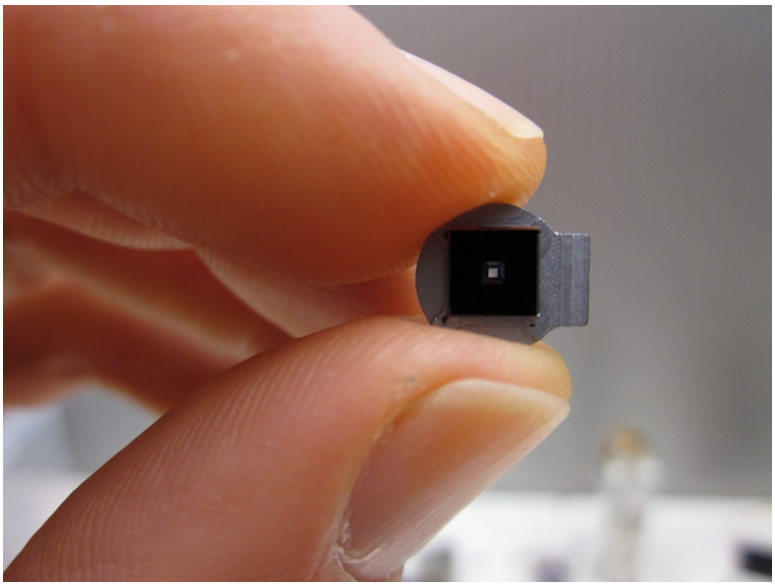

Figure 1.1: The 0.5 mm-sized gray square in the center of the Si chip is the transparent, 50 nm thick Si_3N_4 membrane typical of those whose motion is studied in this thesis. Photo credit: Tom Purdy

and experimentally measured in the late 1960s [12, 13]. However, an example of an optomechanical resonator is found earlier in history. In 1945, the Soviets presented a wooden carving of the Great Seal of the United States to the American ambassador in Moscow (Fig. 1.2). Inside it, a diaphragm coupled to a UHF cavity, designed by Leon Theremin, was used as a passive bug to record the ambassador's conversations [14]. The vibrations of the diaphragm modulated the cavity's resonant frequency, thereby transmitting sounds in the room via radio waves if the cavity was driven by a distant UHF antenna. It is an interesting coincidence that the first scientifically published work in the 1960s also used UHF resonators. Today, little work is done below microwave frequencies, because even at the lowest practical cryogenic temperatures (¡100 mK in a dilution refrigerator), the electromagnetic modes would have appreciable thermal excitation, precluding any quantum effects.

Perhaps the highest-profile results of optomechanics in the quantum regime were the demonstrations of sideband cooling of a mechanical mode into its quantum ground state, using microwave and optical cavities, respectively [15, 16]. By lowering the average temperature of the mechanical mode, both experiments prepared a mechanical resonator in its ground state of motion with greater than 50% probability. These results did not approach the quantum limit of the cooling process itself, which is limited by the ever-present shot noise fluctuations of light. My work demonstrated cooling to this quantum backaction limit, where the light's coherent interaction with mechanical motion has a minimum effective temperature [3].

In general, the results during my time as a graduate student demonstrate interferometric measurements made at the quantum limit. The observation of radiation pressure shot noise (RPSN)—the fluctuating force of the randomly-arriving photons that drives additional motion during a position measurement—represented the resolution of a series of theoretical questions into the quantum limits of optical interferometers long thought to be relevant to gravitational wave detectors [17, 18, 19]. Subsequent work in our group showed that the correlations naturally induced by RPSN could be used to reduce the quantum noise of light below the shot noise limit, generating so-called squeezed light [20, 21, 22]. The first demonstrations of optomechanically squeezed light

Figure 1.2: Bug inside wooden replica of the great seal. Photo credit: Austin Mills, CC BY-SA

demonstrated noise a few percent below the usual vacuum noise level, while our demonstration increased this to 32% below vacuum noise. Squeezed light can be used as a resource to improve sensitivity beyond usual quantum limits, as has been demonstrated in gravitational wave observatories [23, 24]. These demonstrations used nonlinear media such as KTP to generate squeezed light, the technology where the highest levels of squeezing (15 dB, or 97% below vacuum noise) have been reported [25, 26]. However, optomechanically squeezed light is uniquely powerful because it can enhance the measurement of the same mechanical object that generated it, a situation relevant to gravitational wave detectors limited by RPSN [27, 28, 29]. Our most recent result demonstrates how such correlations can be exploited by modifying the readout phase of the measurement to improve sensitivity, a technique called variational readout [30, 28, 31]. Chapter 6 describes my measurement of the quantum backaction limit of laser cooling, and summarizes the utility of measurements of RPSN, squeezed light, and other previous quantum measurement results for calibrating and understanding optomechanical systems in the quantum regime.

Another focus during my time in graduate school was developing an integrated device coupling mechanical motion to both microwave and optical fields, and the progress towards making it operate in the quantum regime. A quantum link between microwave and optical frequencies would enable long-distance quantum networks of superconducting circuits, since quantum states at microwave frequencies cannot survive outside of a dilution refrigerator's base temperature of 10 mK. Optically encoded quantum states, such as single photons, comfortably exist at room temperature, and applications can leverage the technologies available in visible and near-infrared wavelengths. In particular, the minimum of absorption in silica at 1550 nm and low-noise photonic technologies enable long-distance transmission and detection [32], while atomic and ionic systems could form long-lived quantum memories [33, 34]. These technologies have come together in small initial demonstrations, and could one day constitute more ambitions quantum networks [35, 36, 37, 38, 39]. Mechanical resonators form a unique link between microwave and optical frequencies because the radiation pressure force of light works equally in either regime. Unlike nonlinear materials used as electro-optic modulators (a common way to convert classical electrical signals into light), high

efficiencies are readily attainable [40, 41, 42, 43]. Our approach of integrating existing microwave and optical experimental systems to share a common mechanical element led to quick progress and is described in Chapter 7.

Aside from detailing experimental results, this thesis begins with theoretical background on the optomechanical interaction (Chapter 2), employing a matrix formalism to conveniently and elegantly solve the equations of motion, especially in the case of the microwave to optical converter, where many input and output modes intractably multiply the number of equations to keep track of. Following that is a discussion of optical cavities, including relevant calculations and measurements (Chapter 3). A one-dimensional model for calculating the effects of our vibrating membrane is also presented, with representative calculations and measurements.

An important aspect of my graduate work has been the design and construction of the optomechanical devices used in our experiments. They are high-finesse optical cavities with membrane resonators interferometrically aligned and epoxied into place between the cavity mirrors. Because our experiments operate inside cryostats at temperatures between 30 mK and 4 K, these cavities must be designed to survive thermal cycling while maintaining precise alignment between the two mirrors and the membrane. This thesis devotes two chapters to the history and evolution of our optomechanical cavity designs. The first, Chapter 4, describes the cavities used in our purely optical experiments, which incorporate the newest design concepts. The second, Chapter 5, describes the optical design of the devices used to couple microwave and optical frequency light, which consist of membrane resonators coupled to both optical light and microwave fields. Benefiting from earlier experimentation in the purely optical designs, these hybrid devices also incorporate design features unique to their purpose, such as coupling the microwave circuit to transmission lines for excitation and readout without sacrificing interferometric alignment of the membrane resonator.

Chapter 2

Optomechanical theory

My goal is to present a minimally self-consistent description of the optomechanical theory needed to explain the results in this thesis. In particular, I do not wish to compete with the several references available at various levels of technical detail that I have personally found useful [44, 45, 46]. I will present a derivation in truncated form, via the use of matrix techniques to represent and solve the differential equations. This contrivance allows for rapid calculation using symbolic or numerical computer packages. It produces exact (up to the assumptions made) expressions, which are typically much more unwieldly than the simplified expressions found in most papers, reviews, and theses. However, results such as the quantum backaction limit to laser cooling emerge without any additional derivations. A few demonstrations of this, and the references to corresponding literature results should serve to demonstrate the power of this technique. I would like to acknowledge Joe Kerckhoff for introducing this representation to those of us working on optomechanics in Boulder, and demonstrating its power [47, 48]. It was essential for our work on microwave to optical upconversion, if only because the algebra describing so many modes was obviously intractable [42].

While there are multiple approaches to deriving the optomechanical interaction and the results of dynamical backaction, including classical descriptions, I will present the standard Hamiltonian formalism. This can be used to describe the dynamics of optomechanical systems in both classical and quantum regimes. The optical and mechanical modes used in this derivation are completely generic. While initially referring to an optical cavity with a vibrating dielectric membrane,

they apply equally well to microwave LC circuits with mechanically compliant components, as will be discussed later in the chapter.

2.1 Derivation of the equations of motion

An optomechanical system is described by two harmonic oscillator modes, describing the light field in the cavity, and the mechanical mode of the vibrating object. Canonically, one of the end mirrors is assumed to move, although the formalism is identical to our case of a thin dielectric membrane, or indeed one of the many optomechanical systems. A schematic diagram of the following modes are shown in Fig. 2. Let the annihilation (creation) operators for these fields be a ($a^\dagger$) and c ($c^\dagger$), respectively. The radiation pressure of light is proportional to the intensity, thus the interaction Hamiltonian is the number operator $a^\dagger a$ multiplied by the position operator $x = x_{\rm zp}(c + c^\dagger)$, where $x_{\rm zp} = \sqrt{\frac{\hbar}{2m\omega_{\rm m}}}$ is the zero-point motion of the mode of effective mass m and frequency $\omega_{\rm m}$. The strength of the interaction is the optomechanical coupling, which describes how much the resonant frequency of the optical cavity ω_c changes with respect to motion of the mechanical mode, $G = \frac{\partial \omega_c}{\partial x}$. G has a typical scale of MHz/nm in our system. Combined with $x_{\rm zp}$, the optomechanical coupling takes on the more general form $g_0 = G x_{\rm zp}$, which, with units of Hz, can be directly compared to other coupling or dissipation rates in the system (in our system $g_0 \sim 10$ Hz). We can write the Hamiltonian of the system (without dissipation) as

$$H = \hbar\omega_c a^\dagger a + \hbar\omega_{\rm m} c^\dagger c + \hbar g_0 a^\dagger a (c + c^\dagger) \tag{2.1}$$

where constant terms such as the $\frac{1}{2}$ in $\hbar\omega_c(a^\dagger a + \frac{1}{2})$ are omitted [49].

To simplify the interaction, the optical field is linearized by splitting it into a classical amplitude and a remaining fluctuating term, $a \to \alpha + \delta a$. Conceptually, we anticipate that the classical component of the pump will set the scale for the magnitude of the coherent interaction, while the fluctuations will contain the effects of radiation pressure and dynamical backaction on the light. To this end, interaction terms proportional to $|\alpha|^2$ represent dc shifts and can be dropped; terms proportional to $\alpha\delta a$ capture the desired interaction and will be kept; and higher-order terms such

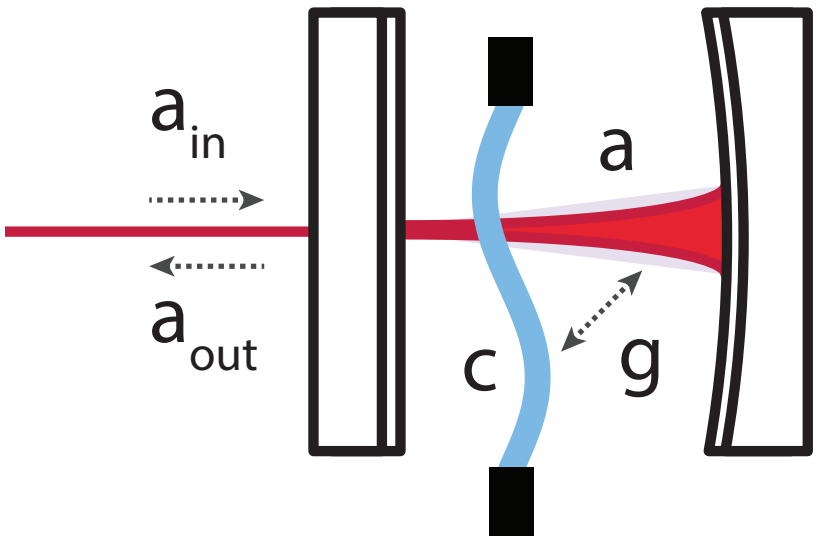

Figure 2.1: Basic diagram of an optomechanical system. The incoming and outgoing light fields are denoted by a_{in} and a_{out}, while the light field in the cavity (confined by the two mirrors) is denoted by a. The membrane's vibrational mode is denoted by c, while the optomechanical coupling between light intensity and mechanical position is denoted by g.

as δa^2 are negligible. It is also convenient to move into a rotating frame at the laser frequency ω_L, giving rise to a detuning $\Delta = \omega_c - \omega_L$. After these adjustments, the Hamiltonian takes the form

$$H = \hbar\Delta\delta a^\dagger \delta a + \hbar\omega_{\rm m} c^\dagger c + \hbar g_0\sqrt{N}(\delta a^\dagger + \delta a)(b + b^\dagger) \tag{2.2}$$

where we introduce the intracavity photon number $N = |\alpha|^2$. At this point, the effects of dissipation, driving, and fluctuations must be taken into account. This is done by moving to the Heisenberg picture, where operators are time-dependent. The resulting Heisenberg-Langevin equations of motion contain input and output operators, representing input fields of vacuum noise, coherent excitation (and for the mechanical resonator, thermal noise), and output fields for modes which will be detected. This yields the equations

$$\delta\dot{a}(t) = -(\kappa/2 + i\Delta)\delta a(t) - ig\sqrt{N}(c + c^\dagger) - \sqrt{\kappa}\delta a_{\rm in}(t) \tag{2.3}$$

$$\dot{c}(t) = -(\Gamma_{\rm m}/2 + i\omega_{\rm m})c(t) - ig\sqrt{N}(\delta a + \delta a^\dagger) - \Gamma_{\rm m} c_{\rm in}(t) \tag{2.4}$$

(as well as their complex conjugates). This forms a complete set of equations of motion, along with input-output relations of the form

$$\delta a_{\rm out}(t) = \sqrt{\kappa}\delta a(t) + \delta a_{\rm in}(t) \tag{2.5}$$

$$\tag{2.6}$$

which states that the input field is almost entirely promptly reflected with $R \approx 1$, and is superimposed with the cavity leakage field. An equivalent relation can be written for $c_{\rm out}$, however for most mechanical systems it is implausible to imagine measuring incoming and outgoing mechanical spectra directly. An exception might be engineered acoustic structures like those used in surface acoustic wave (SAW) devices.

2.2 State-space representation

This set of equations can be written in a condensed matrix representation unimaginatively known as a state space model in the jargon of control theory. (Admittedly, it could be worse. It

could be called ABCD matrix analysis.) Specifically, writing the column vectors

$$\mathbf{a}(t) = (a(t), c(t), a^\dagger(t), c^\dagger(t))^T \tag{2.7}$$

for the internal modes of the system,

$$\mathbf{a}_{\rm in}(t) = (a_{\rm in}(t), c_{\rm in}(t), a^\dagger_{\rm in}(t), c^\dagger_{\rm in}(t))^T \tag{2.8}$$

for the input modes, and

$$\mathbf{a}_{\rm out}(t) = (a_{\rm out}(t), c_{\rm out}(t), a^\dagger_{\rm out}(t), c^\dagger_{\rm out})^T \tag{2.9}$$

for the output modes allows us to represent the equations of motion in the form

$$\dot{\mathbf{a}}(t) = A\mathbf{a}(t) + B\mathbf{a}_{\rm in}(t) \tag{2.10}$$

$$\mathbf{a}_{\rm out}(t) = C\mathbf{a}(t) + D\mathbf{a}_{\rm in}(t) \tag{2.11}$$

where the matrices A, B, C, and D together constitute the system. Their form is given in the last section of the chapter, since we can trivially extend them from the case above (a single-port optical cavity coupled to a single mechanical mode) to a more complicated system of multiport optical and microwave cavities coupled to the same mechanical mode, which will also be discussed below. With the details aside, the following discussion is general to any optomechanical system making the assumptions above.

To proceed, we begin by taking Fourier transforms of the various column vectors, for example

$$\mathbf{a}[\omega] = \int_{-\infty}^{\infty} e^{i\omega t}\mathbf{a}(t)dt \tag{2.12}$$

$$\tag{2.13}$$

There are two approaches to use at this point: sticking with the state space representation allows calculation of a susceptibility

$$\chi[\omega] = (-i\omega I - A)^{-1}B \tag{2.14}$$

satisfying the relation $\mathbf{a} = \chi[\omega]\mathbf{a}_{\rm in}$, or moving to a transfer matrix representation to calculate a transfer function

$$\xi[\omega] = C(-i\omega I - A)^{-1}B + D \tag{2.15}$$

satisfying the relation $\mathbf{a} = \xi[\omega]\mathbf{a}_{\rm out}$.

Now, calculation of operator spectra are straightforward. The spectrum of the internal modes, $S[\omega]$, is given by

$$S[\omega] = \langle \mathbf{a}[-\omega]^\sharp \mathbf{a}[-\omega]^T \rangle \tag{2.16}$$

where $^\sharp$ denotes elementwise conjugation (and ^{T}, as usual, transposition without conjugation). By using the relations between vectors above, this can be written

$$S[\omega] = \chi[-\omega]^\sharp \langle \mathbf{a}_{\rm in}[-\omega]^\sharp \mathbf{a}_{\rm in}[-\omega]^T \rangle \chi[-\omega]^T = \chi[-\omega]^\sharp \Sigma \chi[-\omega]^T \tag{2.17}$$

where we introduce the covariance Σ, containing expectation values of the input noise operators. For example, the mechanical bath, at temperature $n_{\rm th}$, gives $\langle c_{\rm in}[\omega\prime]^\dagger c_{\rm in}[\omega]\rangle = 2\pi\delta(\omega - \omega\prime)n_{\rm th}$ and $\langle c_{\rm in}[\omega']c_{\rm in}[\omega]^\dagger\rangle = 2\pi\delta(\omega - \omega')(n_{\rm th}+1)$. For the optical modes, an equivalent expression is obtained by setting $n_{\rm th} = 0$, corresponding to the situation where only vacuum noise is present. We can calculate the spectrum of the output modes, $S_{\rm out}[\omega]$, equivalently,

$$S_{\rm out}[\omega] = \xi[-\omega]^\sharp \Sigma \xi[-\omega]^T \tag{2.18}$$

Individual elements correspond to the spectra of the various internal or output operators. For example, in the system described for the derivation, $S_{2,2}/2\pi = c[\omega]^\dagger c[\omega]$ is the phonon spectrum of the mechanical mode, which can be integrated over to give the phonon occupation $\bar{n}$.

2.3 Practical calculations: sideband cooling and RPSN

At this point, we can replicate two representative results that illustrate the power of this method. The first is the phonon spectrum for a device in the resolved sideband regime ($2\omega_{\rm m} > \kappa/2$), showing the phonon spectrum as it is damped into its ground state, and continuing until the

strong coupling regime ($g_0\sqrt{N} > \kappa$). Using parameters representative of the first experimental demonstration of ground state cooling (Ref. [15]), we can recreate Fig. 3b in that work (Fig. 2.2). While the specific physics of strong coupling are included in the model, they will not be explained since they are of no further relevance to this thesis. Satisfaction will thus necessarily focus on how straightforward it was to calculate unrelated results using versatile machinery.

The second result is the quantum backaction limit of sideband cooling. By selecting parameters of my result in Ref. [3], which is in the intermediate regime of sideband resolution, the backaction limit clearly appears in a cooling curve (Fig. 2.3) which replicates the result in Fig. 6.7. Both examples represent situations where the classical sideband cooling regime is complicated by additional effects. While they are both, of course, logical consequences of the relatively straightforward theory above, discussing them usually involves bringing in "extra" arguments on top of the classical sideband cooling picture that is typically used to heuristically explain results. Which of these pictures is more useful depends on context. It is fair to observe that when using the matrix formalism, it is difficult to collect and condense analytical expressions which are simplified enough to meaningfully explain what is happening on their own.

For the sake of clarity and explanation, the typical analytical results will also be presented. Perhaps the most relevant to this thesis is the mechanical mode's response to optical damping, resulting in the rate equation

$$\bar{n}(\Gamma_{\rm opt}) = \frac{n_0\Gamma_{\rm m} + n_{\rm ba}\Gamma_{\rm opt}}{\Gamma_{\rm m} + \Gamma_{\rm opt}} \tag{2.19}$$

where the backaction limit $n_{\rm ba}$ is given by the expression

$$n_{\rm ba}(\Delta) = -\frac{(\omega_{\rm m} + \Delta)^2 + (\kappa/2)^2}{4\omega_{\rm m}\Delta} \tag{2.20}$$

which is solely a function of sideband resolution of the cavity. However, this statement belies its origin in shot noise fluctuations which the cavity merely filters to set an effective temperature $n_{\rm ba}$ [50, 51]. In general, one can add additional optical damping terms to the rate equation (Eq. 2.19) if more lasers are incident on the cavity. A prime example is in the case of our radiation pressure shot

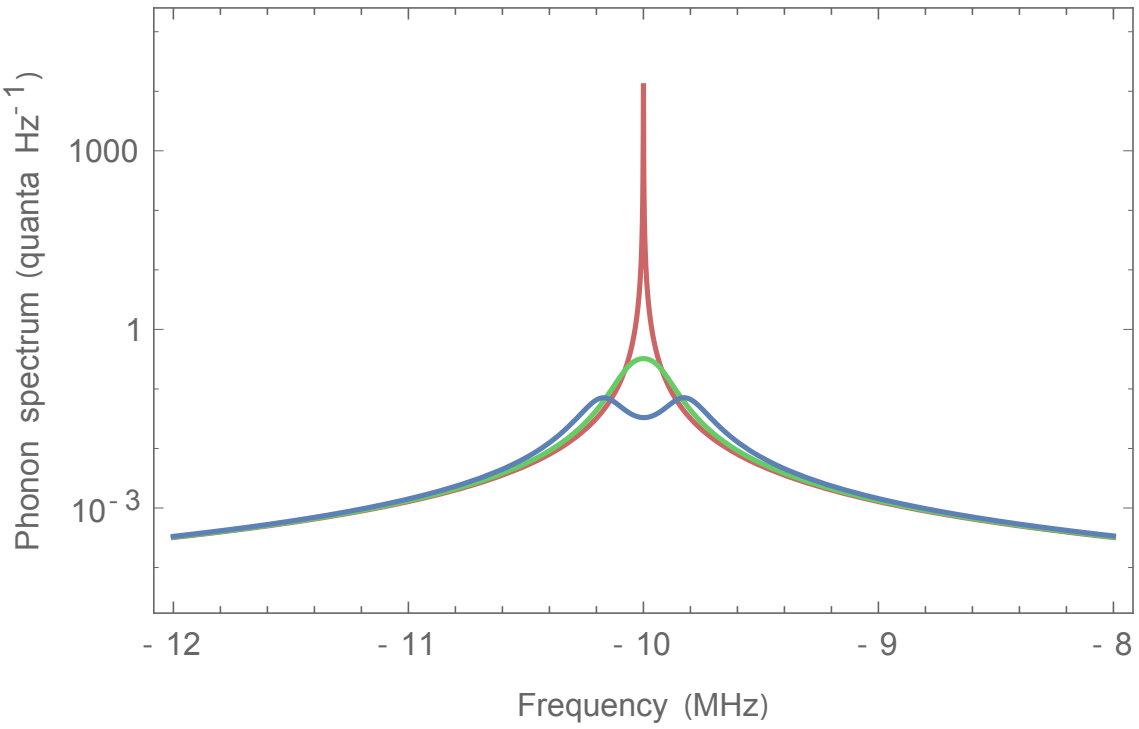

Figure 2.2: Using parameters $\omega_{\mathrm{m}} = 2\pi \times 10$ MHz, $\kappa = 2\pi \times 0.4$ MHz, $\Gamma_{\mathrm{m}} = 2\pi \times 32$ Hz, $g = 2\pi \times 200\sqrt{N}$ Hz, $\Delta = -2\pi \times 10$ MHz, and $n_{\mathrm{th}} = 40$, three selected spectra for $N = \{1, 10^{5.5}, 10^{6}\}$ demonstrating undamped thermomechanical motion (red), damping near the ground state (green), and damping into the strong coupling regime (blue), where the mode hybridization is visible.

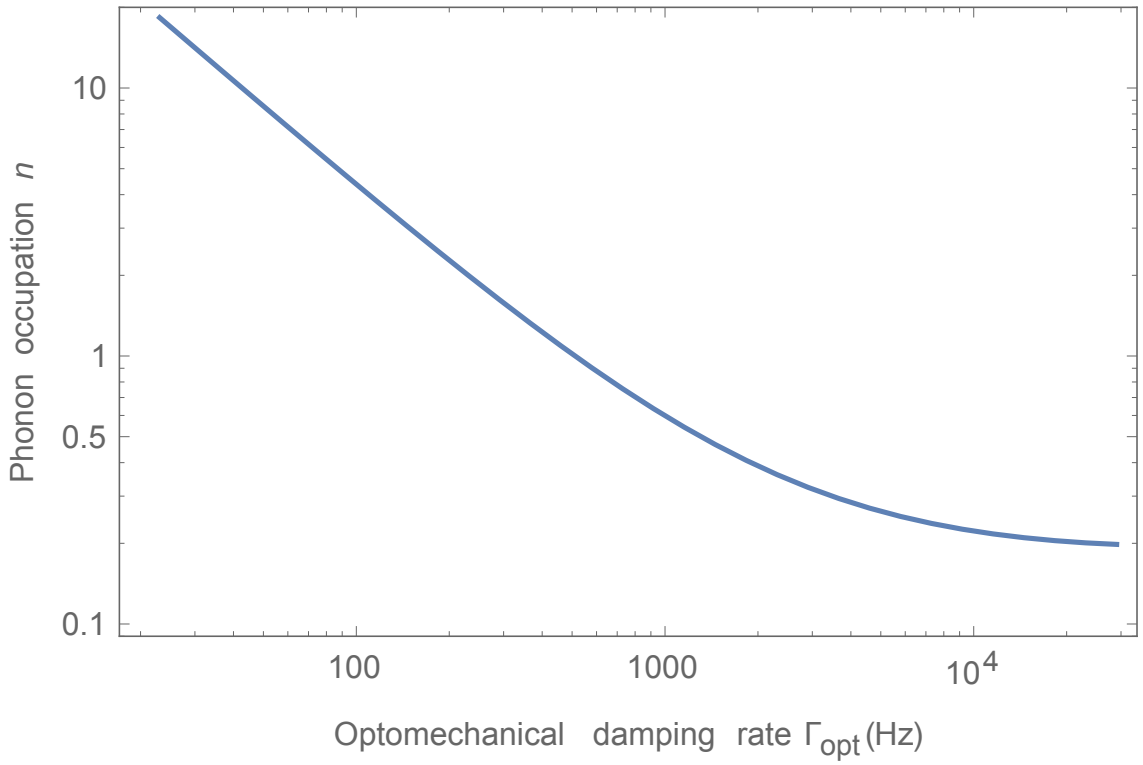

Figure 2.3: Using parameters $\omega_{\rm m} = 1.48\pi \times 10$ MHz, $\kappa = 2\pi \times 2.6$ MHz, $\Gamma_{\rm m} = 2\pi \times 0.1$ Hz, $g = 2\pi \times 15\sqrt{N}$ Hz, $\Delta = -2\pi \times 1.62$ MHz, and $n_{\rm th} = 4200$, a cooling curve is calculated, clearly showing saturation of the mechanical mode's phonon occupation $\bar{n}$ at the backaction limit $n_{\rm ba} = 0.18$, replicating the theory curve in Fig. 6.7.

noise (RPSN) experiment, where an additional near-resonant beam was used to drive mechanical motion via a fluctuating radiation pressure force [22]. Despite n_{ba} diverging as $\Delta \to 0$, the product $n_{\mathrm{ba}}\Gamma_{\mathrm{opt}}$ does not, leaving this as a useful heuristic to also understand RPSN, at least in the case where there is an additional red-detuned laser to damp and readout the mechanical motion. For technical reasons, this is almost always the case in our experiments, as it provides a constant amount of damping that overcomes any instability that may arise if the near-resonant laser is slightly blue-detuned, and thus anti-damps or amplifies mechanical motion to some degree.

Another notable calculation is the effect of RPSN on the mechanical mode. Increasing the power of a resonant pump will eventually drive the mechanical motion, increasing its apparent temperature. By setting $\Delta = 0$ in the model, we can readily calculate a situation similar to Fig. 6.9, where the mechanical mode temperature is monitored as the resonant pump power is increased until its effect on the resonator is roughly ten times that of the original thermal motion (Fig. 2.4).

In both cases, the mechanical spectrum has been calculated directly. Of course, the only experimentally accessible way to infer knowledge of the mechanical state is to measure an optical output mode. After accounting for realistic conditions such as being coupled to an internal loss in the cavity or a second cavity mirror, the simple expressions for the output spectrum can be readily modified to yield the appropriate result. While interpreting this output spectrum in general requires some form of calibration to infer the mechanical state (our old default approaches are detailed in Ref. [19]), the recent emergence of sideband asymmetry as a measurement technique simplifies the conceptual considerations greatly [52, 53, 54, 55, 56, 3]. In the classical cooling regime, where $\bar{n} > \{1, n_{\mathrm{ba}}\}$, the ratio of red and blue mechanical sidebands, regardless of the attenuation of the output signal, is given simply by the ratio of the cavity susceptibility evaluated at each sideband frequency. While in direct photodetection and homodyne the upper and lower mechanical sidebands are folded together, in heterodyne they are separately visible and their amplitudes can be measured to perform mechanical thermometry. Specifically, one monitors the shift in sideband amplitudes that occurs as the system enters the quantum regime. At this point, the red and blue sidebands,

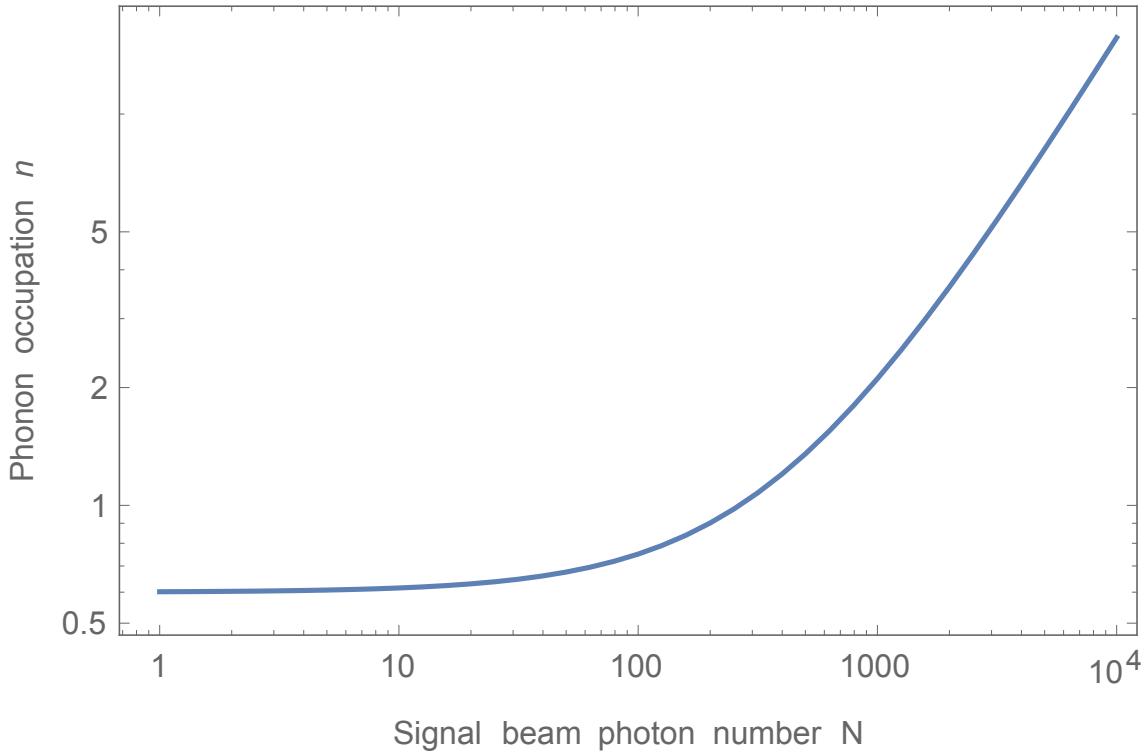

Figure 2.4: Same parameters as in Fig. 2.3, except the pump is now on resonance ($\Delta = 0$) and the mode is precooled to $n_{\rm th} = 0.6$. The correspondence between N and lock power in μW in Fig. 6.9 is not exact, influenced by the uncalibrated detuning, among other factors.

whose scattering rates depend on $\bar{n}+1$ and $\bar{n}$, respectively, will change. For a system with the laser at $\Delta = 0$, the previously equal sidebands will become asymmetric, directly proportional to the ratio $\frac{\bar{n}}{\bar{n}+1}$. For a detuned laser with $\Delta < 0$, the *ratio* of the new asymmetry to the old asymmetry is proportional to $\frac{\bar{n}}{\bar{n}+1}$. Additionally, sideband asymmetry provides information on the quantum efficiency of detection ϵ is available, since the magnitude of the asymmetry induced by the 1 in $\frac{\bar{n}}{\bar{n}+1}$, compared to the amplitude of shot noise in the heterodyne receiver, is a direct measure of what fraction of the intracavity signal was detected. In sum, sideband asymmetry, when available, is a straightforward tool to infer the state of the mechanical mode that is insensitive to loss in the detected signal requires little additional calibration.

2.4 Practical calculations: Microwave-to-optical converter

One of the most technologically relevant applications of optomechanics may be to convert between microwave and optical signals at the quantum level, using the coherent optomechanical dissipation to overwhelm mechanical decoherence that might otherwise spoil fragile quantum information. The mechanisms for this conversion have undergone substantial theoretical study [57, 58, 59, 60, 61, 62, 63, 64, 65, 66], and are related to similar approaches using the electro-optic effect [67, 40, 41]. In order to describe such a converter, we modify the derivations above to a more general case, where the mechanical mode of interest is separately coupled to two electromagnetic resonators. In our case, they will be an optical mode at 1064 nm and a microwave resonant circuit at 7 GHz, but for the purposes of this calculation that distinction is not relevant. We begin by briefly writing a new Hamiltonian, and anticipating how the vectors and matrices describing this system will differ from before. We note that this particular derivation was where the state space model was first of immense benefit to us. This derivation follows one given in the supplementary material to Ref. [42]. The expanded Hamiltonian is given by

$$H = \hbar\omega_{\mathrm{o}} a^\dagger a + \hbar\omega_{\mathrm{e}} b^\dagger b + \hbar\omega_{\mathrm{m}} c^\dagger c + \hbar G_{\mathrm{o}}(a^\dagger a)x + \hbar G_{\mathrm{e}}(b^\dagger b)x \tag{2.21}$$

where we use the reserved letter b to denote the annihilation operator of the microwave cavity. Switching to a more uniform system of labels, the mode frequencies ω_i (and other quantities) are indexed by $i = \{\mathrm{o}, \mathrm{e}, \mathrm{m}\}$ to denote optical, electrical, and mechanical. We also introduce additional ports in the optical and microwave resonators: let the total linewidth of the optical resonator be $\kappa_\mathrm{o} = \kappa_\mathrm{o,L} + \kappa_\mathrm{o,R} + \kappa_\mathrm{o,int}$, comprising the left mirror (the port that is used during measurement of the converter), right mirror, and internal loss. The microwave resonator has two ports with linewidth $\kappa_\mathrm{e} = \kappa_\mathrm{e,R} + \kappa_\mathrm{o,int}$, and the mechanical resonator has a single port with linewidth κ_m (which for symmetry in this context we have used instead of Γ_m).

The (now more numerous) internal modes of the system are described by the vector $\mathbf{a} = (\hat{a}, \hat{b}, \hat{c}, \hat{a}^\dagger, \hat{b}^\dagger, \hat{c}^\dagger)$. The much more numerous input and output modes $\mathbf{a}_\mathrm{in}$ and $\mathbf{a}_\mathrm{out}$, along with the matrices A, B, C, and D are detailed in the last section of this chapter. In this case, using the transfer function formalism will be the focus of this analysis. This formalism reflects our measurement, where we can apply fields (i.e. modify $\mathbf{a}_\mathrm{in}$) and measure fields (i.e. measure components of $\mathbf{a}_\mathrm{out}$). The upconversion transmission coefficient of our converter $t_1(\omega)$ corresponds to the transfer function element $\xi_{a_\mathrm{out,L}, b_\mathrm{in,R}}(\omega) = a_\mathrm{out,L}(\omega)/b_\mathrm{in,R}(\omega)$. In the weak-coupling ($\kappa_\mathrm{e}, \kappa_\mathrm{o} \gg \Gamma_\mathrm{e}, \Gamma_\mathrm{o}$) limit (which our experiment satisfies), it can be simplified to

$$t_1(\omega) = \xi_{a_\mathrm{out,L}, b_\mathrm{in,R}}(\omega) = -\sqrt{\frac{\kappa_\mathrm{e,R}}{\kappa_\mathrm{e}}\frac{\kappa_\mathrm{o,L}}{\kappa_\mathrm{o}}}\epsilon \frac{\sqrt{\Gamma_\mathrm{e}\Gamma_\mathrm{o}}}{-i(\omega - \omega'_\mathrm{m}) + (\Gamma_\mathrm{e} + \Gamma_\mathrm{o} + \kappa_\mathrm{m})/2}\sqrt{\mathcal{A}}\exp(i\phi) \tag{2.22}$$

Here, $\omega'_\mathrm{m} = \omega_\mathrm{m} + \Omega_\mathrm{e} + \Omega_\mathrm{o}$, where Ω_e and Ω_o are the electro- and optomechanical frequency shifts (which we will otherwise omit, writing ω'_m as simply ω_m). Γ_e and Γ_o are the electro- and optomechanical damping rates (see last section). The gain term $\mathcal{A}$ and the associated phase shift ϕ are given by

$$\mathcal{A} = \mathcal{A}_\mathrm{e} \times \mathcal{A}_\mathrm{o} = \left[\frac{(\Delta_\mathrm{e} - \omega'_\mathrm{m})^2 + (\kappa_\mathrm{e}/2)^2}{-4\Delta_\mathrm{e}\omega'_\mathrm{m}}\right] \times \left[\frac{(\Delta_\mathrm{o} - \omega'_\mathrm{m})^2 + (\kappa_\mathrm{o}/2)^2}{-4\Delta_\mathrm{o}\omega'_\mathrm{m}}\right] \tag{2.23}$$

$$\phi = \arctan\left(\frac{\kappa_\mathrm{e}/2}{\Delta_\mathrm{e} + \omega'_\mathrm{m}}\right) + \arctan\left(\frac{\kappa_\mathrm{o}/2}{\Delta_\mathrm{o} + \omega'_\mathrm{m}}\right) \tag{2.24}$$

For $\Delta_\mathrm{e} = \Delta_\mathrm{o} = -\omega'_\mathrm{m}$, $\mathcal{A}$ simplifies to $\left[1 + \left(\frac{\kappa_\mathrm{e}}{4\omega'_\mathrm{m}}\right)^2\right]\left[1 + \left(\frac{\kappa_\mathrm{o}}{4\omega'_\mathrm{m}}\right)^2\right]$, giving it a simple interpretation in terms of the resolved-sideband parameter.

Reflection measurements are described generically by the following transfer function element:

$$\xi_{a_{\mathrm{out,L}},a_{\mathrm{in,L}}}(\omega) = -\left[1 - \frac{\kappa_{\mathrm{o,L}}}{-i(\omega+\Delta_{\mathrm{o}})+\kappa_{\mathrm{o}}/2}\right]\frac{-i(\omega-\omega_{\mathrm{m}}-\Omega_{\mathrm{e}}-\Omega_{\mathrm{o}}\mathcal{B})+(\Gamma_{\mathrm{e}}+\Gamma_{\mathrm{o}}\mathcal{B}+\kappa_{\mathrm{m}})/2}{-i(\omega-\omega_{\mathrm{m}}-\Omega_{\mathrm{e}}-\Omega_{\mathrm{o}})+(\Gamma_{\mathrm{e}}+\Gamma_{\mathrm{o}}+\kappa_{\mathrm{m}})/2} \tag{2.25}$$

where $\mathcal{B} = (1 - \frac{i\kappa_{\mathrm{o,L}}/2}{\Delta_{\mathrm{o}}})/(1 - \frac{\kappa_{\mathrm{o,L}}}{-i(\omega+\Delta_{\mathrm{o}})+\kappa_{\mathrm{o}}/2})$ is a resonant enhancement factor of order unity. Equivalent expressions for other electromagnetic output fields can be obtained via substitution of appropriate parameters. As an aside, this is a case where algebraic simplification of the exact result does not quite give a satisfactory answer—in particular, the factor $\mathcal{B}$ and its associated expression defy useful interpretation.

Another path through the system—used for signal-to-noise measurements—is from the mechanical bath input to an optical output:

$$\xi_{a_{\mathrm{out,L}},c_{\mathrm{in}}}(\omega) = -i\sqrt{\epsilon\frac{\kappa_{\mathrm{o,L}}}{\kappa_{\mathrm{o}}}}\frac{\sqrt{\Gamma_{\mathrm{o}}\kappa_{\mathrm{m}}}}{-i(\omega-\omega'_{\mathrm{m}})+(\Gamma_{\mathrm{e}}+\Gamma_{\mathrm{o}}+\kappa_{\mathrm{m}})/2}\sqrt{\mathcal{A}_o}\exp\left[i\arctan\left(\frac{\kappa_{\mathrm{o}}/2}{\Delta_{\mathrm{o}}+\omega'_{\mathrm{m}}}\right)\right] \tag{2.26}$$

From these, and consideration of how to calculate the operator output spectrum in earlier sections, we can write the signal to noise ratio (SNR) of an upconverted signal:

$$\mathrm{SNR} = S_{\mathrm{in}}(\omega)\left(|\xi_{a_{\mathrm{out,L}},b_{\mathrm{in,R}}}(\omega)|^2\frac{2\pi\delta(\omega-\omega')}{\langle a^\dagger_{\mathrm{out,L}}a_{\mathrm{out,L}}\rangle}\right) \tag{2.27}$$

where S_{in} is the spectral density of the input microwave field and the second term is noise at the output of the converter referred to the input. If we assume all fields in $\mathbf{a}_{\mathrm{in}}$ except $\hat{c}_{\mathrm{in}}$ and $\hat{c}^\dagger_{\mathrm{in}}$ are that of vacuum, and additionally use $\Delta_{\mathrm{e}} = \Delta_{\mathrm{o}} = -\omega'_{\mathrm{m}}$ and $\Gamma_{\mathrm{e}} = \Gamma_{\mathrm{o}}$, the expression for SNR simplifies to:

$$\mathrm{SNR} = \mathcal{A}_e\frac{\kappa_{\mathrm{e,R}}}{\kappa_{\mathrm{e}}}\left[\frac{\kappa_{\mathrm{m}}n_{\mathrm{env}}}{\Gamma_{\mathrm{e}}} + \left(\frac{\kappa_{\mathrm{e}}}{4\omega'_{\mathrm{m}}}\right)^2 + \left(\frac{\kappa_{\mathrm{o}}}{4\omega'_{\mathrm{m}}}\right)^2\right]^{-1} \times S_{\mathrm{in}}(\omega) \tag{2.28}$$

$$= \mathcal{A}_e\eta_{\mathrm{e}}\left[\frac{\kappa_{\mathrm{m}}n_{\mathrm{env}}}{\Gamma_{\mathrm{e}}} + (\mathcal{A}_{\mathrm{e}}-1) + (\mathcal{A}_{\mathrm{o}}-1)\right]^{-1} \times S_{\mathrm{in}}(\omega) \tag{2.29}$$

In this case the added vibrational noise, n_{vib}, is found through $\mathrm{SNR} = S_{\mathrm{in}}/n_{\mathrm{vib}}$.

2.5 Classical laser noise analysis

An important check on the results of any experiment claiming to see quantum correlations and effects in continuous measurement is to assess the potential impact of classical amplitude and phase noise on the measurement. Classical noise on the laser can drive an optomechanical system via radiation pressure as readily as quantum noise, and in many systems can be large enough to swamp any quantum signal. Calculations to capture the effect of classical laser noise are conceptually straightforward: add classically-correlated amplitude and phase noise terms to the description of the incoming pump laser alongside the quantum noise operators. The difficulty lies in the more complicated algebra, and in the end identifying and collecting terms in the calculation which clearly elucidate classical noise's effect on both mechanical motion and the optical measurement of that motion. A history of useful published calculations and discussion of classical noise in our group includes Refs. [19, 22, 68, 54, 3], including supplemental materials. Other especially pertinent sources include Refs. [69, 70, 21, 53]. I apologize for not providing additional technical detail on the effects of classical laser noise, but humbly submit that writing an additional technical document with insidious factor-of-two and transcription errors may be of little benefit to the community.

2.6 List of vectors and matrices

2.6.1 Single-port optomechanical system

$$A = \begin{pmatrix} i\omega_{\mathrm{m}} - \Gamma_{\mathrm{m}}/2 & -ig & 0 & -ig \\ -ig & i\Delta - \kappa/2 & -ig & 0 \\ 0 & ig & -i\omega_{\mathrm{m}} - \Gamma_{\mathrm{m}}/2 & ig \\ ig & 0 & ig & -i\Delta - \kappa/2 \end{pmatrix} \tag{2.30}$$

$$B = \mathrm{Diag}(\sqrt{\Gamma_{\mathrm{m}}}, \sqrt{\kappa}, \sqrt{\Gamma_{\mathrm{m}}}, \sqrt{\kappa}) \tag{2.31}$$

$$C = B \tag{2.32}$$

$$D = -I \tag{2.33}$$

$$\Sigma = \mathrm{Diag}(n_{\mathrm{th}}, 0, n_{\mathrm{th}} + 1, 1) \tag{2.34}$$

2.6.2 Microwave-to-optical converter

In the expressions presented below, $g_{\mathrm{e}} = G_{\mathrm{e}} x_{\mathrm{zp}} \sqrt{n_{\mathrm{e}}}$ and $g_{\mathrm{o}} = G_{\mathrm{o}} x_{\mathrm{zp}} \sqrt{n_{\mathrm{o}}}$ are electro- and optomechanical couplings in Hz. The electrical pump produces a classical intracavity field described by β, where $|\beta| = \sqrt{n_{\mathrm{e}}}$ and $\mathrm{Arg}[\beta] = \theta_{\mathrm{p}}$. Likewise, the optical pump produces a classical intracavity field described by α, where $|\alpha| = \sqrt{n_{\mathrm{o}}}$ and $\mathrm{Arg}[\alpha] = \phi_{\mathrm{p}}$. We also use $n_{\mathrm{th,m}}$ to describe the mechanical bath phonon occupation, and use $n_{\mathrm{th,e}}$ ($n_{\mathrm{th,o}}$) to describe the average photon occupation of the electrical (optical) input fields, which should both be zero at dilution refrigerator temperatures, but are included for completeness and for comparison to previous results at 4 K.

$$\Omega_{\mathrm{e}} = g_{\mathrm{e}}^2 \left[\frac{\Delta_{\mathrm{e}} + \omega_{\mathrm{m}}}{(\Delta_{\mathrm{e}} + \omega_{\mathrm{m}})^2 + (\kappa_{\mathrm{e}}/2)^2} + \frac{\Delta_{\mathrm{e}} - \omega_{\mathrm{m}}}{(\Delta_{\mathrm{e}} - \omega_{\mathrm{m}})^2 + (\kappa_{\mathrm{e}}/2)^2} \right] \tag{2.35}$$

$$\Omega_{\mathrm{o}} = g_{\mathrm{o}}^2 \left[\frac{\Delta_{\mathrm{o}} + \omega_{\mathrm{m}}}{(\Delta_{\mathrm{o}} + \omega_{\mathrm{m}})^2 + (\kappa_{\mathrm{o}}/2)^2} + \frac{\Delta_{\mathrm{o}} - \omega_{\mathrm{m}}}{(\Delta_{\mathrm{o}} - \omega_{\mathrm{m}})^2 + (\kappa_{\mathrm{o}}/2)^2} \right] \tag{2.36}$$

$$\Gamma_{\mathrm{e}} = g_{\mathrm{e}}^2 \left[\frac{\kappa_{\mathrm{e}}}{(\Delta_{\mathrm{e}} + \omega_{\mathrm{m}})^2 + (\kappa_{\mathrm{e}}/2)^2} - \frac{\kappa_{\mathrm{e}}}{(\Delta_{\mathrm{e}} - \omega_{\mathrm{m}})^2 + (\kappa_{\mathrm{e}}/2)^2} \right] \tag{2.37}$$

$$\Gamma_{\mathrm{o}} = g_{\mathrm{o}}^2 \left[\frac{\kappa_{\mathrm{o}}}{(\Delta_{\mathrm{o}} + \omega_{\mathrm{m}})^2 + (\kappa_{\mathrm{o}}/2)^2} - \frac{\kappa_{\mathrm{o}}}{(\Delta_{\mathrm{o}} - \omega_{\mathrm{m}})^2 + (\kappa_{\mathrm{o}}/2)^2} \right] \tag{2.38}$$

$$A = \begin{pmatrix} i\Delta_{\mathrm{o}} - \frac{\kappa_{\mathrm{o}}}{2} & 0 & -ie^{i\phi_{\mathrm{p}}} g_{\mathrm{o}} & 0 & 0 & -ie^{i\phi_{\mathrm{p}}} g_{\mathrm{o}} \\ 0 & i\Delta_{\mathrm{e}} - \frac{\kappa_{\mathrm{e}}}{2} & -ie^{i\theta_{\mathrm{p}}} g_{\mathrm{e}} & 0 & 0 & -ie^{i\theta_{\mathrm{p}}} g_{\mathrm{e}} \\ -ie^{-i\phi_{\mathrm{p}}} g_{\mathrm{o}} & -ie^{-i\theta_{\mathrm{p}}} g_{\mathrm{e}} & -\frac{\kappa_{\mathrm{m}}}{2} - i\omega_{\mathrm{m}} & -ie^{i\phi_{\mathrm{p}}} g_{\mathrm{o}} & -ie^{i\theta_{\mathrm{p}}} g_{\mathrm{e}} & 0 \\ 0 & 0 & ie^{-i\phi_{\mathrm{p}}} g_{\mathrm{o}} & -i\Delta_{\mathrm{o}} - \frac{\kappa_{\mathrm{o}}}{2} & 0 & ie^{-i\phi_{\mathrm{p}}} g_{\mathrm{o}} \\ 0 & 0 & ie^{-i\theta_{\mathrm{p}}} g_{\mathrm{e}} & 0 & -i\Delta_{\mathrm{e}} - \frac{\kappa_{\mathrm{e}}}{2} & ie^{-i\theta_{\mathrm{p}}} g_{\mathrm{e}} \\ ie^{-i\phi_{\mathrm{p}}} g_{\mathrm{o}} & ie^{-i\theta_{\mathrm{p}}} g_{\mathrm{e}} & 0 & ie^{i\phi_{\mathrm{p}}} g_{\mathrm{o}} & ie^{i\theta_{\mathrm{p}}} g_{\mathrm{e}} & i\omega_{\mathrm{m}} - \frac{\kappa_{\mathrm{m}}}{2} \end{pmatrix} \tag{2.39}$$

$$B = \begin{pmatrix} M & 0 \\ 0 & M \end{pmatrix} \tag{2.40}$$

$$M = \begin{pmatrix} \sqrt{\kappa_{\mathrm{o,L}}} & \sqrt{\kappa_{\mathrm{o,R}}} & \sqrt{\kappa_{\mathrm{o,int}}} & 0 & 0 & 0 \\ 0 & 0 & 0 & \sqrt{\kappa_{\mathrm{e,R}}} & \sqrt{\kappa_{\mathrm{e,int}}} & 0 \\ 0 & 0 & 0 & 0 & 0 & \sqrt{\kappa_{\mathrm{m}}} \end{pmatrix} \tag{2.41}$$

$$C = \begin{pmatrix} \sqrt{\kappa_{\mathrm{o,L}}} & 0 & 0 & 0 & 0 & 0 \\ \sqrt{\kappa_{\mathrm{o,R}}} & 0 & 0 & 0 & 0 & 0 \\ 0 & \sqrt{\kappa_{\mathrm{e,R}}} & 0 & 0 & 0 & 0 \\ 0 & 0 & 0 & \sqrt{\kappa_{\mathrm{o,L}}} & 0 & 0 \\ 0 & 0 & 0 & \sqrt{\kappa_{\mathrm{o,R}}} & 0 & 0 \\ 0 & 0 & 0 & 0 & \sqrt{\kappa_{\mathrm{e,R}}} & 0 \end{pmatrix} \tag{2.42}$$

$$D = \begin{pmatrix} -1 & 0 & 0 & 0 & 0 & 0 & 0 & 0 & 0 & 0 & 0 & 0 \\ 0 & -1 & 0 & 0 & 0 & 0 & 0 & 0 & 0 & 0 & 0 & 0 \\ 0 & 0 & 0 & -1 & 0 & 0 & 0 & 0 & 0 & 0 & 0 & 0 \\ 0 & 0 & 0 & 0 & 0 & 0 & -1 & 0 & 0 & 0 & 0 & 0 \\ 0 & 0 & 0 & 0 & 0 & 0 & 0 & -1 & 0 & 0 & 0 & 0 \\ 0 & 0 & 0 & 0 & 0 & 0 & 0 & 0 & 0 & -1 & 0 & 0 \end{pmatrix} \tag{2.43}$$

$$\Sigma = \begin{pmatrix} N & 0 \\ 0 & N+I \end{pmatrix} \tag{2.44}$$

$$N = \begin{pmatrix} n_{\mathrm{th,o}} & 0 & 0 & 0 & 0 & 0 \\ 0 & n_{\mathrm{th,o}} & 0 & 0 & 0 & 0 \\ 0 & 0 & n_{\mathrm{th,o}} & 0 & 0 & 0 \\ 0 & 0 & 0 & n_{\mathrm{th,e}} & 0 & 0 \\ 0 & 0 & 0 & 0 & n_{\mathrm{th,e}} & 0 \\ 0 & 0 & 0 & 0 & 0 & n_{\mathrm{th,m}} \end{pmatrix} \tag{2.45}$$

$$\mathbf{a}_{\mathrm{in}} = \begin{pmatrix} \hat{a}_{\mathrm{in,L}} & \hat{a}_{\mathrm{in,R}} & \hat{a}_{\mathrm{in,int}} & \hat{b}_{\mathrm{in,R}} & \hat{b}_{\mathrm{in,int}} & \hat{c}_{\mathrm{in}} & \hat{a}^{\dagger}_{\mathrm{in,L}} & \hat{a}^{\dagger}_{\mathrm{in,R}} & \hat{a}^{\dagger}_{\mathrm{in,int}} & \hat{b}^{\dagger}_{\mathrm{in,R}} & \hat{b}^{\dagger}_{\mathrm{in,int}} & \hat{c}^{\dagger}_{\mathrm{in}} \end{pmatrix}^{T} \tag{2.46}$$

$$\mathbf{a}_{\mathrm{out}} = \begin{pmatrix} \hat{a}_{\mathrm{out,L}} & \hat{a}_{\mathrm{out,R}} & \hat{b}_{\mathrm{out,R}} & \hat{a}^{\dagger}_{\mathrm{out,L}} & \hat{a}^{\dagger}_{\mathrm{out,R}} & \hat{b}^{\dagger}_{\mathrm{out,R}} \end{pmatrix}^{T} \tag{2.47}$$

Chapter 3

Optomechanical cavities - calculations and characterization

The simplest one-dimensional description of an optical cavity has the end mirrors serve as nodes of the electric field. Since the light inside the cavity is the sum of both left and right-propagating waves, a standing wave is formed whose intensity is periodic every half-wavelength. Thus an optical cavity is "on resonance" if its length ℓ is exactly an integer number of half-wavelengths long. Off resonance, no mode is supported. This suggests two possible ways of making an optical cavity in practice: The first is to adjust the length of the cavity via some feedback mechanism until the cavity is in resonance with a fixed-frequency laser. The second is to tune the frequency of the laser until its wavelength is such that the fixed cavity length is now an integer number of half-wavelengths. This chapter will present the properties of optical cavities and the methods used to characterize them in the lab.

The simple one-dimensional model in the introductory paragraph does not tell us about the transverse profile of the cavity mode. However, coupling light to mechanical motion requires that the transverse mode spot probe specific parts of the moving material. Otherwise, differential mechanical motion in the transverse plane can cancel out the optical signal. Fig. 3.1 shows a schematic view of the transverse mode inside a cavity, as well as a typical optical transverse mode imaged in transmission. To describe this mode, we will consider propagation of light in the paraxial (or small angle of divergence) limit.

The geometry of an optical cavity mode is described by the solution to the paraxial Helmholtz

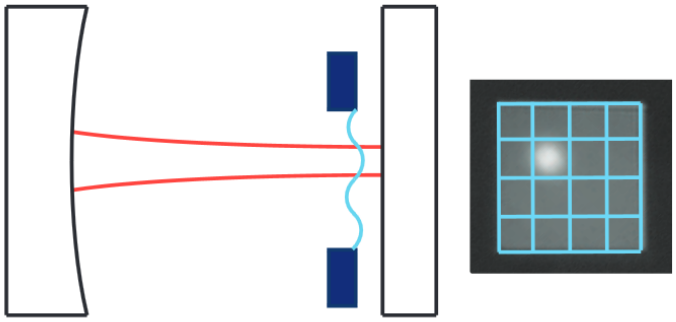

Figure 3.1: Left) Schematic drawing of a membrane-at-the-end cavity, with characteristic width of transverse mode outlined in red. Right) Transverse mode of the optical cavity (white gaussian), with nodal lines of the (4,4) mechanical mode of the membrane overlaid. Optomechanical coupling g is proportional to the overlap integral between the optical transverse modeshape and the mechanical modeshape. The optical mode has a 180 μm $1/e^2$ diameter, and the membrane is 500 μm square. Taken from Fig. 1a in Ref. [19].

equation, propagating in the z direction. Here I take the lowest-order Gaussian transverse profile,

$$\mathbf{E} = E_0 \hat{x} \frac{w_0}{w(z)} \exp\left(\frac{-r}{w(z)^2}\right) \exp\left(-i\left(kz - k\frac{r^2}{w(z)^2}2R(z) - \phi(z)\right)\right) \tag{3.1}$$

where $k = 2\pi/\lambda$ is the wavenumber, $w(z)$ is the $1/e^2$ power radius of the beam, with the waist $w_0 = w(0)$, $R(z)$ the radius of curvature of the wavefronts, and $\phi(z)$ the Gouy phase. An optical cavity can be thought of as the placement of mirrors to act as nodes of the electric field along two phase front surfaces of this mode, in analogy with the simple construction at the start of the chapter. For example, a plano mirror can be placed at $z = 0$, where the phase fronts are planar, and a curved mirror with radius of curvature equal to $R(z)$ can be placed a distance z away. The volume between them is a cavity mode whose intensity profile is proportional to $\mathbf{E}^* \cdot \mathbf{E}$.

Stable optical cavities are described by a set of TEM modes, which describe both the longitudinal and transverse dimensions. For our purposes, it is convenient to describe the transverse modes using Hermite-Gaussian modes u_{mn}, shown in Fig. 3.2. The lowest-order transverse mode is simply the gaussian profile of the TEM00 mode described in Eqn. 3.1. The rectangular symmetry of these modes corresponds to the higher-order modeshapes observed in our cavities due to tilting of the membrane, which breaks cylindrical symmetry. The angular frequencies ω_{qnm} of the cavity mode resonances are given by

$$\omega_{qnm} = \left(q + (n + m + 1)\frac{\arccos \pm\sqrt{g_1 g_2}}{\pi}\right) \times \frac{\pi c}{\ell} \tag{3.2}$$

Here, q denotes the longitudinal mode, which for the lowest-order transverse mode $m = 0$, $n = 0$, is incremented in angular frequency units of $\frac{\pi c}{\ell}$, called the free spectral range (FSR). In non-angular units (as it is unfortunately often quoted), FSR $= \frac{c}{2\ell}$ can be clearly seen to be the inverse of the round-trip time for light to traverse the cavity. The Gouy phase shift means that the higher-order (m, n) transverse modes are in general nondegenerate in frequency. This spacing, in units of $\frac{\arccos \pm\sqrt{g_1 g_2}}{\pi} \times$ FSR, is the transverse mode spacing or TMS. Here, $g_1 = 1 - \frac{\ell}{R_1}$ and $g_2 = 1 - \frac{\ell}{R_2}$ describe the cavity geometry. In the regime discussed in this thesis, cavities are relatively near the planar-planer limit ($R_i \gg \ell$), and one mirror is plano ($R_2 = \infty$, $g_2 = 1$), so transverse modes are always nondegenerate.

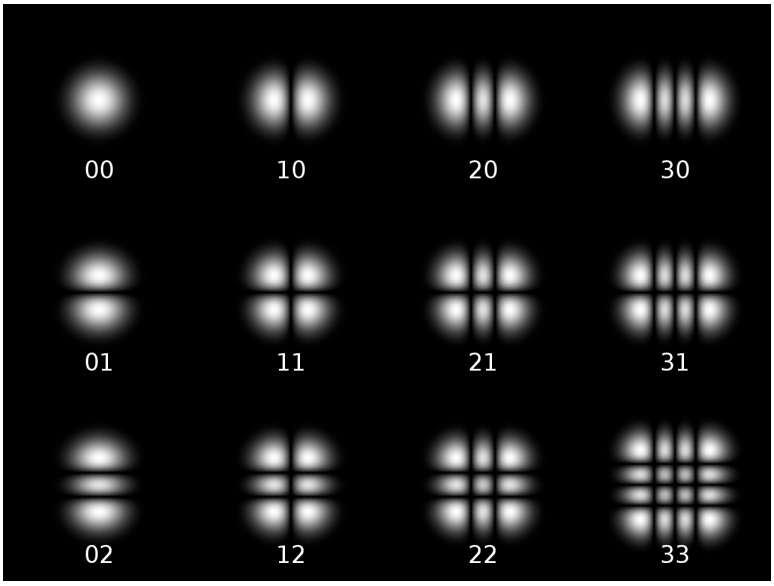

Figure 3.2: Hermite-Gaussian modes u_{mn}, which form an orthogonal basis set for transverse modes in an optical cavity. (Image: DrBob at en.wikipedia)

The specific equations describing a Gaussian beam are useful for routine calculations. The radius of curvature is given by $R(z) = z + z_R^2/z$, where $z_R = \frac{\pi w_0^2}{\lambda}$ is the Rayleigh range. The $1/e^2$ intensity beam radius is $w(z) = w_0\sqrt{1 + (\frac{z}{z_R})^2}$. In practice, a cavity's waist can be calculated by solving for w_0 in the equation $R(\ell) = R_{\text{mirror}}$, since typically the radius of curvature of the curved mirror R_{mirror} is well-known. The cavity length can be measured directly via examining the transverse optical modes of the cavity. With a known radius of curvature mirror, the length can be directly computed from the ratio of TMS to FSR, using Eqn. 3.2.

3.1 Cavity characterization - empty cavity

The most basic property of an optical cavity is its FWHM linewidth κ, the inverse of the cavity decay time τ. Practical measurements of κ involve either slowly scanning across the cavity resonance in frequency to trace out the lineshape, or from a cavity ringdown to observe the exponential decay. The ringdown is the simplest, most direct measurement, because it doesn't require an external frequency reference, being a time-domain measurement. The cavity is probed with light, and then the light is cut off either with a fast switch or by moving the laser frequency off cavity resonance very quickly. Scanning an end-mirror piezo at kilohertz frequencies with sufficient amplitude is typically able to achieve a fast enough velocity to clearly see and fit to the exponential decay of the light in the cavity. In Fig. 3.3, calculations from Oliver Wipfli's Master's thesis (Ref. [71]) show the lineshapes from the two regimes discussed above. For determination of κ in the slow scanning regime, known frequency markers (usually from an electro-optic modulator) must be placed on the light to scale a fit to the lorentzian lineshape. Fully in the ringdown regime, a simple exponential fit will suffice. The use of the fit parameter $\tau = 1/\kappa$ from either method will be discussed in the following paragraph. For data in the intermediate regime of Fig. 3.3, consult Ref. [71] for the derivation of the nonlinear equation of motion and comments on fitting it to experimental data.

The cavity linewidth varies with cavity length, as the round-trip time increases. The cavity

finesse $\mathcal{F}$, proportional to the power build up, is given by

$$\mathcal{F} = \frac{2\pi}{\Sigma L_i} \tag{3.3}$$

where the L_i describe loss channels in the cavity, which includes mirror transmissions as well as any internal loss due to scattering or absorption in the mirrors or objects inside the cavity such as a membrane. The finesse is related to linewidth via the free spectral range (FSR)

$$\mathcal{F} = \frac{FSR}{\kappa} = \frac{\pi c}{\ell}\frac{1}{\kappa} \tag{3.4}$$

where I will now insist that the FSR and κ are given in angular units. For an empty cavity, the total cavity loss is likely to be dominated by the mirror transmissions as long as the mirrors are clean, that is, $\Sigma L_i = T_L + T_R = 2T$, in the case of a symmetric cavity whose left and right mirrors have transmissions $(T_L, T_R = T)$. In our case, $T = 100$ parts per million (ppm) is a typical value, corresponding to $\mathcal{F} = 31,000$. Via repeated measurement of cavity linewidth after successive cleaning procedures (using First Contact from Photonic Cleaning Solutions), the mirror transmission can be inferred with confidence without requiring the more involved measurements described below.

While the total linewidth is straightforward to measure, the determination of the loss rates through individual mirrors and internal loss is more complicated to experimentally investigate. In general, one wishes to know the transmission rates of each mirror, T_L and T_R, and the internal loss L, corresponding to scattering or absorption due to substrate surface roughness or imperfections in the dielectrics of either the mirror coating stacks or (if present) the membrane's dielectric material. A method for determining these quantities for an optical cavity with two identical mirrors using only reflection and transmission measurements is given in Ref. [72]. A rederivation reproduced here from the supplementary material of our work in Ref. [42] describes the additional measurements to be made if the mirrors have unequal transmissions. (Note that even for a symmetric cavity with identical mirrors, the presence of a membrane dispersively shifts the cavity dynamics, which can result in separate effective mirror transmissions for each mirror.) With nonidentical mirrors,

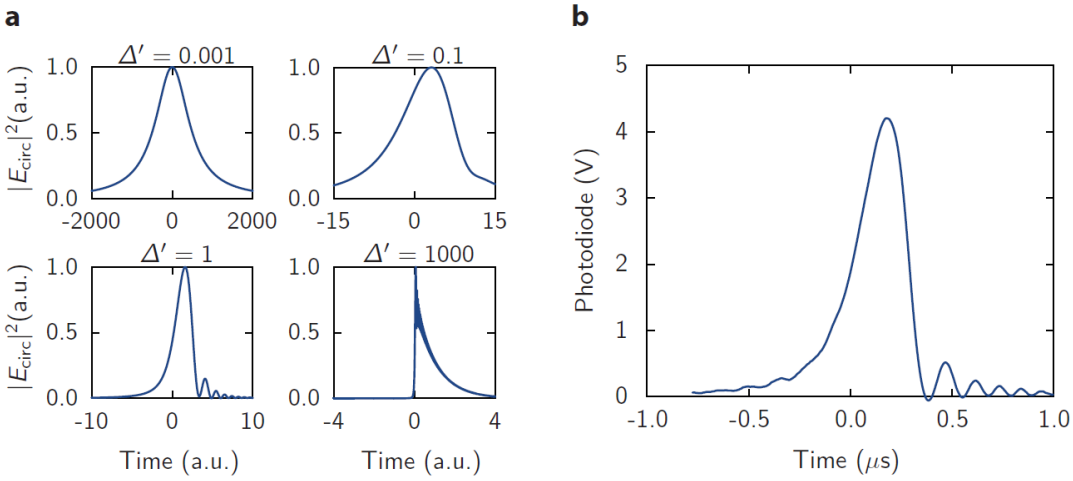

Figure 3.3: Figure taken from Ref. [71]. a) Speed Δ' of the change in cavity length/resonant frequency compared to κ. Note the $\Delta' = 0.001$ regime corresponding to quasistatically tracing the cavity lineshape, the $\Delta' = 1000$ regime corresponding to a cavity ringdown with exponential decay, as well as the intermediate regime. b) Experimental data motivating the investigation of fitting ringdowns in the intermediate regime.

reflection and transmission measurements must be taken from both directions. For each direction that the cavity is probed, there is an additional modematching factor ϵ_L (ϵ_R) describing the overlap of the left (right) input beam with the cavity's TEM00 mode. To solve for all five unknowns, five measurements will be made, namely the cavity finesse, the relative transmission and reflection from probing the left mirror of the cavity, and the relative transmission and reflection from probing the right mirror of the cavity.

The power in transmission probed from the left side, $P_{t,L}$, can be written normalized to the modematched input power $\epsilon_L P_{in,L}$ as

$$\frac{P_{t,L}}{\epsilon_L P_{in,L}} = 4T_L T_R \left(\frac{1}{T_L + T_R + L}\right) \tag{3.5}$$

while the useful power in reflection, which is the reflected power of the input beam $P_{r,L}$ minus the noninteracting unmodematched portion of the input beam $(1 - \epsilon_L)P_{in,L}$, all normalized to modematched input power, can be written

$$\frac{P_{r,L} - (1 - \epsilon_L)P_{in,L}}{\epsilon_L P_{in,L}} = \left(\frac{L + T_R - T_L}{L + T_R + T_L}\right)^2 \tag{3.6}$$

Now, with the trick of dividing Eqn. 3.5 by Eqn. 3.6, we are left with

$$\frac{P_{t,L}}{P_{r,L} - P_{in,L}} = \frac{4T_L T_R}{(L + T_R - T_L)^2 - (L + T_R + T_L)^2} \tag{3.7}$$

which conveniently only has directly measurable optical powers on the left hand side, and the modematching ϵ_L has dropped out. With another equation describing measurements taken probing from the right side (interchange L and R subscripts in Eqn. 3.7), along with a measurement of the cavity finesse $\mathcal{F} = \frac{2\pi}{T_L + T_R + L}$, the system of equations can be solved to yield T_L, T_R, and L. With substitution of those values into Eqn. 3.5, ϵ_L and ϵ_R can be determined as well.

3.2 Cavity characterization - with membrane

A simple but effective model of the membrane-at-the-end cavity that reproduces key optical characterization measurements is a one-dimensional transfer-matrix formalism. In the context of

optomechanical cavities, descriptions of the model are given in graduate student theses (Refs. [73, 71]). The former work describes the details of the model in general, while the latter covers aspects of the calculations used in our group. By modeling the cavity as a stack of dielectric materials in one dimension, the cavity's linewidth κ, as well as the optomechanical coupling G, can be determined. However, some realistic scenarios such as the membrane being tilted with respect to the cavity axis cannot be modeled in this way.

A model of our membrane-at-the-end optomechanical system can be constructed via matrix multiplication of the transfer matrices for mirrors, vacuum, and dielectric plates [73, 72]. Mirrors are represented by

$$M_{\text{mirror}}(n) = \begin{pmatrix} 0 & i/Y_0 n \\ iY_0 n & 0 \end{pmatrix} \tag{3.8}$$

where $Y_0 = \sqrt{\epsilon_0/\mu_0}$ is the vacuum conductance, and $n = \sqrt{\frac{1-r}{1+r}}$ is the effective index of a mirror with amplitude reflectivity $r = \sqrt{1-T}$. This models the mirror as the reflection resulting from the index contrast between vacuum and an unphysically very high index material. Without this simplification, the entire mirror stack would need to be modeled, which is straightforward but not necessary for our purposes in this chapter and often not possible since coating houses may not disclose the stack. Instead, the mirror reflectivity can be obtained via the coating curves or a measurement of κ. Next, vacuum is represented by

$$M_{\text{vacuum}}(L) = \begin{pmatrix} \cos(kL) & i\sin(kL)/Y_0 \\ iY_0 \sin(kL) & \cos(kL) \end{pmatrix} \tag{3.9}$$

where k is the wavevector of the light, and L is the length of the vacuum element. A dielectric plate is represented by

$$M_{\text{dielectric}}(n, L_d) = \begin{pmatrix} \cos(knL_d) & i\sin(knL_d)/nY_0 \\ inY_0 \sin(knL_d) & \cos(knL_d) \end{pmatrix} \tag{3.10}$$

where n is the index of the dielectric, which can model absorption via an imaginary index ($n = n_R - in_I$), and L_d is the thickness of the dielectric. The absorption can also be expressed as a per-pass absorption δ via Beer's law, $\delta = 1 - \exp(-4\pi L_d n_I/\lambda)$. We can now write the characteristic

matrix of our membrane-at-the-end optomechanical cavity, denoting the lengths of the parts of the cavity to the left and right of the membrane as ℓ_1 and ℓ_2:

$$M = M_{\text{mirror}}(n_1)M_{\text{vacuum}}(\ell_1)M_{\text{dielectric}}(n_{\text{Si}_3\text{N}_4}, L_d)M_{\text{vacuum}}(\ell_2)M_{\text{mirror}}(n_2) \tag{3.11}$$

and, from this point, solve the system for the appropriate resonance condition. The resonance condition used in these calculations is that the transmitted phase is an integer multiple of π, or $\Im(M_{11} + M_{12} + M_{21} + M_{22}) = 0$, a condition that can be calculated numerically [73].

The details of how to set up the problem and solve for resonance are very important, especially in our setup. Because we operate with a fixed-frequency laser, the end mirror positions must be adjusted, for example, by changing ℓ_1 to bring the cavity into resonance with the laser. Changing the membrane position is a differential operation that preserves $\ell = \ell_1 + \ell_2$, by increasing ℓ_2 and decreasing ℓ_1 by the same amount δx. For situations such as determining a cavity parameter like κ of G as a function of membrane position, keeping track of what exactly is moving is critical. In fact, depending on which of the model lengths is adjusted, such calculations can give different results.

An example that illustrated this point to us is the measurement of the optomechanical coupling G as a function of membrane position. With $G = \frac{\partial \omega_{\text{cav}}}{\partial x}$, we though that a simple measurement in transmission of the cavity while scanning the end mirror would let us measure a signal proportional to G as a function of membrane position. For a constant scan amplitude on the end mirror piezo, we thought that the shift in time of the cavity modes' resonances would correspond to frequency and thus G via the conversion factor FSR/532 nm. Modeling this situation, however, revealed that we were not measuring G. Instead we were measuring a subtly different but related parameter G_{wrong}. Because G is fundamentally a derivative with respect to frequency, a position scan of the end mirror does not directly probe it. And while a correspondence exists between G and our G_{wrong} via the chain rule, it is instructive to determine how to properly measure G with a fixed-frequency laser. By applying 500 MHz fm sidebands to the laser via an electro-optic modulator, a direct frequency scale can be used for measurement. With a constant-amplitude high-voltage sine wave added to the membrane piezo bias voltage, a constant amount of motion is added to

the membrane. By capturing the jitter of the cavity resonance (by using infinite persistence on an oscilloscope) and comparing it to the frequency markers, a signal proportional to G is obtained. Data for a test cavity illustrating this measurement of G (green, blue) along with finesse (red) are shown in Fig. 3.4. Because of systematic drift in the experiment due to thermal gradients as the lab heats during the day, the data are sequentially shifted. However, since the finesse was measured in between the green and blue traces for G, the horizontal average of the green and blue curves matches the expectation of the model, shown in Fig. 3.5, corresponding to the experimental setup where the mirror nearest the membrane was scanned. An alternative situation modeled in Fig. 3.6 shows the different behavior when the far mirror is scanned. The subtle changes in relative width of the maxima and minima, as well as the phase change of G_{wrong} illustrate the importance of the details of cavity operation, both experimentally and theoretically. For this cavity, the experimental data in Fig 3.4 show a maximum finesse of 30,000, while the model in Fig. 3.5 has a maximum finesse of 41,000. To obtain agreement on this point between the data and the model, introduction of an imaginary index of refraction as described above could be used to model the loss resulting in lower than ideal maximum finesse. Typically, values of $n_I \approx 10^{-5}$ are used to capture per-pass loss of 1-10 ppm in our cavities.

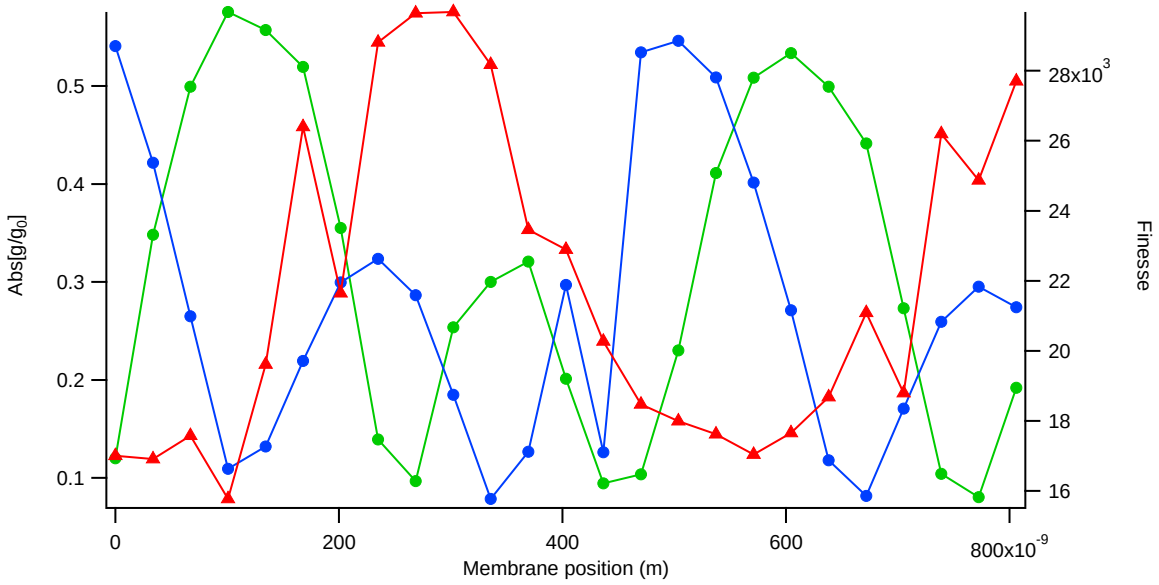

Figure 3.4: Experimental determination of G (arbitrary units) (green, blue circles) and finesse (red triangles) for a $\ell = 6.3$ mm, $\ell_2 = 0.5$ mm optical cavity comprised of two 96 ppm transmission mirrors and a 40 nm thick membrane. Because of systematic drift in the experiment, first G (green), then finesse (red), then G again (blue) was measured. The average of the two G curves' positions corresponds to the expectations of the model.

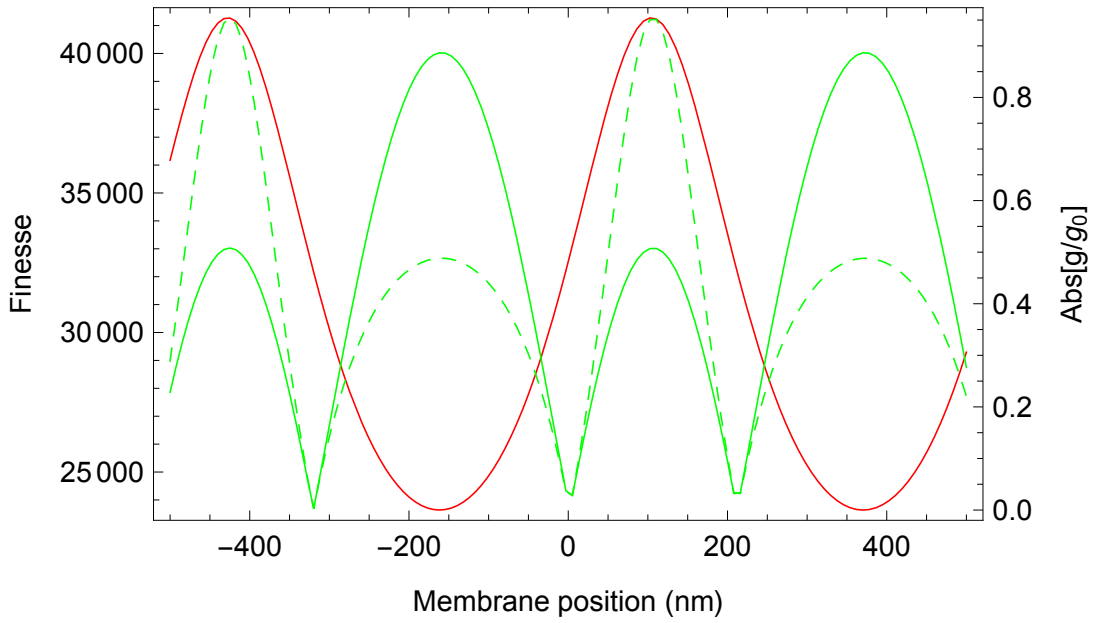

Figure 3.5: Model of the cavity in Fig. 3.4 where the input mirror close to the membrane is adjusted to bring the cavity into resonance. Shown are G (green), G_{wrong} (dashed green), and finesse (red). Note that the high-finesse peak is skinnier than the low-finesse trough. Also note the alternating absolute maxima of G and G_{wrong}.

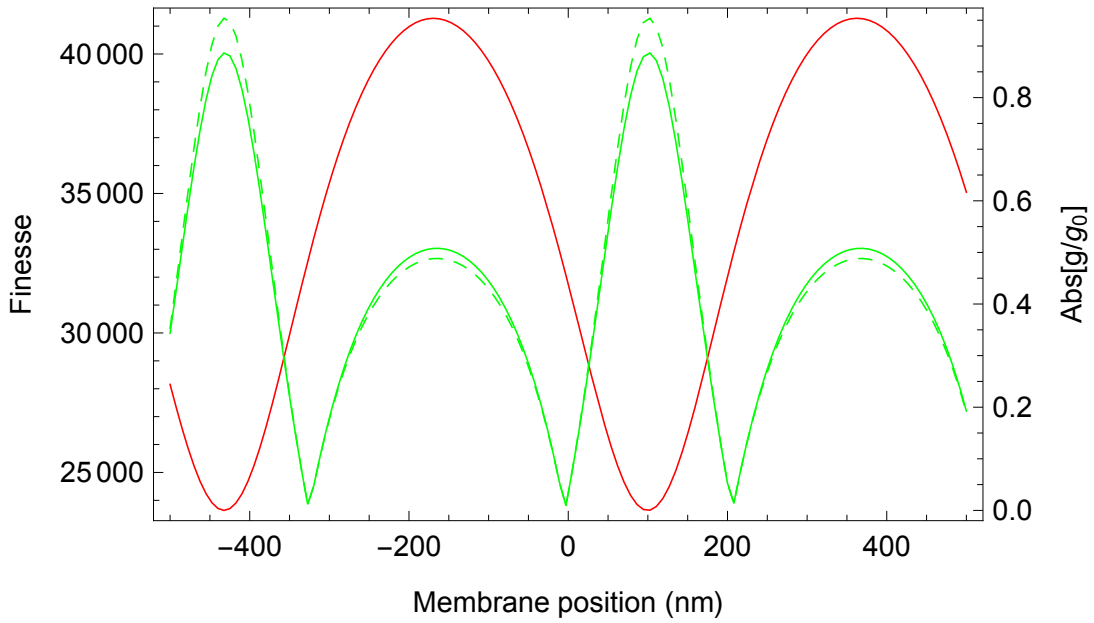

Figure 3.6: Model of the cavity in Fig. 3.4 where the output mirror far from the membrane is adjusted to bring the cavity into resonance. Shown are G (green), G_{wrong} (dashed green), and finesse (red). Note that the high-finesse peak is wider than the low-finesse trough. Also note that the absolute maxima of G and G_{wrong} occur together. Both situations are the opposite of the simulation in Fig. 3.5

Chapter 4

Optomechanical cavities

> How foolish to call them mirrors. They are to mirrors as the enveloping firmament is to a child's balloon. They reflect light indeed; but that, I think, is no part of their true function. They reflect reality, the metaphysical substance that underlies the material world.
>
> *The Book of the New Sun*, Gene Wolfe

Chapters 4 and 5 will discuss the optomechanical cavities designed and used for these experiments. This chapter will be concerned with the pure optomechanical cavities used in experiments since the lab's inception [19, 22, 68, 54, 3, 31]. The cavity designs covered in this chapter are not an exhaustive list of everything ever built, but a history reflecting those cavities used in our lab's publications, with additional designs that shaped our thinking or demonstrated important technological advances. The cavities for the electro-optomechanical experiments, although developed in parallel, will be discussed separately in Chapter 5.

My contributions to optomechanical cavity design started when I joined the lab. The optomechanical cavities discussed here were principally designed by Tom Purdy and subsequently by Nir Kampel, with my advice and assistance, and built in whole or in part by all of us at various times. The optical design of the electro-optomechanical devices in Chapter 5 is the area where I made more central contributions. As the only student who has continuously participated in cavity design and construction from (nearly) the beginning, this thesis is an opportunity to document the history of cavity design in the lab up until the end of 2016.

Our optomechanical cavities consist of a dielectric membrane coupled to the cavity mode

defined by two mirrors, the so-called membrane-at-the-end concept shown in Fig. 4.1. Compared to other optomechanical systems, those using a Fabry-Pérot cavity to confine the light typically exhibit power handling capabilities closer to typical optical cavities, and are often associated with lower-frequency, higher-mass, higher-quality-factor mechanical modes [19]. Many early optomechanical systems were designed with this general approach, with more recent work demonstrating the design we adopted, of two cavity mirrors and a separate mechanically-compliant membrane placed in between [74, 75, 76, 77, 78, 79, 80, 81, 82]. The principal design challenge is to define and maintain interferometric alignment between all three optical elements, despite the thermal contraction of materials as the cavity is cooled to cryogenic temperatures. Additionally, piezoelectric actuation of two optical elements is required to bring the cavity into resonance with a fixed-frequency laser, as well as to position the membrane in the optimal position along the standing wave of optical intensity inside the cavity (Fig. 4.1). While actuation of the mirror and membrane prevent a truly monolithic design, we strive to make the cavity as rigid as possible. In particular, we do not include the ability to adjust other degrees of freedom, such as the transverse position or tip-tilt of optical elements, which we assume will remain aligned as the cavity is cooled.

The constraints of fast iteration on designs early on, as well as the complicated geometries required for aligning and positioning the membrane inside the optical cavity, made us select invar as the cavity spacer material. Invar has the lowest thermal expansion of a metal alloy; its discovery in the early 20th century and subsequent impact on precision measurement merited a Nobel Prize [83]. Selecting the appropriate amorphous or crystalline materials would allow us to match thermal expansion coefficients of the mirror substrates or membrane substrate [84], but machining these materials is beyond the scope of what a researcher in a machine shop can do. Invar is a difficult to machine material, and the intricate geometries we designed are possibly beyond the skill of the less patient graduate student or postdoc, but with sharp tooling, slow cutting speeds, and above all patience, it is possible to machine cavity spacers yourself, as we did for the first several years. With less variability in design, cavities are now made by the professional machinists in the instrument shop, who can achieve tighter tolerances, better parallelism, and can properly anneal the invar

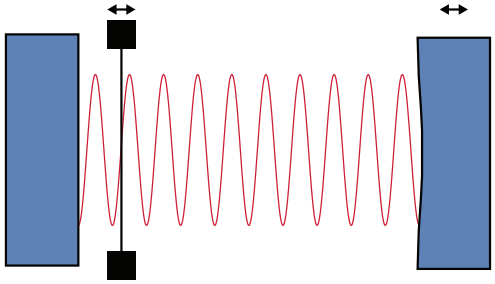

Figure 4.1: Membrane-at-the-end cavity. The membrane is positioned along the desired point of the optical intensity standing wave, and one end mirror's position is adjustable to bring the cavity into resonance with a fixed-frequency laser.

during machining, improving its dimensional stability.

4.1 First cavities

The first cavities in the lab explored a variety of design concepts, first among them how to align the elements and how to make the cavities survive cooling to 5 K without the mirrors or membrane literally falling off. As it turns out, simply adding more epoxy is not the answer, since it strongly clamps the membrane chip, placing a large amount of stress on it which can drastically lower the Q [85, 86].

Fig. 4.2 depicts the design that resulted in our first optomechanics publication. Two devices are pictured, the top is the immediate predecessor to the device used in Ref. [19], while the bottom is the device used in Ref. [19]. They are largely identical, except for the inset curved mirror (bottom right) which reduced the cavity length from 10 mm to 5 mm. From our current design perspective, these cavities reflect the beginnings of several design features that we have used since. Namely, the construction of the spacer out of invar, the geometric clearance to operate in the 1 in diameter bore of the flow cryostat used in early experiments, and the use of piezo actuators on the membrane and one end mirror as the only available degrees of freedom. However, from our current point of view, we can identify several critical features and design choices that are absent

from this design. First among them is accessibility of the membrane. It is often the case that the membrane tilts relative to the cavity mode, gets dirty, or just has a low Q once it's been cooled down, all of which necessitate replacement. In these early designs, everything must be discarded and built anew, since the membrane is glued in place and then entombed by the 1/2 in diameter flat mirror (Fig. 4.2 top and bottom, right side). All subsequent designs allow for nondestructive removal and reinsertion of a new membrane, in some form consistent with other evolving design constraints. There is also a trend towards shorter cavity lengths, starting from this "baseline" of 5 mm, which leads to designs with smaller diameter mirror substrates, and more concentrically-inlaid structures to allow the membrane to sit on a stack of spacers and a piezo whose height is greater than the cavity length. The shift towards smaller mirror radii of curvature to reduce the optical cavity waist also has influenced cavity design, since radii less than 5 mm are not compatible with standard superpolished fused silica substrates, which further complicates the design.

4.2 Our canonical optomechanical cavity design: the RPSN cavity

The next prominent cavity design was first used in Refs [22], shown in Fig. 4.3. It continued to be used through Refs. [68, 54], though in honor of the first result it produced, I will refer to it as the "RPSN cavity." As a single design used in several experiments, it is in many ways the canonical reference that solidified our design concept, and was the point of departure for the electro-optomechanical devices in Chapter 5. The open structure allows for nondestructive replacement of the membrane, which is placed on a multilayer "membrane stack." The membrane stack operationally allows for interferometric alignment and epoxying of the membrane into place, while it can be removed by unscrewing the plate it's epoxied to, as depicted in Fig. 4.7. This allows removal of the membrane and epoxy without dust generation inside the cavity.

4.3 Later designs

A longstanding challenge in cavity design has been the relatively large size of the mirror substrates. The standard size of 7.75 mm is too wide to make the increasingly short cavities we

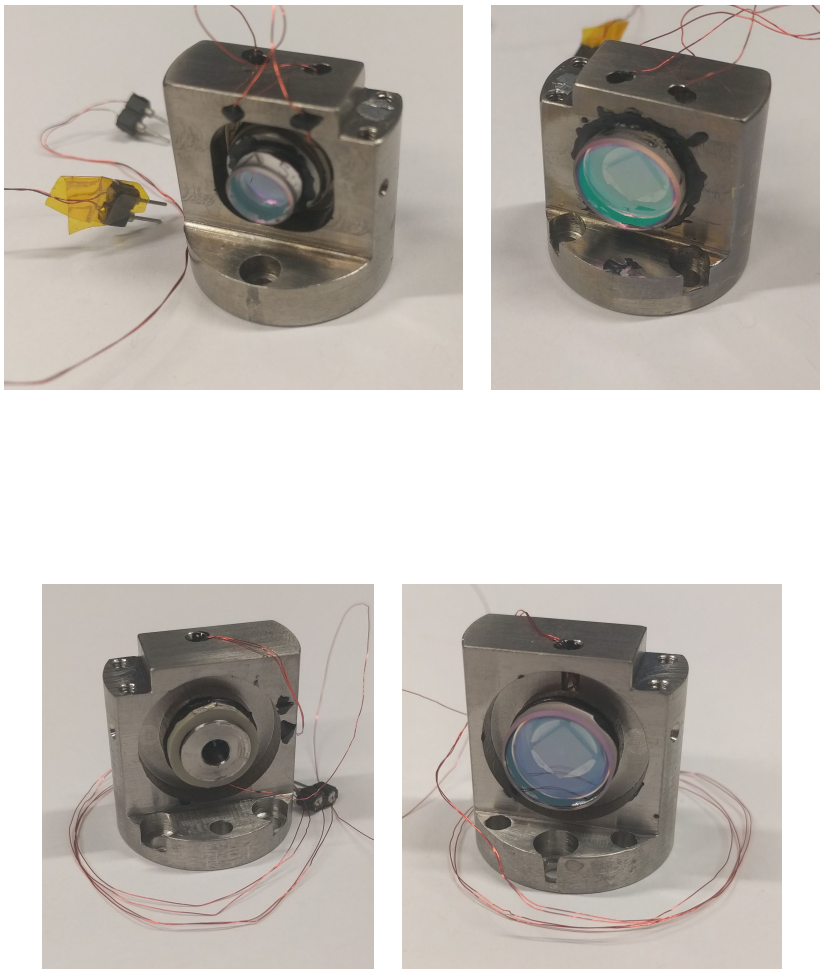

Figure 4.2: Early cavity designs. (top) Immediate predecessor to the device used in Ref. [19]. Cavity length $\ell = 10$ mm, mirror radii of curvature $R = 5$ cm and plano. (bottom) Device used in Ref. [19]. Note the inset curved mirror relative to (top) left, which reduced the cavity length to $\ell = 5$ mm. Mirror radii of curvature $R = 5$ cm and plano.

were planning ($\ell \approx 2$ mm) while still providing comfortable access to insert a membrane in between the mirrors. Tom Purdy explored machining these mirror substrates to both a smaller diameter and shorter thickness, while protecting the already-coated supermirror coating. The mini-mirror cavity in Fig. 4.4 demonstrated an optical cavity using these mirrors, without an increase in cavity linewidth due to surface damage of the dielectric coating. This technique is now used routinely for the devices in Chapter 5, where integration of microwave-frequency electromagnetic modes places even more stringent constraints on the geometry of the cavity mirror substrates.

The final design to be discussed in this chapter is the device used in Refs. [3, 31], the "backaction limit" cavity, shown in Fig. 4.5. The largest change is that the two halves of the cavity—each holding one of the cavity mirrors—separate from each other. This is since the shorter cavity length ($\ell \approx 2$ mm) cannot accommodate the membrane stack concept in Fig. 4.7. In particular, the removal of the membrane is no longer possible, since the thickness of the membrane, the membrane holder, and the top invar plate is greater than the cavity length. While the same membrane stack is used in the backaction limit cavity, the membrane can only be removed after unscrewing the top invar plate if the cavity spacer itself is first unscrewed and separated. We found good repeatability for reassembling the empty optical cavity. In fact, the repeatability of cavity separation and rejoining was good enough to maintain membrane alignment if one was epoxied to the membrane stack. This modularity was a very important test, since these techniques are critical to the latest electro-optomechanical cavity design in Chapter 5.

4.4 Cavity components

Before describing the assembly procedure, I will provide an inventory of components, and an outline their importance in our devices.

The most important aspect of any optical cavity is the mirror. We use superpolished dielectric supermirrors on a fused silica substrate, which are available commercially from local vendors. Cavity mirrors are characterized by their transmission and scattering/absorption, typically in parts-per-million or ppm. The RPSN cavity uses one planar and one 5 cm radius of curvature (ROC)

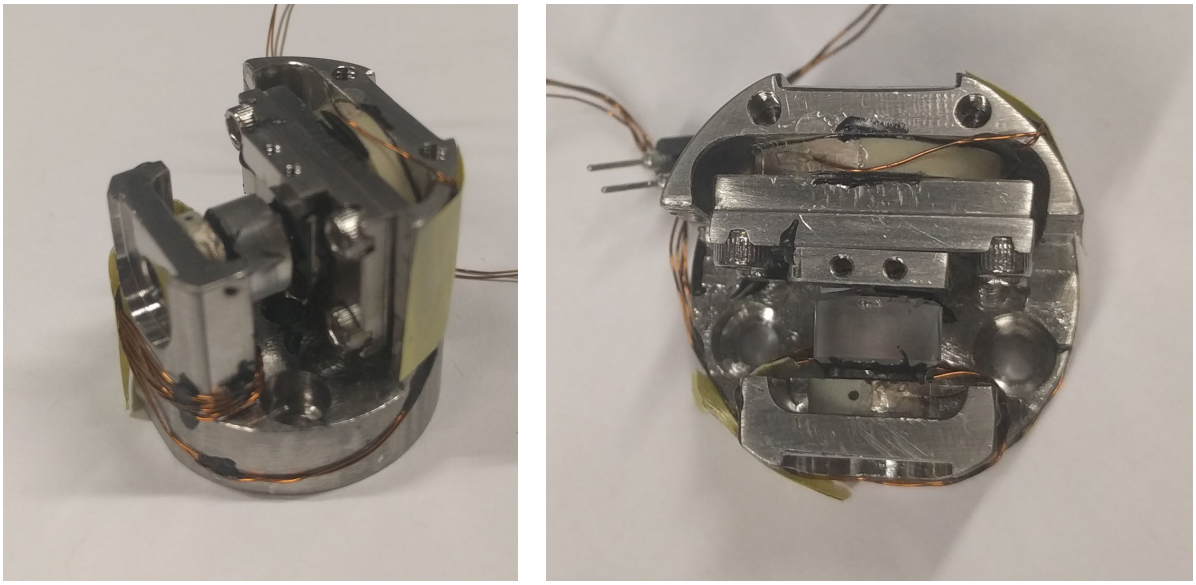

Figure 4.3: RPSN cavity. The principal design change since Fig. 4.2 is the open interior of the cavity, allowing for nondestructive replacement of the membrane inside the cavity. Cavity length $\ell = 5$ mm, mirror radii of curvature $R = 5$ cm and plano.

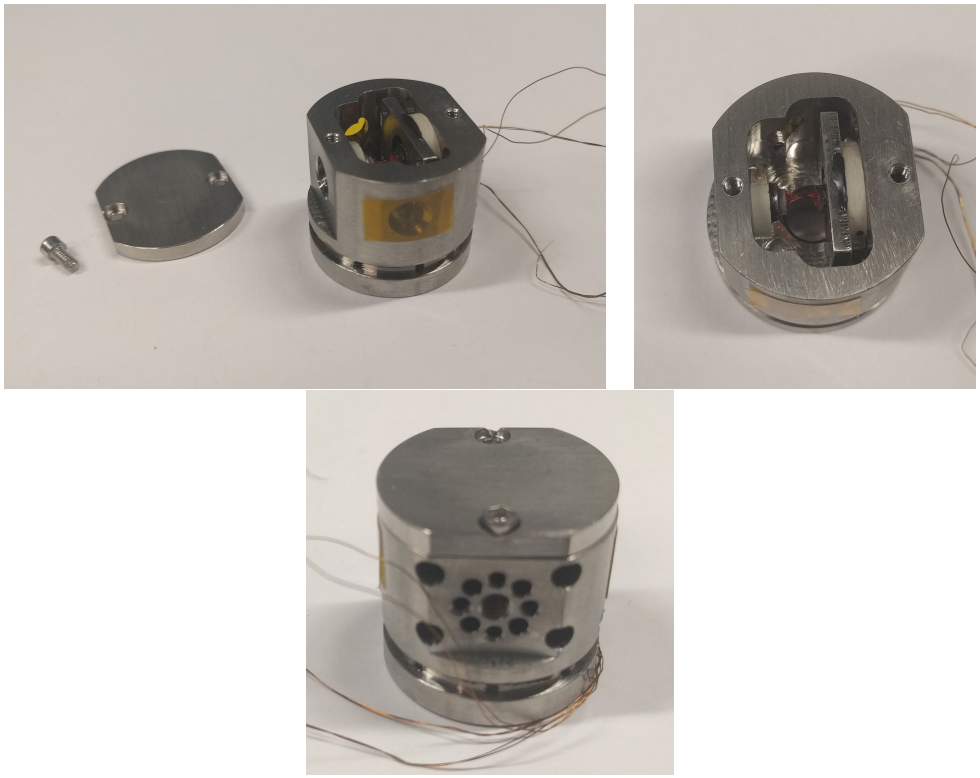

Figure 4.4: Mini-mirror cavity. A realization of a cavity made from few-mm diameter mirrors machined down from the 7.75 mm diameter substrates we bought commercially.

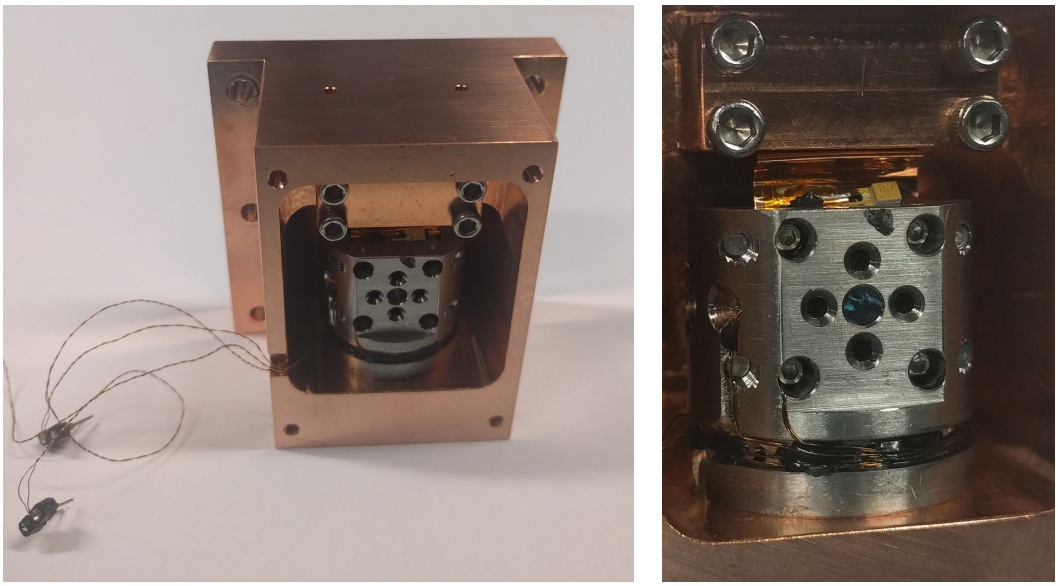

Figure 4.5: Backaction limit cavity, shown in copper enclosure used in dilution refrigerator. Both views show an end mirror epoxied using the back glue joint (four radial holes around optical axis), as well as a copper foil providing a thermal connection between the membrane stack and the copper enclosure, which thermally shorts the bulk of the cavity spacer. Cavity length $\ell = 1.65$ mm, mirror radii of curvature $R = 2.5$ cm and plano.

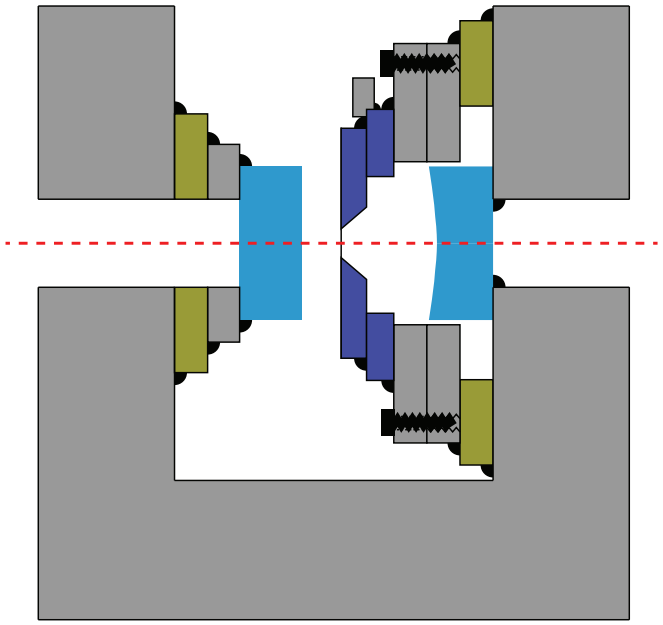

Figure 4.6: Cavity schematic (not to scale). Representative of the RPSN cavity, but some glue joints have been schematically simplified. Optical axis is indicated by dashed red line. The invar cavity spacer (gray), along with the thicknesses of the mirrors and mirror stack components, defines the cavity length. The flat mirror stack (left) consists of a piezo (beige), an invar ring (gray), and the flat mirror (light blue). The stack is assembled separately and centered to the hole in the cavity spacer with an alignment jig (not shown). The membrane stack is as depicted in Fig. 4.7. The curved mirror (light blue) is glued directly to the right side of the cavity spacer, using a glue joint that shares characteristics of the edge glue and the back glue joints in Fig. 4.8.

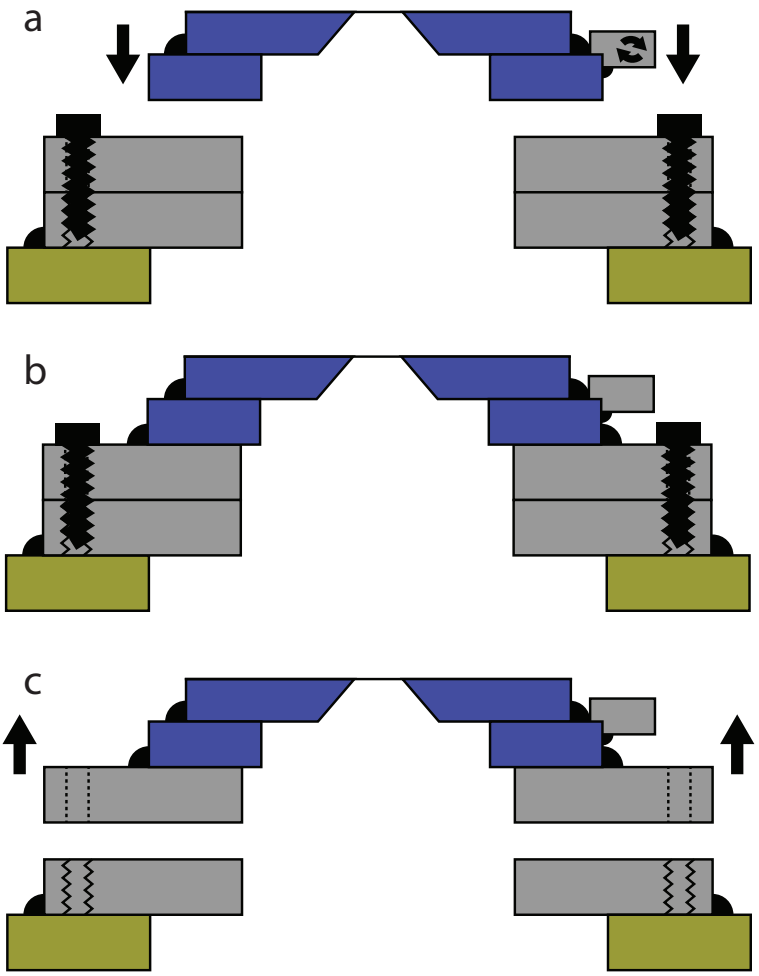

Figure 4.7: Membrane stack. (a) The membrane (blue, top) is epoxied to a machined silicon holder (blue, bottom), which is manipulated by a tapped invar holder (gray, rotation symbol) attached to a five-axis stage. It is interferometrically aligned to the cavity mode before being epoxied to the rest of the membrane stack. The bottom of the stack consists of the piezo (beige), as well as two invar plates (gray) that are attached with screws. (b) Complete membrane stack after membrane alignment and epoxying. The five-axis stage is unscrewed from the invar holder and backed off, leaving a complete optomechanical cavity. (c) When removal of the membrane is desired, the screws connecting the two invar plates are removed, and the assembly from the top invar plate up (including the membrane) is removed by hand.

Figure 4.8: A generic taxonomy of the glue joints used to epoxy cavity components together. (a) The edge glue joint is the most robust, and allows for the two surfaces to be in planar contact. (b) The face glue joint is often used where radial clearance for an edge glue is not possible or ideal. It is more susceptible to delamination due to thermal cycling or applied mechanical stress, and the layer of glue between the surfaces can be uneven. (c) The back glue joint is an alternative to the face glue joint that allows for planar contact between the two surfaces. It is also susceptible to delamination, and care must be taken to ensure the channels are filled with epoxy to make full contact with the second surface. Moving the gluing surface to the backside of one of the components can simplify assembly and reduce the complexity of the cavity interior geometry.

mirror, both with 96 ppm transmission and approximately 1 ppm scattering/absorption, which are representative values for the rest of our devices as well. It is apparent in many other sections of this thesis that having different mirror transmissions can be useful in an optical cavity. The principal constraint is that it's a significant monetary investment to have a coating run done by a vendor, so we initially had only one batch of mirrors with the same mirror transmission value. Another constraint is that the cavity geometry, set by the cavity length and mirror ROC, defines a cavity waist, whose size is ideally matched to the mechanical wavelength of the membrane resonator (Chapter 3). The practical limitation here is the commercial availability of small ROC mirror substrates. Local vendors have supplied us with substrates down to 2.5 cm (Advanced Thin Films) and 1.0 cm, and potentially 5 mm (Perkins Precision Developments). Mirror substrate ROC less than 5 mm are still of interest to us, but they are technologies being developed by researchers [87, 88, 89]. As a general statement, our experiments have been enabled by the high quality of commercially available supermirrors, but desired improvements in substrate geometry have forced us to consider different approaches.

Mirror cleaning is also an important aside. The optical losses of these mirrors are low enough that using lens paper or a solvent wash are inappropriate. We use a drying polymer solution such as First Contact (Photonic Cleaning Solutions) to clean the mirrors, as well as to protect them during handling and storage. We define mirrors to be dirty using the most sensitive metric: When the linewidth of a cavity formed by these mirrors is appreciably higher than what the cavity length and mirror coating curves imply it should be. For us this can be a change in linewidth under 100 kHz, for linewidths typically of order 1 MHz. Aside from the manual technique to apply and remove the polymer solution, consideration should be given to the problem of dust accumulation after removal. The polymer peel-off can leave the surface charged, possibly attracting particles in the air unless precautions are taken [90]. Ion-generating guns using mechanical compression of a piezo are relatively inexpensive and a reasonable way to neutralize surface charge, if that is a concern.

The membrane resonator is the second key component. Many of our experiments have been

performed using commercially available Si_3N_4 membranes (Norcada). A typical chip has a 50 nm thick film suspended over a 0.5 mm x 0.5 mm square hole in a Si frame. They exhibit remarkable mechanical properties, with $Q > 10^6$ at 4 K, and fundamental frequencies $\omega_m \approx 2\pi \times 1$ MHz due to the very high stress of the Si_3N_4 film [78, 86]. A key aspect of cavity design is the reproducibility of the membrane Q due to stress on the chip from mounting [85]. Our approach in most designs is to place the membrane chip on a thermally matched Si holder, machined to support three corners of the membrane, and attached with three very small dabs of epoxy on those corners. Subsequent designs have accommodated more sophisticated membranes, shielded from the substrate by a phononic band gap structure [91]. These were fabricated by collaborators, and eventually ordered as a custom membrane run from the same vendor.

Because we use a fixed-frequency laser, it is necessary to scan the cavity length to bring it into resonance with the laser. It is also necessary to position the membrane along the linear portion of the cavity standing wave, where linear optomechanical coupling is maximized. For this purpose, two piezo actuators are used. We use multilayer ring piezos from Noliac, which are able to scan across multiple half wavelengths at room temperature, and about one half wavelength at cryogenic temperatures. They are also notable for surviving thermal cycling as well as many other components. At cryogenic temperatures, piezos can be operated harmlessly with reverse polarity, giving extra range.

4.5 Cavity construction

For the sake of clarity, discussion of the construction and assembly procedures for our cavities will be condensed to focus on the RPSN cavity. The more complicated procedures in Chapter 5 will again follow this generic prescription, as do later optomechanical cavity designs derived from the RPSN cavity. A schematic depiction of the cavity in Fig. 4.3 is shown in Fig. 4.6, highlighting the components and epoxy joints necessary to construct it. Before discussing the assembly procedure for the RPSN cavity, an aside on how to build an "empty" cavity will serve to illustrate how adding the third optical element complicates the process.

A optical cavity is formed whenever two mirrors are oriented towards each other in a geometry that satisfies a stability condition

$$0 \leq \left(1 - \frac{\ell}{R_1}\right)\left(1 - \frac{\ell}{R_2}\right) \leq 1 \tag{4.1}$$

where R_1 and R_2 are the two radii of curvature. In practice, we take $R_1 = R$ and $R_2 = \infty$ for a single curved mirror and a plano mirror, with $\ell \ll R$, near the plane-parallel cavity limit. More details of cavity stability and mode structure are given in Chapter 3. An interesting practical result arises: The two mirrors do not need to be pointed exactly at each other, that is, the flat backside surfaces of the substrate need not be parallel to each other. As long as the angle is small enough that any part of the curved mirror's surface is locally parallel to the flat mirror's surface, a cavity mode is formed. This effectively means that an optical cavity doesn't need to be aligned to be built. What I will call the "bulk geometry" of the cavity spacer is enough to define a cavity mode. Machining tolerance and mirror placement still need to be good enough to ensure that the cavity mode forms roughly in the right spot, but there is no interferometric constraint. Essentially, two mirrors can be positioned just according to bulk geometry "for free," while any additional optical elements in the cavity mode must be interferometrically aligned. In practice, we epoxy together mirror stacks first, consisting of a piezo for mirror positioning, an invar ring, and finally the mirror on top. The invar ring serves to absorb the stress due to thermal mismatch of the piezo, which shrinks much more than invar and fused silica. The mirror stack, along with a bare mirror, are epoxied to a cavity spacer as schematically shown in Fig. 4.6. This defines a cavity mode, which we actively probe during the rest of the assembly by scanning the mirror piezo and measuring in transmission, both on a photodetector and on a camera. The camera allows for coupling into the TEM00 mode of the cavity, while minimizing coupling to higher-order modes. At this point, the membrane can be aligned and epoxied. It is held to a 5-axis stage providing XYZ positioning and tip-tilt angle orientation. It is placed vertically above the position in the cavity where it is to be epoxied. The cavity, whose post on the optical table is located by a post position retainer, is temporarily removed while the membrane is moved down to the optical axis. The membrane is

aligned via the tip-tilt stages to make it retroreflect the incident laser. It is then raised, and the cavity is returned and realigned by twisting the post in the position retainer until the transmission is maximized. This step coarsely aligns the membrane to the cavity mode, since in the next step, the membrane is inserted into the cavity a small distance from the membrane stack. Until it is aligned, no light will be transmitted through the cavity. This coarse alignment makes it much easier to find the correct alignment by fine-tuning. Exactly aligning the membrane to the cavity mode is done via monitoring the image of the membrane and the optical spot in transmission. If the membrane is tilted, the TEM modes hybridize to form eigenmodes with higher-order TEM components in the direction of the tilt. By ensuring that the membrane can be scanned along the cavity length (using an additional piezo actuator on the XYZ stage) without periodically hybridizing beyond the TEM00 mode, alignment is achieved. Finally, the membrane must be brought into contact with the membrane stack for epoxying. It is here that the concepts of bulk geometry and micro geometry diverge. The membrane cannot be simply pushed into planar alignment with the top of the membrane stack, since this is not interferometrically aligned to the optical mode. The most that can be done is for a corner or an edge of the membrane to come to the threshold of contact with the membrane stack. This is done by scanning the membrane stack piezo. If the membrane is not in contact with the membrane stack, there is no effect to scanning this piezo. If the membrane has made contact, the piezo will begin to push it during the fraction of its sweep in which the membrane stack is in contact with the membrane. Once found, the membrane should be backed off until it's just beyond contact. At this point, small dabs of epoxy can be used to attach the membrane (really, the silicon holder beneath it, shown in Fig. 4.6).

4.6 Epoxy

Gluing together the components of the cavity requires both suitable epoxy and suitable technique. Our epoxy of choice is Stycast 2850 FT, as it is cryogenically compatible, somewhat thermally conductive, and not too dissimilar in thermal expansion to materials we use to crack due to stress. While it is nominally designed to be thermally matched to aluminum (set by the filler

material), it has reliably connected fused silica to invar, and piezos to invar in our applications. It is a two-part epoxy consisting of a resin and a hardener catalyst. The resin compound (properly, the Stycast 2850 FT itself) consists of a chemical resin as well as a filler material, in this case fine aluminum oxide fibers. We typically use catalyst 9 to prepare the epoxy, as its higher viscosity than catalyst 23LV makes it more workable to "paint on" a fillet of glue around edges, as shown in Fig. 4.8. For back glue joints with narrow aspect-ratio access holes or face joints, catalyst 23LV may be more appropriate, as the thinner epoxy can work into small spaces and be spread uniformly over a surface more easily.

Preparing components for epoxying involves proper surface treatment and cleaning. Cavity mirrors can only be cleaned with a polymer solution such as First Contact, and membrane chips typically should not be cleaned so much as replaced if they become dirty. In these cases, it is best to never get them dirty in the first place. For metal components, we typically sand the surfaces with 600 grit sandpaper and then clean them according to a standard protocol: manual cleaning with Simple Green and white (nonabrasive) Scotch Brite, ultrasonic cleaning in a detergent solution, deionized water rinse, and a solvent rinse with acetone, isopropanol, and methanol. Other materials like piezos can be swabbed or rinsed with isopropanol to clean the surfaces prior to gluing.

For epoxy preparation, it is vital to use the recommended vacuum deairing to remove air incorporated during mixing. For application, I recommend using lengths of small-diameter spring steel held freehand, or music wire held in a pin vise. For the smallest of glue joints, aluminum wire from a wirebonder can be used as the applicator, since the stereoscope and the geared-down motion of the needle makes application of tiny amounts of epoxy easier. We do not cure at an elevated temperature out of a concern that it could be harmful to the cavity mirrors, although curing in an oven or a hot plate is common for many cryogenic applications of Stycast 2850. Without elevated temperatures, curing takes approximately 24 hours.

Replacement of the membrane in a membrane stack assembly such as in Fig. 4.7 requires removal of cured epoxy from a reusable invar plate, as do other "undo" operations when a component has failed. I typically use a single-sided razor blade as a chisel; with a light tap the epoxy can be

delaminated from the metal surface. Any remainder is easily removed with a fresh xacto knife or a dental scaler. Light sanding with 600 grit sandpaper removes any residual epoxy or metal flash from the removal process. After cleaning, the part is ready for reuse.

4.7 Lab environment

Cavity construction is best carried out in a clean environment. The current solution is to enclose the cavity construction optical setup and place a HEPA filter above it. The JILA-standard canopies above the optical table readily serve this purpose, since one of the standard 2' x 4' melamine panels can be removed and a HEPA filter put in its place. The canopy framing can support either flexible antistatic vinyl sheeting or a track made from T-slotted framing (80/20 Inc.) with sliding plexiglass panels. A quieter fan makes it psychologically easier to keep the filter for the clean area on continuously, which is the best option. Note that later designs, such as the mini-mirror cavity and the backaction limit cavity (Figs. 4.4, 4.5) have covers to enclose the cavity volume, preventing dust from entering the cavity after assembly and damaging its optical or mechanical properties.

Chapter 5

Electro-optomechanical cavities

The development of electro-optomechanical cavities began in parallel with the developments of Chapter 4, with the original optical design principally inspired by the RPSN cavity. The cavities incorporate both an optical cavity and a microwave-frequency LC circuit, each coupled to the same mechanical resonator. Our success in developing this platform was due to the collaborative effort in its design and fabrication. Design and fabrication of the LC circuit, which is on the same substrate as the membrane, was the result of the work of several collaborators. In this thesis, I will only give a brief outline of the microwave design. References are available which explore this topic in more detail [42, 92, 93]. In particular, Reed Andrews's thesis (Ref. [92]) contains the parallel set of content describing the design and integration of the device from the microwave perspective.

Because the experiments performed with these electro-optomechanical cavities are focused on the application of quantum state conversion between microwave and optical frequencies, the cavities in this chapter will be referred to as converters, emphasizing the two vastly different frequencies of the electromagnetic modes that they bridge.

5.1 Microwave circuits and the flip-chip electromechanical device

While a complete understanding of the converter design requires equal discussion of the optical, mechanical, and microwave components, my principal contribution was in the optical design. In this section, I will provide an overview of the electrical and mechanical design of the converters. For more details, I refer to our collaboration's publications focusing on the mechanical and electrical

design [42, 92, 93].

The basic design principal for the electromechanical portion of the design is the flip-chip. This structure is a stack, formed by a bottom chip and a top chip. The bottom chip contains an inductive loop and capacitor pads formed by deposition of superconducting Nb next to a hole in the chip that allows an optical beam to pass through. These form part of the LC circuit that is electromechanically coupled to motion of the membrane. In the first converter, it also contains a microwave transmission line inductively coupled to the partial LC circuit that allows for an electrical connection to excite and readout the circuit. The top chip contains the membrane; its principal difference from the commercially available Si_3N_4 chips used in some of the designs in Chapter 4 is that part of the membrane surface is metallized with Nb. The top and bottom chips are aligned and placed one on top of the other, and epoxied in place. The separation of the capacitive pads on each chip, which forms a parallel plate capacitor, is defined by pillars on the bottom chip to be a few hundreds of nanometers.

The complete electromechanical flip-chip is almost entirely self-contained, and most importantly can be manipulated, aligned, and epoxied into place in an almost identical manner to the membrane chips used in Chapter 4 for the optomechanical cavities. This conformance to established optical assembly procedures and expertise allowed for fast progress in developing the first converter concept. The one aspect that distinguishes the flip chip is the necessity to couple microwave signals to the LC circuit. Our two approaches to this problem define the different design approaches of our two converters. The first converter uses a wired microwave connection, while the second uses wireless coupling to the LC chip.

5.2 First converter

The first converter design was our initial attempt at combining existing electromechanical and optomechanical technologies developed at JILA. Instead of suspended aluminum membranes like those used in preceding electromechanics experiments [94, 95, 15], colleagues developed the flip-chip electromechanical resonator. Its Nb (instead of Al) circuit superconducts at 4 K, allowing operation

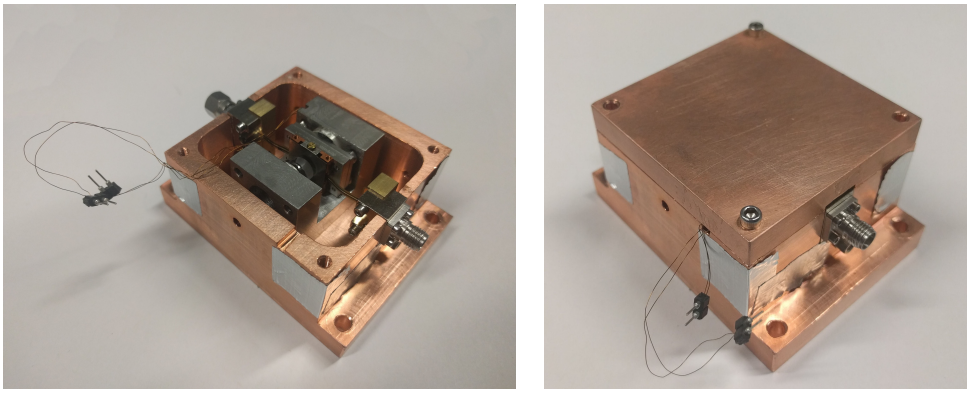

Figure 5.1: Photograph of the first converter, depicting the optical cavity enclosed in an open copper box (left), and with the lid closed (right). A hole in the left side of the box allows transmission of the free-space optical light, while the SMA connector on the right side of the box couples microwave signals to the flip chip via a flexible transmission line. The membrane stack is covered by the Nb shield.

of the device in simpler and more accessible LHe cryostats as opposed to a dilution refrigerator. As discussed in the previous section, the flip chip is also compatible with existing membrane-at-the-end optomechanical designs and assembly procedures in our lab. For more details on its design and construction, refer to Reed's thesis, Ref. [92].

The primary visual difference between the first converter and its predecessor optical designs is that it was not designed to fit in a small flow cryostat, leaving the design free to use simple rectilinear symmetry rather than the upright cylinder shape of all previous designs. A rendering of the converter design is shown in Fig. 5.2, illustrating the rectilinear symmetry and open design. The flexible microwave transmission line that connects the flip chip to the microwave coax wiring in the cryostat requires room for access, so the cavity spacer has a more pronounced U shape, whereas the predecessor optical designs kept circumferential support to add rigidity to the spacer.

A schematic cross-section of the design is shown in Fig. 5.4, which clearly depicts the design heritage from the RPSN cavity in Fig. 4.6. The concept of operationally isolating the electromechanical circuit in the membrane package allowed for immediate integration into existing optical design concepts, which accelerated initial progress on the converter project. The necessarily more-complicated membrane stack is depicted schematically in Fig. 5.5, while a detail exploded view

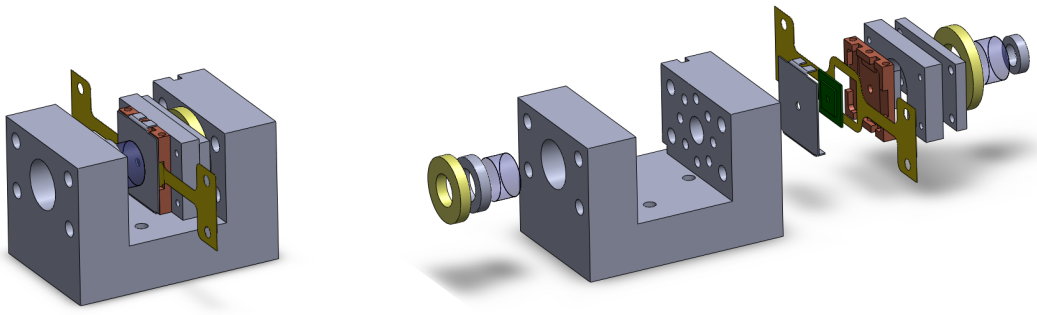

Figure 5.2: Rendering of the design of the first converter, depicting the assembled converter (left) and an exploded view (right) of its components. Parts/materials depicted: invar (gray), piezo (yellow), mirror (translucent), Cu-coated invar (copper), flexible transmission line (beige), flip chip (green), Nb shield (gray).

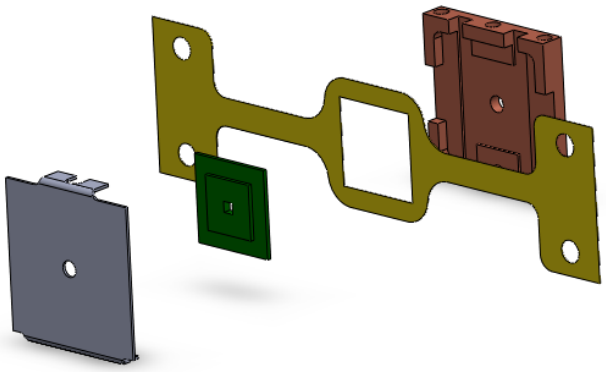

Figure 5.3: Detail of the first converter membrane stack (omits piezo and affixed invar plates). The Cu-coated invar mount (right) locates the flexible microwave transmission line (beige) and the flip-chip (green) for wirebonding necessary to complete the microwave circuit. The Nb shield (gray) is registered to the invar mount to align its aperture to the optical axis position. While the aperture is depicted as a circle in this rendering, by using wire electrical discharge machining techniques, more complex shapes can be cut to precisely conform to the optical clear aperture through the membrane, limiting scattering outside this surface.

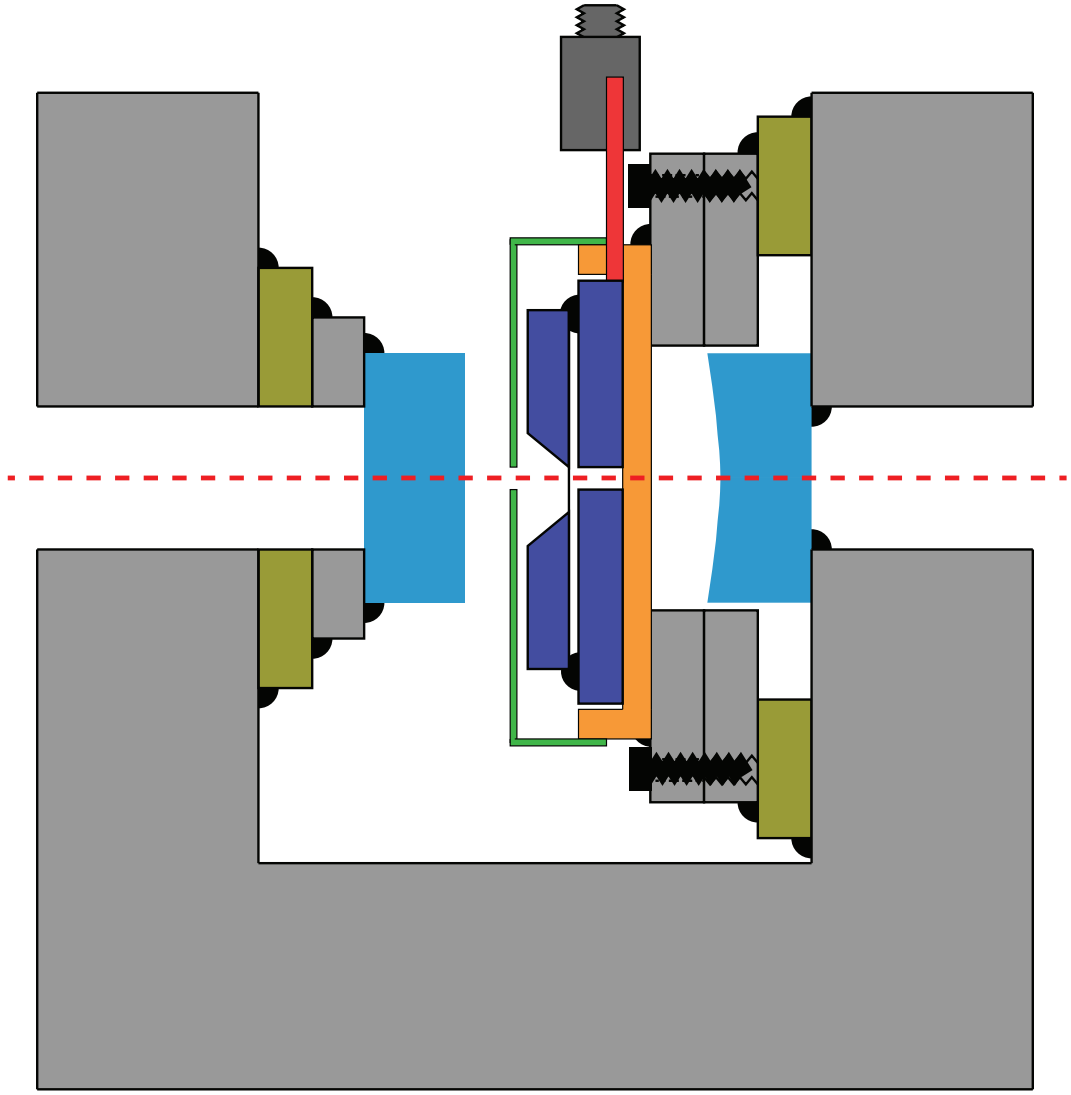

Figure 5.4: First converter schematic. (Not to scale.) The design of the first converter was adapted from the design of the RPSN cavity in Chapter 4. The flat mirror stack (left) consists of a piezo (beige), invar spacer (gray), and the flat mirror (light blue), while the curved mirror is epoxied directly to the cavity spacer (gray). The membrane stack is similar to the RPSN cavity in that the piezo (beige) supports two invar plates (gray) which allow nondestructive removal of the membrane, here a flip-chip electromechanical resonator. The complete membrane package is detailed in Fig. 5.5.

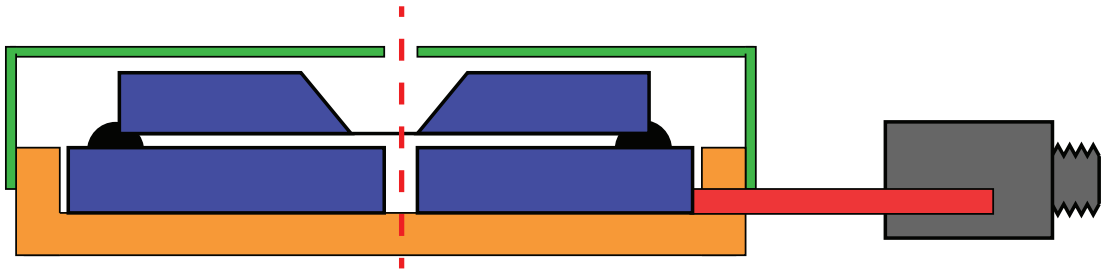

Figure 5.5: Detailed schematic of the membrane stack for the first converter. Optic axis is indicated by dashed red line. The base is a copper-coated invar plate (orange) with raised features to precisely position the flexible microwave transmission line (red) and the flip-chip (blue). The transmission line ends in a SMA connector (dark gray). The flip-chip is covered by a Nb shield (light green) that blocks scattered light from hitting the section of the membrane coated with capacitive Nb pads (left).

render in Fig. 5.3 depicts the portion of the membrane package that is aligned and epoxied into the optical cavity as a unit. The package is manipulated by a five-axis stage via the two 0-80 tapped holes on each side of the invar mount's top. While the flexible microwave transmission line presents an awkward geometry, the heavy SMA connectorization does not need to be connected until after assembly.

Concern that stray light from the optical cavity could hit the superconducting circuit and degrade its performance led us to design a Nb cover to be placed over the flip-chip. Since the flip-chip is precisely located by the final Cu-coated invar plate to align it with the flexible transmission line, the cover can be attached to the invar plate while still covering the exposed LC circuit to the $< 50\mu$m tolerance to prevent obscuring the optical access.

5.2.1 Design and control loop resonances

The active stabilization required to operate our optomechanical cavities, while not unusual for optical cavities, is complicated by the difficulties of cryogenic operation. The quality factor of material resonances can increase, both in the cavity spacer itself, as well as the entire cryostat system. While each cavity design (and indeed, each cryostat) requires tweaking of the feedback loop for stability, this particular design iteration provides an instructive illustration of some of the

problems encountered in cavity operation, as well as one strategy to overcome them.

The first hybrid device was operated in a 4 K bath cryostat (HDL-12, by IRLabs, Inc.). The cavity is mounted on a cold plate attached to the LHe stage, which is shrouded by a LN2 stage, all of which is suspended from the top of the cylindrical cryostat. The largest initial challenge to optical operation of the converter was the inability to lock the cavity using our Pound-Drever-Hall setup. A 2.7 kHz resonance in the feedback loop was the primary cause. Practically speaking, the addition of an elliptic filter designed to notch out the feedback loop's response at this frequency solved the problem (Fig. 5.8). In general, one might expect that active feedback could also help reduce oscillation at this frequency. However, this depends on having sufficient phase and amplitude response at a given frequency servo out an unwanted resonance. Without those conditions being met, simply attenuating the servo response at the problem frequency can prevent the feedback circuit from doing more harm than good. The design of these rf filters have inspired other applications, such as filtering noise at the mechanical frequency on rf carrier tones (Fig. 5.9).

In the subsequent cooldown (where the data in Ref. [42] were taken), we observed similar oscillation at 2.5 kHz. In an attempt to learn more about the problem, network analysis was performed on both the cavity mirror piezo and the membrane piezo. The electronic excitation from the network analyzer is added to the lockbox output to the cavity piezo, and to the bias line to the membrane piezo. In each case, 780 nm laser light is used to read out its effect on the cavity. At this wavelength, the cavity mirrors form only a low-finesse cavity, eliminating any optomechanical effects. The transfer functions of the two piezo stacks are shown in Figs. 5.6, 5.7. They show many similar resonances, though they are all shifted slightly in frequency from their "partner" in the opposite figure. In particular, the 2.480 kHz peak in Fig. 5.6 seems to correspond to the oscillation seen trying to lock the cavity. The piezos themselves all are specified to have a fundamental resonance above approximately 500 kHz (Noliac, Inc.), so even loaded by the mirror or membrane stacks, they are not themselves suspect. A simple argument suggests an explanation: the speed of sound c in metals is typically of order 5000 m/s. The wavelength of a corresponding 2.5 kHz vibrational mode is 2 m. With the cryostat for this experiment standing 1 m tall, one might

suspect that a resonance of the entire cryostat could be responsible. Given the small mechanical connections between temperature stages designed to minimize thermal contact, this argument seems plausible.

5.3 Wireless converter

The second design for our microwave to optical converter set out to solve some of the problems encountered with the first. Namely, coupling to the LC circuit using a flexible transmission line can induce lateral forces on the membrane stack, potentially contributing to interferometric misalignment of the membrane during cryogenic operation. The main design change was to enclose the flip chip in a microwave 3D cavity to enable wireless inductive coupling. A rendering of the design is shown in Fig. 5.10. The design and details of the wireless coupling are described in Ref. [93], whereas this section will focus on the changes in optical design and construction.

The microwave package, previously consisting of the flip chip, its invar mount, and accessories, now properly consists of the flip chip and the enclosing microwave cavity. The microwave 3d cavity is formed by two top and two bottom pieces which fit together. The tops, together called the "hat", can be separately selected and attached to each other to adjust the resonant frequency of the 3d cavity to properly correspond to the resonant frequency of individual flip chips. The microwave cavity bottoms change the optical alignment procedure in that they must be sequentially assembled during membrane alignment. However, the previous cavity and membrane assembly procedure can be largely reproduced. The empty optical cavity is a two-piece spacer similar in concept to the backaction cavity design in Chapter 4, but geometrically enlarged to contain the microwave 3D cavity. Additionally, both mirrors are on longer, thinner stacks to achieve a cavity length $\ell \approx 2$ mm. The ends of the stacks penetrate the microwave 3d cavity through apertures whose diameter is small enough to be a waveguides below cutoff for the microwave fields. Because of this, they are made of microwave-compatible materials only (in particular not invar). In this design, just the mirror substrates and fused silica spacers, along with epoxy, penetrate the microwave cavity. With the empty cavity assembled, the microwave cavity cannot be installed. By inserting the half of

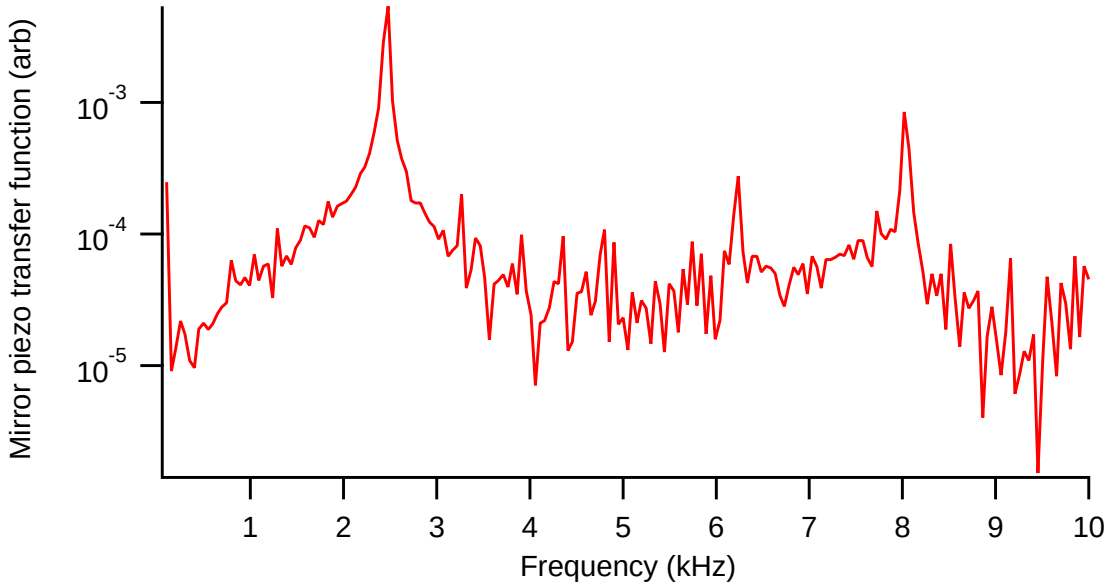

Figure 5.6: Transfer function of the cavity mirror assembly. Excitation is added to lockbox output and amplified before piezoelectrically exciting the cavity end mirror stack (while cavity is locked). Excitation is read out optically via a 780 nm beam (where the cavity has a very small finesse).

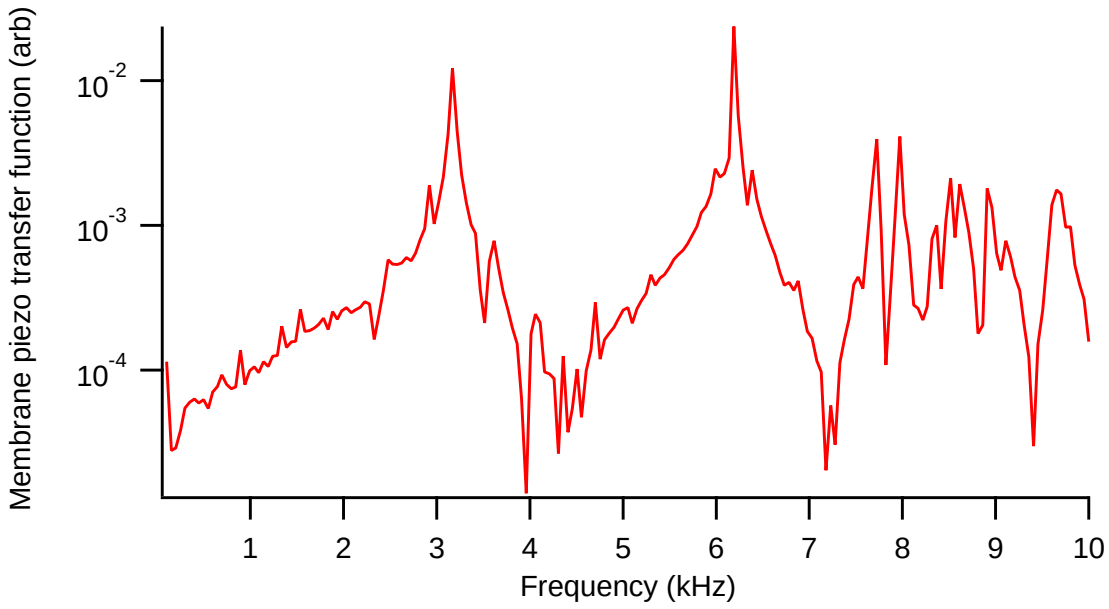

Figure 5.7: Transfer function of the membrane assembly. Excitation is added to the bias voltage for the membrane piezo and piezoelectrically excites the membrane stack. Excitation is read out optically via a 780 nm beam (where the cavity has a very small finesse).

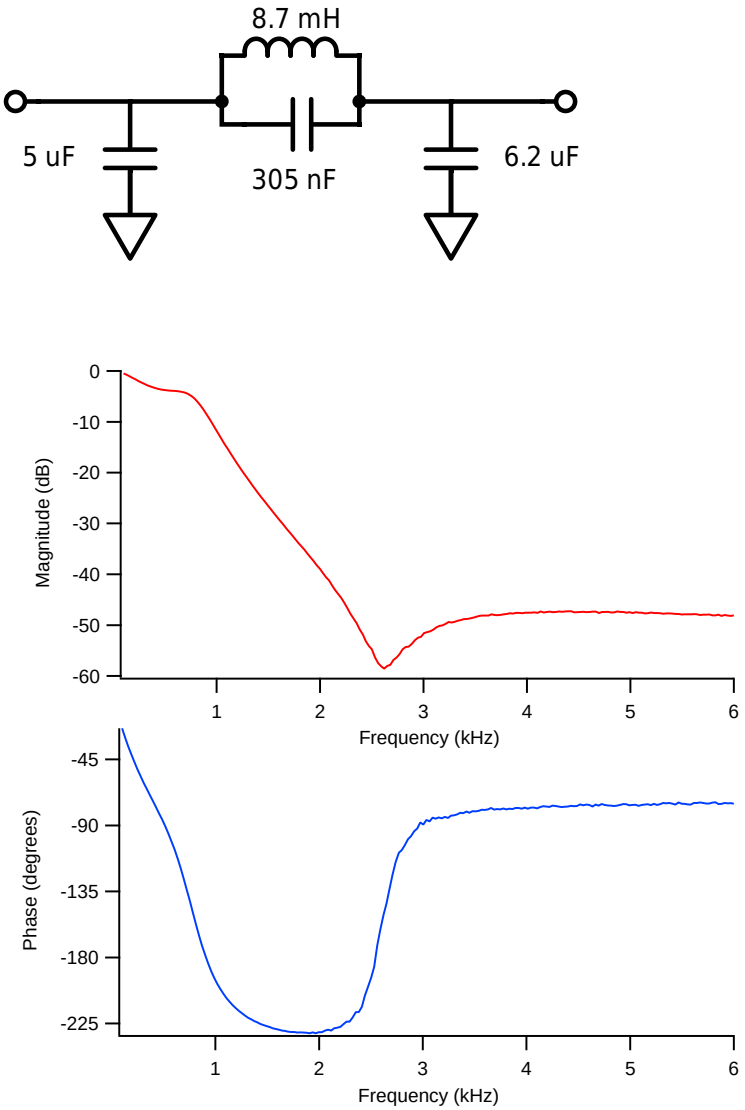

Figure 5.8: Design (top) and measured transfer function (bottom) of the elliptic filter tuned to notch out a specific frequency in the stopband. The design spec is for 2.7 kHz as shown, but typically a tunable capacitor in the LC is used to exactly match the desired frequency. Filter designed in AADE Filter Design program (Neil Heckt).

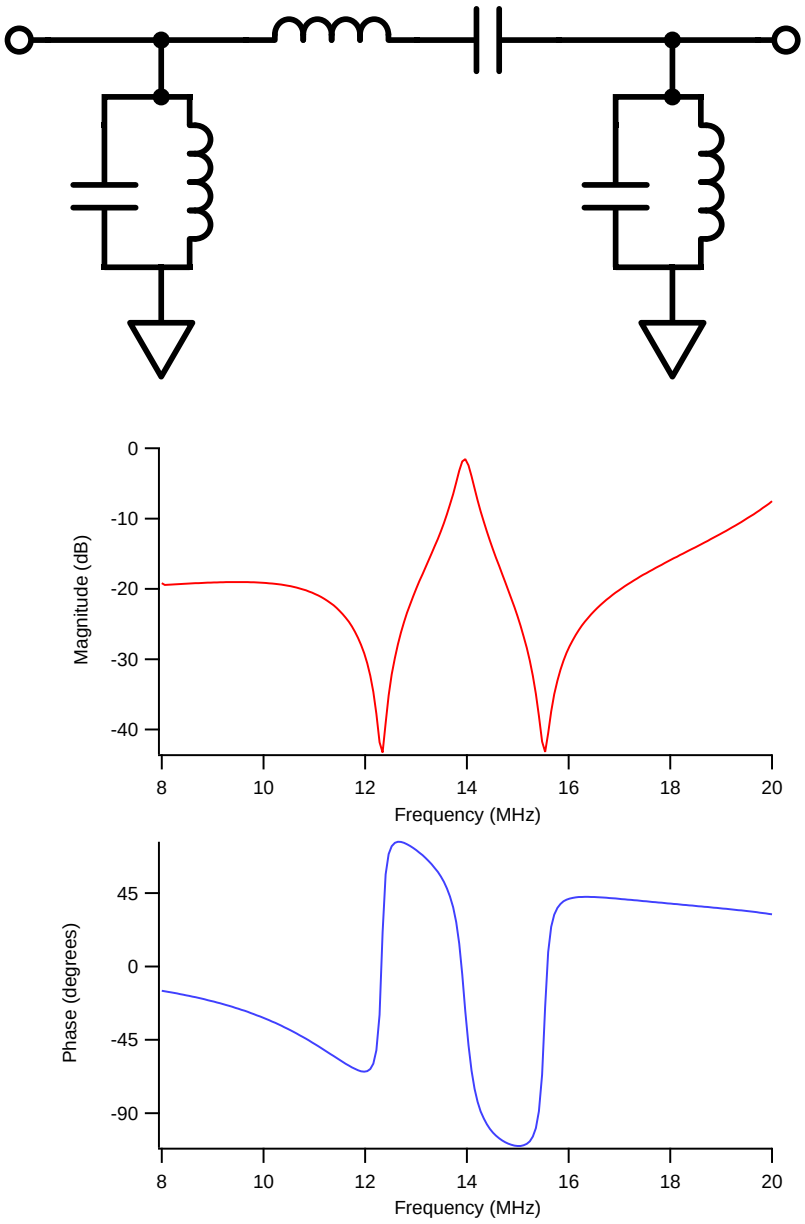

Figure 5.9: Design concept (top) and measured transfer function (bottom) of a bandpass/notch filter design using resonant LC shunts to filter noise at $\pm\omega_{\mathrm{m}}$ from rf carrier signals. Used in Fig. 6.3.

the microwave cavity bottom to which the flip chip is epoxied, and then replacing the removable (curved) mirror, the configuration is analogous to previous membrane alignment and epoxying procedures (Fig. 5.11). Because the flip chip is directly epoxied without additional spacers, the bottom chip is directly grasped and manipulated with a pair of tweezers mounted to a five-axis stage. After alignment and epoxying of the flip chip, the curved mirror must be temporarily removed while the second half of the microwave bottom is attached (Fig. 5.12). Replacement of the curved mirror allows a small amount of freedom to reposition the cavity's transverse mode location, making the remove/replace procedure more resilient and also allowing for small corrections due to imperfect positioning of the membrane chip during its original installation. In summary, the principal change in this design from an optical point of view is that the optical cavity must be disassembled and reassembled before operation, and the membrane (here a flip-chip electromechanical resonator) is mounted directly on the cavity spacer.

The completed wireless converter is shown on the assembly table in Fig. 5.13. Portions of the converter that define the microwave 3d cavity are Au-coated to increase conductivity, though the entire assembly is made of invar. Torquing the screws holding the microwave bottoms or hat produces only a small visible shift of the optical alignment (in particular its transverse position), but can be countered by evenly and lightly tightening the screws for each subassembly. This degree of freedom was not previously available; future work could quantify how useful tightening screws post-epoxying could be for adjusting optical alignment. The wireless converter installed in the base of our optical-access dilution refrigerator is shown in Fig. 5.14.

Familiarity with disassembling cavities before use suggests additional possibilities for cavity design, in particular the partial disassembly of the microwave cavity bottom to insert a thin cover to shield the part of the LC circuit exposed to stray optical light. Due to the different assembly concept, the previous Nb shield concept does not transfer neatly. Instead, a spare bottom chip with a machined hole for optical access (whose profile is the exact shape we want to use to block scattered light) can be used.

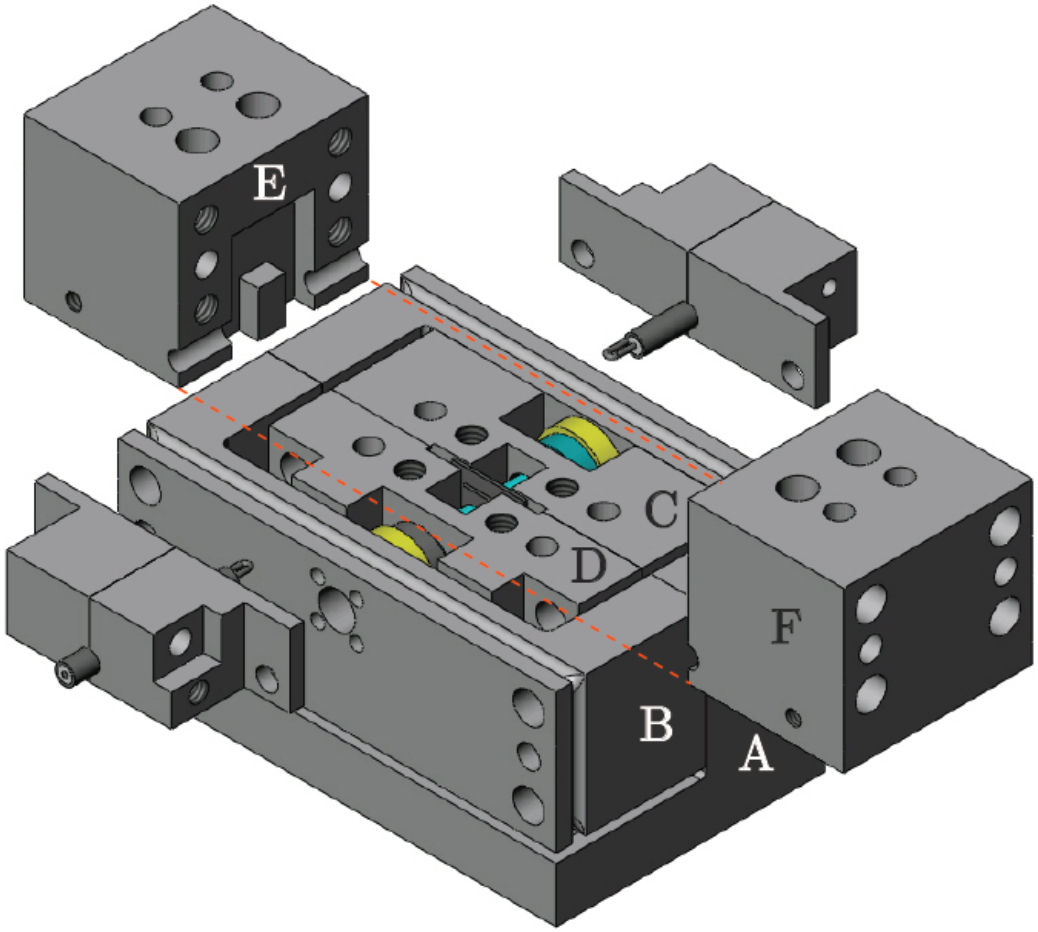

Figure 5.10: Rendering of the wireless converter design. Parts A and B form the optical cavity, and correspond to the flat and curved mirrors, respectively. The membrane is glued directly to C, the second half of the bottom of the microwave 3d cavity is formed by D, and the parts E and F (together the "hat") completely define the microwave 3d cavity. The remaining parts affix coaxial lines terminated in loops that couple inductively to the field inside the 3d cavity. The design name comes from these coaxial lines being wirelessly coupled to the LC circuit. Rendering from Ref. [93].

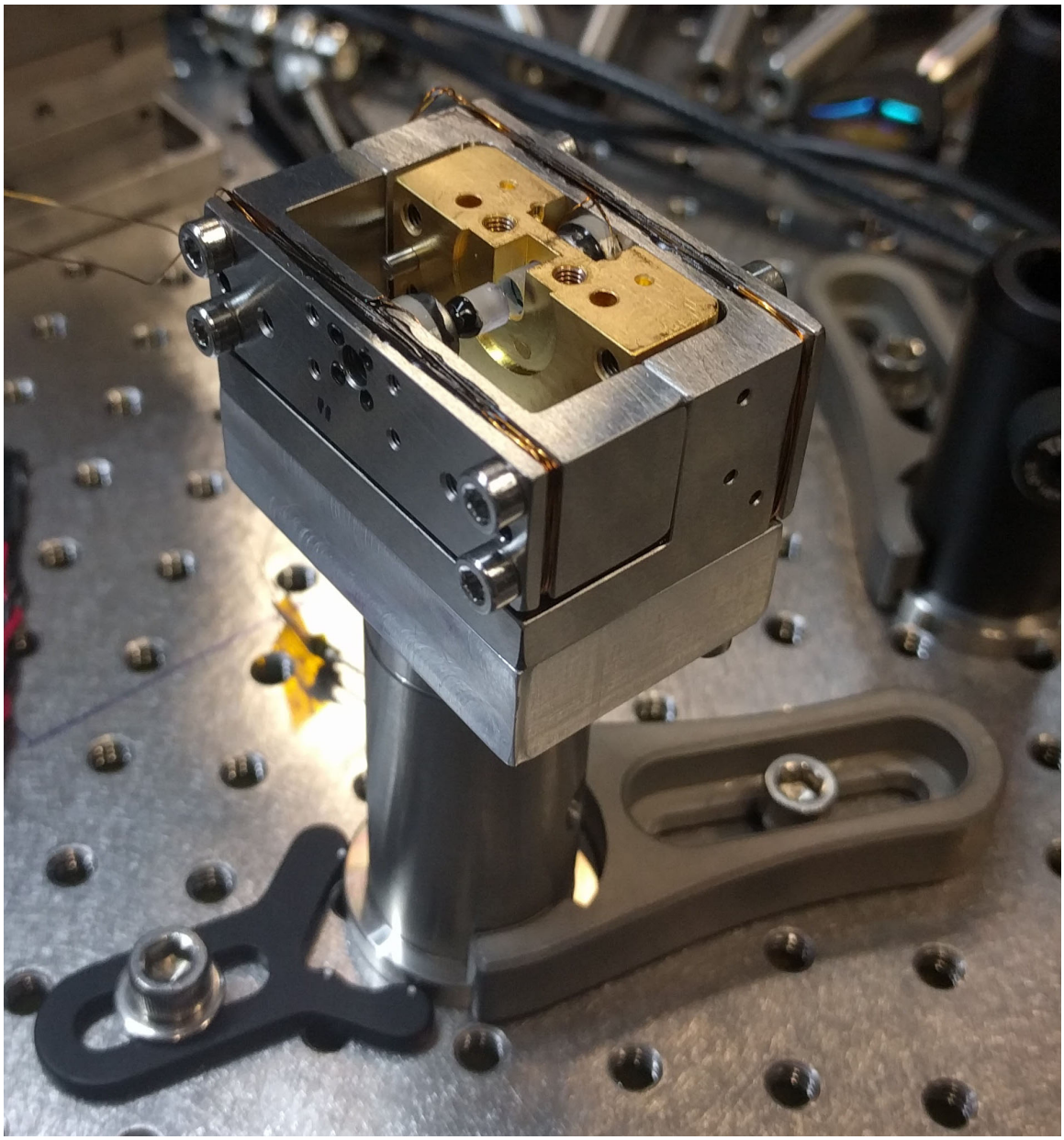

Figure 5.11: Wireless converter with only optical cavity spacer and half of the microwave cavity bottom installed. Optical cavity mirrors are visible, as is the circular pocket where the flip chip is inserted and directly epoxied according to previous alignment procedures. All parts made of invar, but the microwave cavity parts are Au-coated for higher electrical conductivity.

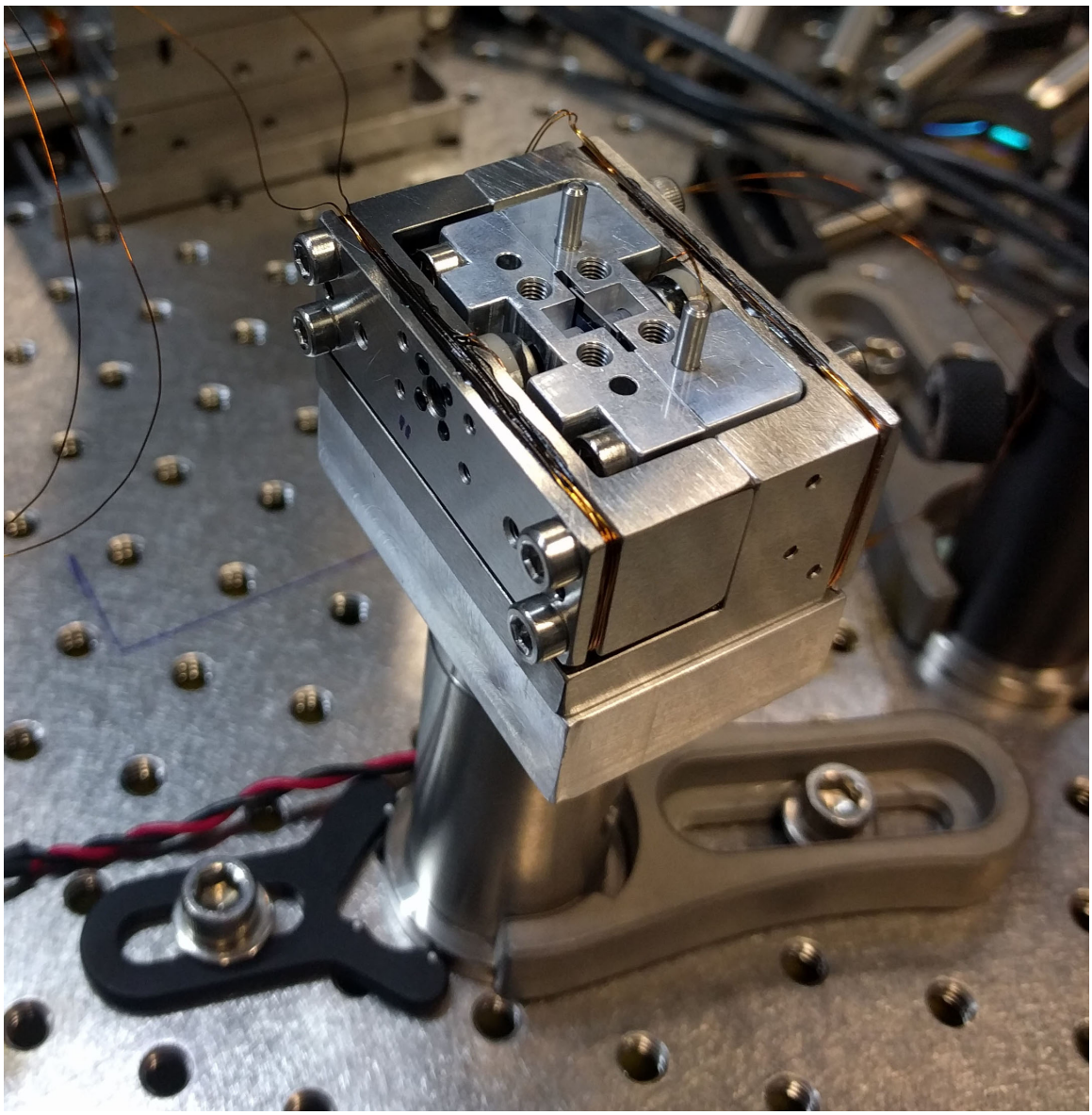

Figure 5.12: The first demonstration of membrane alignment and epoxying in the wireless converter design. The microwave cavity bottoms are test pieces made of Al, not invar. After epoxying the membrane, the curved mirror (front) was removed so the second half of the microwave cavity bottom could be installed. After replacing the curved mirror, the converter is ready for installation of the microwave hat.

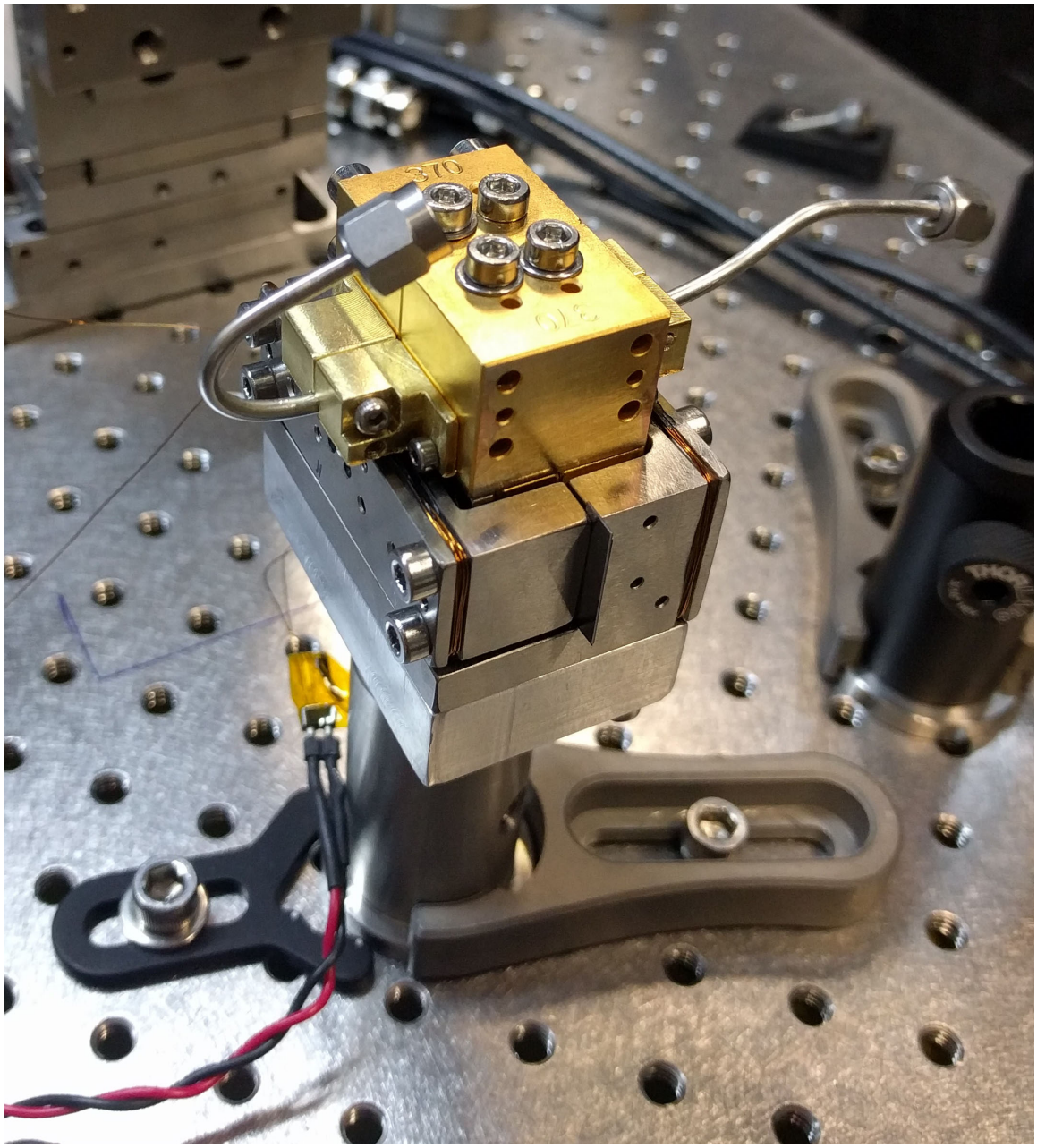

Figure 5.13: The complete wireless converter, with all optical and microwave components assembled. The two coaxial lines are for reflection and transmission measurements.

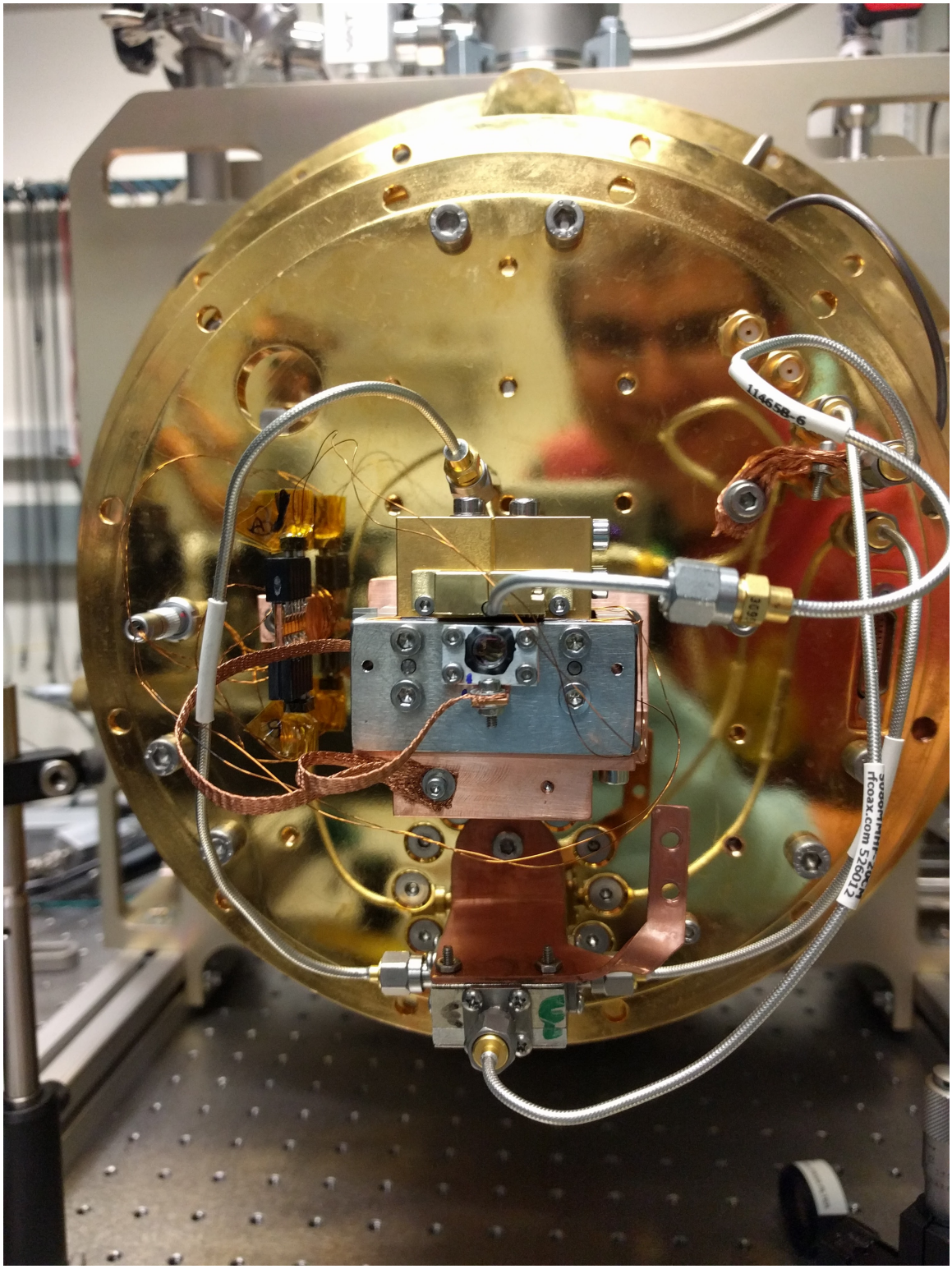

Figure 5.14: Wireless converted installed at the base plate of an optical access dilution refrigerator. Visible in the center of the optical cavity spacer is a lens which limits divergence of the free-space beam coupled to the cavity mode. Author's reflection on the Au-coated Cu base plate.

Chapter 6

Optomechanical experiments

This chapter will cover my main experimental work on optomechanical systems not related to microwave to optical conversion. In particular, it will focus on our demonstration of sideband cooling a mechanical mode's temperature to the quantum backaction limit [3]. This demonstration has broader relevance because it signifies a regime where the mechanical resonator's dynamics are dominated by the coherent coupling to the light field and its quantum noise, thus the decoherence from its connection to a thermal bath becomes negligible. Such a regime enables future work on the microwave to optical conversion experiment, demonstrating that the converter could operate in a quantum-enabled regime to perform tasks such as transferring quantum states or generating entanglement between microwave and optical light. A perspective of past work will also be given, with an emphasis on how previous scientific results, such as observing RPSN, generating squeezing light, or performing sideband thermometry, can now be used as a suite of powerful calibration techniques for subsequent experiments. Our work on reaching the backaction limit used measurements of all of these phenomena to directly calibrate or cross-check measurements, making discussion of these past results a natural part of the story.

6.1 Background

The concept of using radiation pressure as a tool to manipulate mechanical motion arose decades ago in the context of gravitational wave detection[12, 13]. This initial work demonstrated that a harmonically-bound object buffeted by electromagnetic radiation (there, a UHF field inside

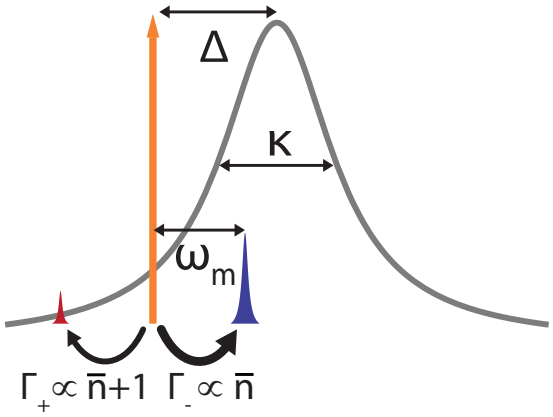

Figure 6.1: Frequency-space diagram depicting optomechanical sideband cooling. The cooling laser (orange) excites both Stokes (red) and anti-Stokes (blue) sidebands separated by the mechanical frequency ω_m, whose amplitudes are suppressed or enhanced by the cavity susceptibility (gray, real part, FWHM κ). Due to the quantum nature of the scattering process, the red sideband rate is proportional to $n+1$, while the blue sideband is proportional to n. This asymmetry is the source of the quantum backaction limit, where the red sideband remains at a constant finite amplitude, defining a synthetic thermal bath of the light whose temperature the mechanical mode cannot be cooled below. Adapted from Ref. [3]

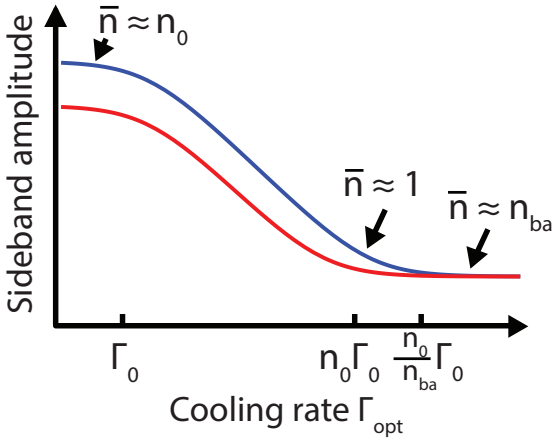

Figure 6.2: Successive regimes of optomechanical sideband cooling. While $\Gamma_{\rm opt} < \Gamma_{\rm m}$, sideband amplitude is given by cavity susceptibility while no cooling takes place. For $\Gamma_{\rm opt} > \Gamma_{\rm m}$, the ratio of sideband amplitudes remains fixed but the mode temperature decreases (classical regime). When $\Gamma_{\rm opt} = n_{\rm th}\Gamma_{\rm m},$, the mechanical mode approaches the ground state ($\bar{n} = 1$). Finally, at $\Gamma_{\rm opt} = (n_{\rm th}/n_{\rm ba})\Gamma_{\rm m}$ backaction and thermal forces on the system are equal. Beyond this is the quantum backaction limit, where the equal red and blue sidebands imply the mechanical mode is in thermal equilibrium with the synthetic thermal bath provided by the shot noise of the light. Adapted from Ref. [3]

a cavity) can be subject to additional engineered dissipation. Subsequent theoretical investigation focused on the quantum nature of this process: does the random arrival of individual photons (shot noise) disturb the measurement or control process? In fact, this random backaction force, called radiation pressure shot noise (RPSN), is a fundamental limit of optical position measurement [18]. In the context of optomechanical sideband cooling, backaction is better conceptualized as a temperature, defined by the shot noise fluctuations inside the optical cavity, below which the mechanical mode cannot be cooled. More specifically, cooling to the quantum backaction limit is the end of the line for sideband cooling with a coherent state, in that cooling below n_{ba} is not possible without employing more sophisticated techniques such as using squeezed light [96].

To briefly review the relevant theory, a red-detuned cooling laser will contribute additional optomechanical damping Γ_{opt} to the mechanical mode, thus lowering its temperature from that of its thermal bath $n_{\mathrm{th}} = \frac{kT_{\mathrm{m}}}{\hbar\omega_m}$ (to which it has a coupling Γ_{m}). The damped resonator's temperature $\bar{n}$ is given by

$$\bar{n} = \frac{n_{\mathrm{th}}\Gamma_{\mathrm{m}} + n_{\mathrm{ba}}\Gamma_{\mathrm{opt}}}{\Gamma_{\mathrm{m}} + \Gamma_{\mathrm{opt}}} \tag{6.1}$$

where n_{ba} is the backaction limit, describing the effective thermal bath of the shot noise fluctuations of the light inside the optical cavity. Sideband cooling is the result of a balance between the red sideband, which heats the resonator but is suppressed by the off-resonant cavity susceptibility, and the blue sideband, which cools the resonator and is resonantly enhanced by the cavity susceptibility (Fig. 6.1). The backaction limit is given by

$$n_{\mathrm{ba}} = -\frac{(\omega_m + \Delta)^2 + (\kappa/2)^2}{4\omega_m\Delta} \tag{6.2}$$

which is simply a function of sideband resolution, as clearly illustrated in the case of optimal detuning, where $n_{\mathrm{ba}} = (\kappa/4\omega_m)^2$ [50, 51]. While the optical damping Γ_{opt} is dependent on detuning, it is operationally trivial to achieve the same amount of damping for a variety of Δ by adjusting the optical power of the cooling laser.

While other methods of detection allow determination of the mechanical mode temperature $\bar{n}$ with proper calibration, using heterodyne detection to independently measure red and blue

mechanical sidebands is convenient since it allows for direct thermometry of the mechanical mode via sideband asymmetry when the temperature is near the quantum regime $\bar{n} \approx 1$ [97, 52, 54, 53, 55, 56]. The various regimes of sideband behavior are shown in Fig. 6.2. In the first two, $\Gamma_{\rm opt}$ is either smaller or larger than $\Gamma_{\rm m}$; in both cases the ratio of sideband amplitudes is given by the cavity susceptibility, and sideband cooling is present in the latter case. As $\Gamma_{\rm opt} = n_{\rm th}\Gamma_{\rm m}$, the mode is near the ground state as the sideband ratio begins to change. At $\Gamma_{\rm opt} = \frac{n_{\rm th}\Gamma_{\rm m}}{n_{\rm ba}}$, backaction and thermal motion contribute equally, while beyond this is the quantum backaction limit, where backaction is the dominant force on the system. Sideband amplitudes are equal because the mechanical mode is in thermal equilibrium with the synthetic bath provided by the shot noise of the light.

6.2 Cooling to the quantum backaction limit

The simplified experimental setup is shown in Fig. 6.4 (a more detailed schematic is given below). A red-detuned cooling laser is injected into the 10 ppm-transmission mirror of a $\kappa = 2\pi \times 2.6$ MHz optical cavity coupled to the motion of the $\omega_m = 2\pi \times 1.48$ MHz mechanical mode of a Si_3N_4 drumhead resonator (500 μm x 500 μm x 40 nm), and collected in transmission from a 100-ppm mirror by a heterodyne receiver. A second locking laser is injected in the orthogonal polarization mode, and actively stabilizes the cavity length and laser frequency. The optomechanical cavity, described in detail in Chapter 4, is mounted to the base plate of a dilution refrigerator. The mechanical mode is coupled to a thermal bath $n_{\rm th}$, whose temperature need not correspond to the bulk temperature of the base plate (but can be directly measured in this experiment), with a very small mechanical decay rate $\Gamma_{\rm m} = 2\pi \times 0.18$ Hz, measured via observing the ringdown of a mechanical excitation driven by a piezo actuator. This measurement is performed optically with a 904 nm diode laser. At this wavelength, the cavity mirrors do not have a high finesse, meaning optomechanical effects such as damping the mechanical motion are absent.

By collecting the transmitted light in heterodyne detection, the red and blue sidebands are directly visible (Figs. 6.4, 6.7). By performing a simultaneous fit to both sidebands at $\omega_{\rm het} \pm \omega_m$ (where $\omega_{\rm het}$ is the heterodyne frequency), and using the off-resonant shot noise as an absolute cal-

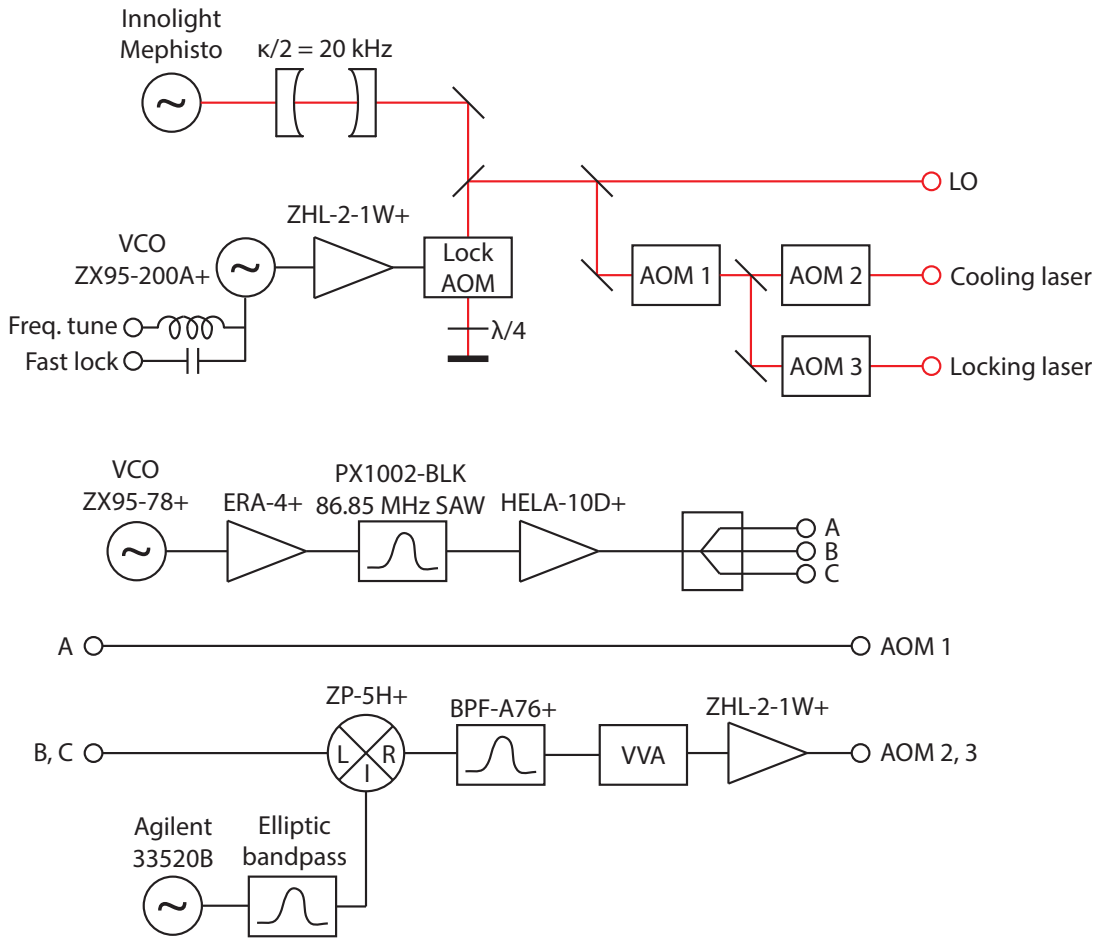

Figure 6.3: Detailed rf and laser schematic. Top: The 1064nm laser light is produced, sent through a filter cavity, and sent through the lock AOM (acousto-optic modulator) in a double-pass configuration to stabilize it to the optomechanical cavity. After this, it is split into several parts which form the LO, cooling laser, and locking laser after passing through a series of AOMs. Bottom: rf setup for producing the tones driving AOMs 1, 2, and 3. An 86 MHz tone is filtered and split, where two paths are modulated by ∼10 MHz tones whose difference is the cooling-locking laser detuning. The frequency of modulation of the AOM 2 is the heterodyne frequency. This setup has low noise near ω_m, and can be easily converted to homodyne operation. Because AOMs 2 and 3 select the opposite order of AOM 1, noise or drift in the VCO is common-mode and is not written onto the light.

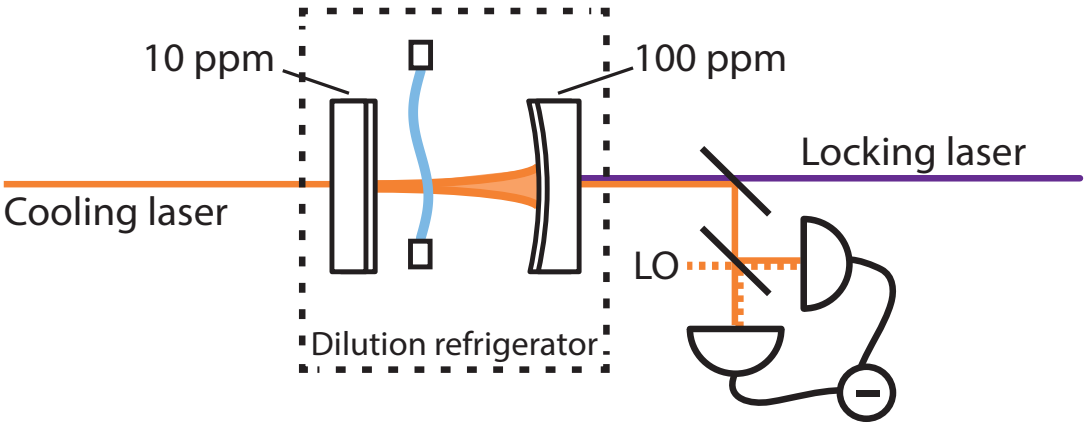

Figure 6.4: Essential experimental setup. The cooling laser is injected into the optomechanical cavity. The transmitted light is sent into a heterodyne receiver along with a local oscillator (LO). The locking laser is injected in the opposite direction and measured in reflection to perform Pound-Drever-Hall stabilization of the cavity. Adapted from Ref. [3].

ibration of sideband amplitude, sideband thermometry can immediately be performed. By taking the ratio of red to blue sideband amplitudes, R, as a function of the increasing optical damping $\Gamma_{\rm opt}$, the amplitude ratio due to cavity susceptibility only, s, can be extrapolated at $\Gamma_{\rm opt} = 0$. (Equivalently, the detuning Δ could be determined directly and s calculated for each cooling experiment.) The temperature of the mode is then $\bar{n}^{-1} = (R/s) - 1$. Thus, for each cooling experiment, s determines Δ (with κ and ω_m independently measured).

An exceptional cooling experiment is shown in Figs. 6.4, 6.7, where the extracted sideband heights and the inferred mode temperature $\bar{n}$ are shown, respectively. The signature of the quantum backaction limit is clear in Fig. 6.4, which parallels the expectation given in Fig. 6.2 as the sideband amplitudes shift from being in ratio according to the cavity susceptibility to being equal. By inferring the mode temperature $\bar{n}$, it is clear in Fig. 6.7 that the temperature asymptotically approaches $n_{\rm ba}$ as expected. The final point in the cooling curves corresponds to $\bar{n} = 0.20 \pm 0.02$, for an expected $n_{\rm ba} = 0.18$. The cooling experiment can be repeated at a variety of detunings (Fig. 6.8), which demonstrates the nature of the quantum backaction limit. Increased sideband resolution as the cooling laser moves from near resonance to further red detuned lowers $n_{\rm ba}$, consistent with the expectation of Eqn. 6.2.

6.3 Classical laser noise and beam preparation

The essential problem of the optical and rf design of this experiment is to prepare laser light with as little classical amplitude and phase noise near ω_m as possible. With lasers required on resonance, red detuned from resonance, and as a heterodyne LO, the technical task is to produce clean laser tones with 1 MHz and 10 MHz detunings from each other. Our approach is illustrated in Fig. 6.3, where the optical and rf subsystems to produce the lasers used in the experiment are detailed. All laser beams are sourced from a InnoLight Mephisto 1064nm continuous-wave source, which is sent through a 40 kHz filter cavity (filtering the noise at 20 kHz), all but ensuring shot-noise limited performance at noise frequencies from the carrier near ω_m. Unfortunately, the light must be further manipulated, which can add noise. All the light is sent through an AOM in double-pass

configuration to shift the frequency to follow the optomechanical cavity. From this point, the light is split to form the several lasers used in the experiment. A copy is kept unaltered to serve as an LO (its noise performance being critical to good detection). From this point, the remainder of the light is sent through a series of AOMs to implement the following scheme: By passing the light through two AOMs in series, selecting opposite scattering orders in each crystal, shifts in frequency from dc to 10 MHz are possible. This is done to two beams (with both using the same AOM 1 for the first shift) in the following scheme. The cooling laser's frequency relative to the LO (the heterodyne frequency f_{het}) is set by $f_{\text{het}} = f_{\text{AOM2}} - f_{\text{AOM1}}$, while the detuning of the cooling beam from resonance (more precisely, from the locking laser, which can be within 10s of kHz of resonance depending on how the lock is tuned) is given by $f_{\text{AOM3}} - f_{\text{AOM2}}$. By looking at the bottom of Fig. 6.3, the procedure for generating the rf tones that run the AOMs is detailed. They use an 86 MHz tone from a VCO as a common-mode source, filtered by a commercially available SAW filter built for the obsolete 2G wireless phone standard. As an aside, in the VHF band in which our AOMs operate, there is typically only one SAW filter commercially available in any useful frequency range. Despite their very narrow bandwidth (25 kHz), the necessity of multiple tones with 1-10 MHz spacing requires other solutions. Discrete inductors and capacitors cannot make a high-enough Q filter to appreciably attenuate noise at ω_m from the carrier, and VHF cavity filters, notwithstanding their technical design considerations, are roughly the size of a beer keg and are extremely unwieldy. Our solution has been to dodge the problem by mixing clean signals near 10 MHz up to the VHF band, where other than filtering mixer images there is no need for additional filtering. The generation of 10 MHz signals is done using digital function generators, typically Agilent 33520Bs. While they have many undesirable noise characteristics, including harmonic and non-harmonic spurs, these can be filtered using hand-built elliptic bandpass filters resonantly tuned to attenuate exactly at ω_m to either side of the carrier. We achieve 20 dB of attenuation at the mechanical sidebands, with 3 dB of insertion loss for the carrier (Fig. 5.9). Once mixed onto the VCO signal, and after filtering the image sideband and residual carrier, the tone is sent through a voltage-variable attenuator (optional for laser intensity stabilization; our preferred lower-noise

technique is to instead feed back to an EOM crystal to modulate the polarization going into a polarizing beamsplitter near 45°. After a power amplifier, the signal is directly sent to the AOM. This beam preparation scheme produces light with amplitude (phase) noise 0.2% (2%) of shot noise at 5 μW, a representative power needed to reach $\bar{n} = n_{\mathrm{ba}}$.

A corresponding more-detailed optical schematic describing the optical setup of the experiment itself is shown in Fig. 6.5. It corresponds to a slightly idealized version of the setup that can be used for both the current backaction cooling experiment, as well as ongoing microwave to optical experiments. In the experiment described in this chapter, the damping beam is denoted in yellow, and operates in transmission. For other experiments where operation in reflection is desired, the beampath in red can be used, which also is detected by the heterodyne receiver. A corresponding version of this setup has been used in subsequent work employing homodyne detection [31]. In this scheme, the rf electronics detailed in Fig. 6.3 are modified by adding a mixing stage to channel A equivalent to those in channels B and C. This allows for cooling and locking laser frequencies ~ 1 MHz from the LO, and a copy of the LO (called the signal beam) can be used as an on- or near-resonant probe. For quantum measurement applications where a large total collection efficiency is critical, the factor of two greater efficiency of homodyne detection is very useful. Like the cooling laser in the backaction cooling experiment, the signal beam is injected into the cavity from behind (yellow beampath in Fig. 6.5) to obtain a clean signal in transmission. Now, with the cooling laser moved to operate in reflection for microwave to optical experiments (Chapter 7), the signal beam also serves to assist in alignment and calibration of the optical cavity operated in reflection.

6.4 Further analysis of classical and substrate noise effects on sideband thermometry

A qualitative suggestion that classical noise is not significant is the fact that the cooling curves saturate at the expected n_{ba}. Given the levels of classical laser noise on the cooling laser, an analysis of the sideband thermometry procedure used to calculate $\bar{n}$ was performed including the effects of classical nose [54, 53, 70, 97]. It was found that the contribution was $\Delta\bar{n}^{\mathrm{laser}} = 0.006$,

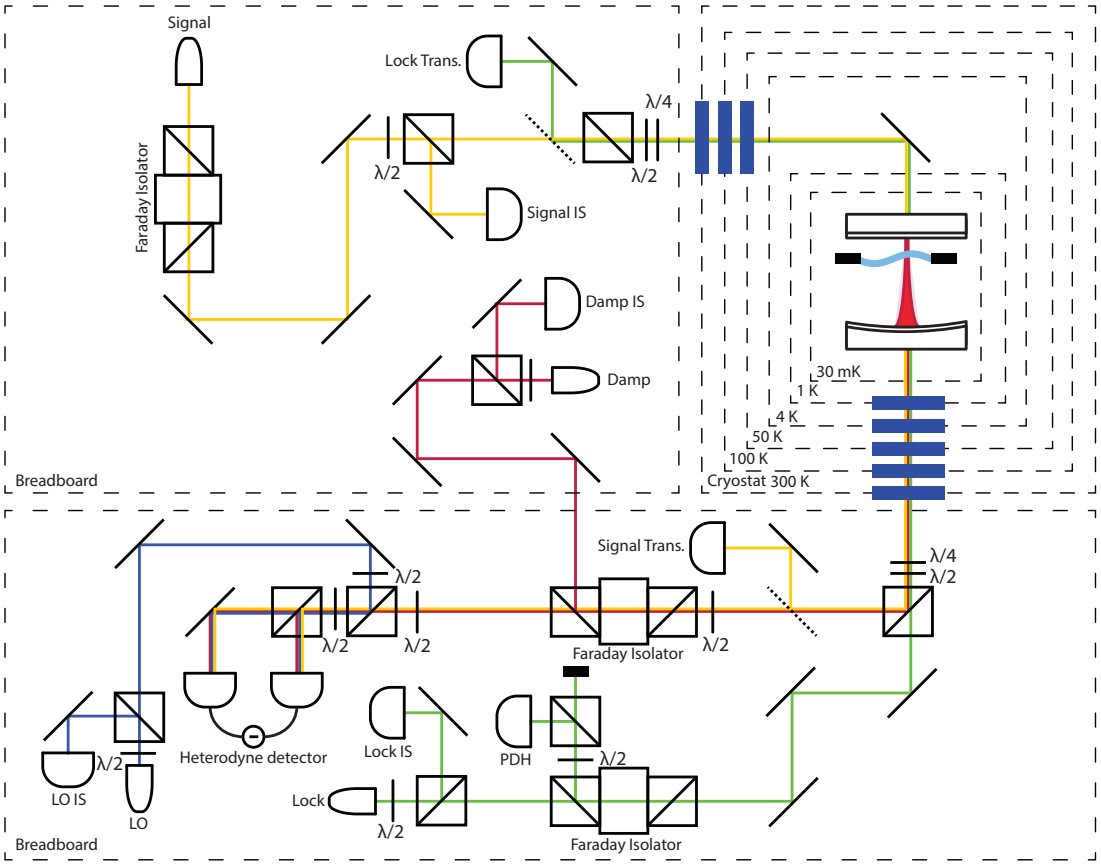

Figure 6.5: Detailed optical schematic representative of both the backaction-limit cooldown, as well as ongoing microwave to optical conversion experiments (Chapter 7). Beams are denoted as follows: the lock beam is green, the LO beam is blue, the damping beam (in reflection, used now for microwave to optical conversion) in red, and the signal beam (either the damping beam moved to be injected in the rear, or a separate beam made from splitting the LO) in yellow. Dashed mirrors are flip mirrors used for alignment or auxiliary detection. The optical setup is on two breadboards to facilitate access to the cryostat. The bottom breadboard is routinely removed and relocated via position retainers on the posts that support it.

smaller than the statistical error in our fits of $\Delta\bar{n} = 0.02$. An additional source of noise is off-resonant mechanical modes whose noise power rides on top of shot noise [19, 98, 91], affecting the normalization of sideband amplitudes to the (assumed) off-resonant shot noise level. This is visible in the last points of Fig. 6.7, where the higher off-resonant levels result in artificially lower normalized sideband heights. But because sideband thermometry relies on the ratio of sideband amplitudes, to first order this has a small effect on determination of $\bar{n}$. An analysis finds a systematic error of $\Delta\bar{n}^{\mathrm{sub}} = 0.006$, of the same magnitude as classical laser noise and thus not a significant source of error. An additional check on the magnitude of possible systematic error is that the mechanical sidebands (Fig. 6.7 inset) retain a lorentzian lineshape [70]. That these two main sources of systematic error are small suggests that the simple calculations of sideband thermometry are appropriate, and that this error analysis need not be represented elsewhere in the Chapter to give context to results.

6.5 Characterizing the mechanical mode's thermal bath using RPSN

Characterization of the membrane mode's thermal bath was an important step in transitioning to dilution refrigerator operation. In previous work at 4 K, it was found that the membrane effectively thermalized to the bulk temperature of the cryostat cold finger. This assumption would not necessarily hold true at millikelvin temperatures, as thermal conductivities are much lower and the cooling power of the cryostat is far less. Sideband asymmetry measurements allow for straightforward measurement of the mechanical decoherence rate $n_{\mathrm{th}}\Gamma_{\mathrm{m}}$, which in conjuction with a mechanical ringdown measurement to determine Γ_{m}, directly determines the bath temperature. Comparison to the bulk temperature, as measured by a ruthenium oxide thermometer on the mixing chamber of the dilfridge, is a first-order answer to whether the optomechanical cavity, and in particular the membrane, has thermalized. However, the locking laser, even at injected powers of half a microwatt, can still contribute enough RPSN to be a significant component of the membrane's thermal bath. By varying the lock power (Fig. 6.9), the effect of RPSN on temperature can be assessed. Specifically, the linear dependence of the bath temperature n_{th} on lock power can

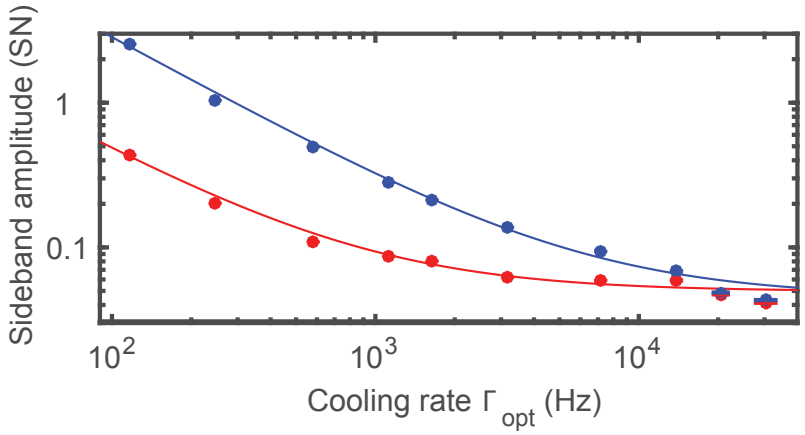

Figure 6.6: Red and blue sideband amplitudes captured in heterodyne detection. Sideband amplitudes are normalized to the off-resonant level, which is assumed to be shot noise. At low Γ_{opt}, the amplitudes differ due to the ratio of cavity susceptibility at each frequency, while at high Γ_{opt} they become equal when the mechanical mode is in thermal equilibrium with the light field. The last two points are below the expectation because of off-resonant excess mechanical noise which distorts the normalization. Adapted from Ref. [3].

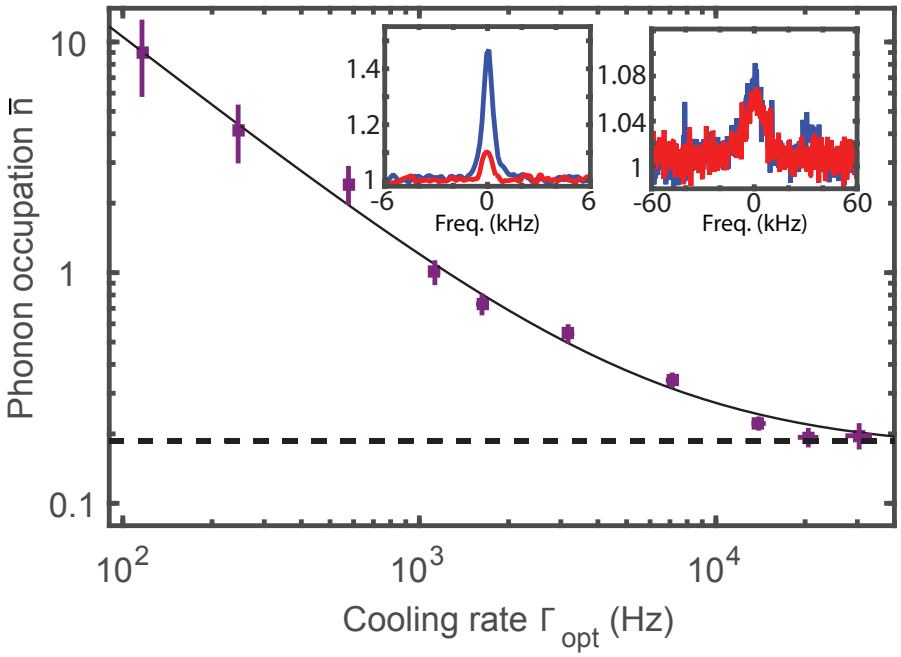

Figure 6.7: A cooling curve near optimal Δ, demonstrating cooling of the mechanical mode to the quantum backaction limit. Insets show superimposed spectra of red and blue sidebands fro the third (left) and third-to-last (right) points on the cooling curve. Adapted from Ref. [3].

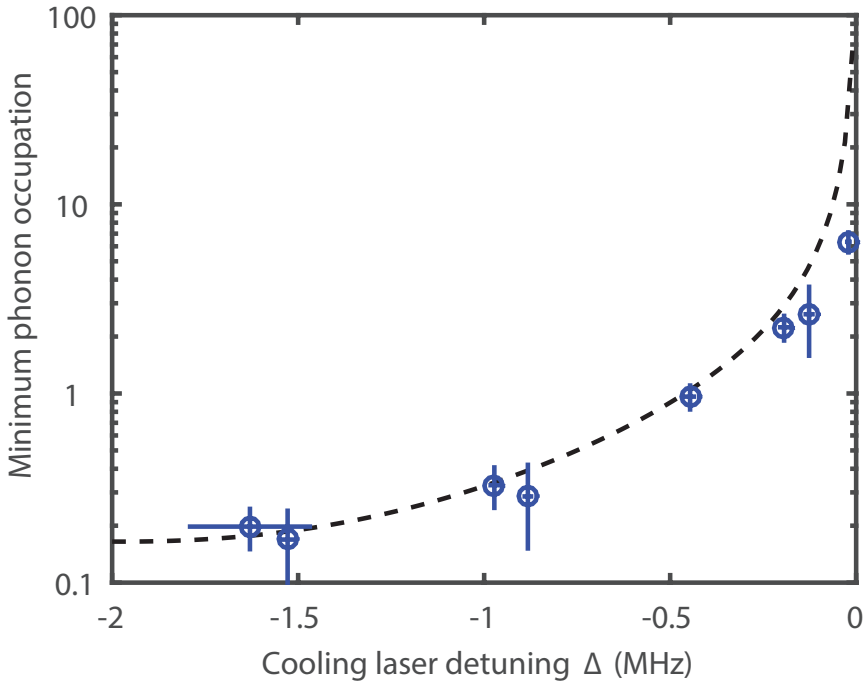

Figure 6.8: The minimum phonon occupation reached as Δ is varied from near resonance to its optimal value. Near resonance, n_{ba} diverges. Adapted from Ref. [3].

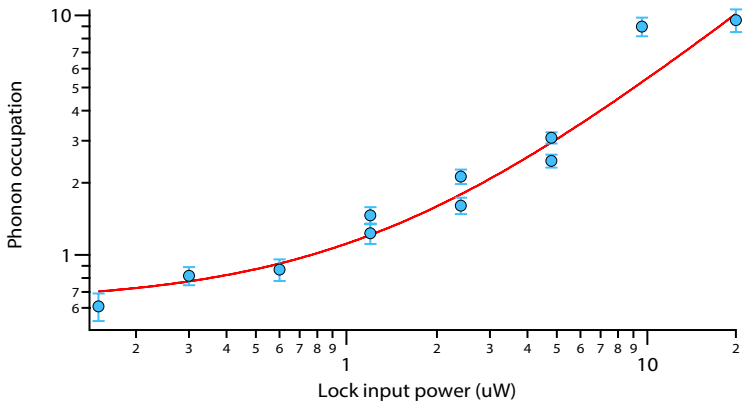

Figure 6.9: An uncalibrated measurement of RPSN. For a fixed cooling beam power (here just under $\bar{n} = 1$), increasing the near-resonant locking beam power appears to "heat" the resonator as its backaction force on it increases. Typically, the y-axis is calibrated in units of position spectral density, and the x-axis is calibrated relative to the SQL power. Without calibration, it is clear that the RPSN grows to 10 times the thermal motion.

be fit and used to determine the fraction of the bath temperature due to RPSN. It was found that of the total effective bath temperature of 360 mK, the thermometer accounted for 70 mK, RPSN of the locking laser accounted for 166 mK, with 96 mK left over. In fact, RPSN was the dominant thermal bath of the membrane. Subsequent work to improve optical aligment and detection allowed for operation with much lower locking laser powers in the hundreds of nanowatts, where the RPSN contribution is less substantial.

A check on the main result is to use RPSN to increase the bath temperature of the mechanical mode while still attempting to cool to the quantum backaction limit. In Fig. 6.10, a cooling curve is taken under nominal conditions (orange), and with additional locking laser power (green). Though technical noise prevented increasing Γ_{opt} much further, the cooling curve still follows a trend of asymptotically approaching n_{ba}.

6.6 Determining the quantum efficiency of detection by measuring squeezed light

It should not be surprising that a cavity that can be cooled to quantum backaction limit would be able to generate strong ponderomotive squeezing. A thought experiment suggests red

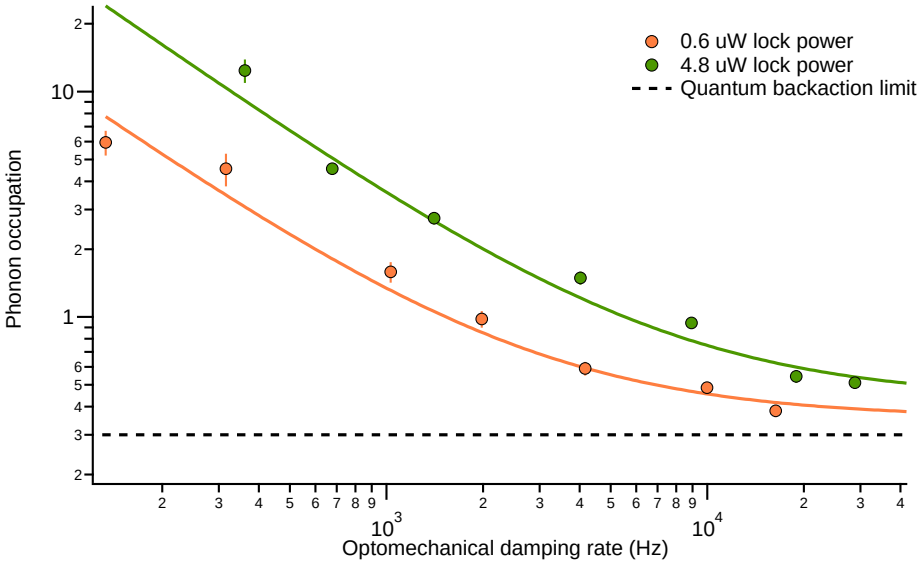

Figure 6.10: Cooling to the quantum backaction limit with two bath temperatures. The orange curve was taken under the same conditions as the main data result. By increasing the lock power, the additional RPSN increases the bath temperature. By comparing the fractional increase of the lock power to the fractional increase of the bath temperature n_{th}, the component of the bath temperature due to RPSN can be determined.

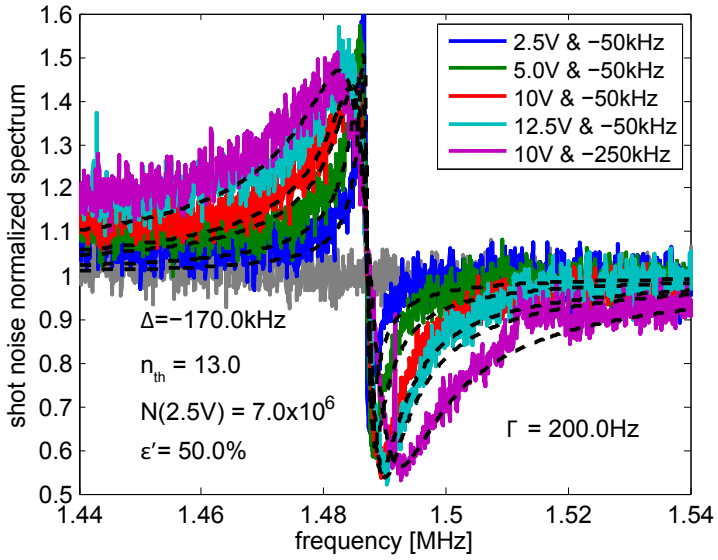

Figure 6.11: Superimposed spectra of optomechanically squeezed light produced in the backaction limit experiment. This light was collected via direct photodetection, as opposed to heterodyne detection as used in the rest of the experiment. Increasing the power of the locking beam saturates the amount of squeezing, indicating the regime where measurement quantum efficiency ϵ' dominates. By fitting these curves, ϵ' is determined to be 0.50, which can be related to the corresponding value ϵ in the main experiment.

and blue sidebands ought to be highly correlated: Imagine that the resonator is cooled into its ground state. A shot noise fluctuation drives a Stokes scattering process, where the resonator heats up by one phonon, and a red photon is emitted from the cavity. Because of the very strong coherent coupling, the resonator is very quickly cooled back into its ground state, and the cavity emits a blue photon in short succession. The average temperature of the resonator is essentially the duty cycle of this process, and if it is sufficiently smaller than $\bar{n} = 1$, the two photons are emitted with very strong correlations. While this describes the correlations in the sidebands of the transmitted cooling laser, the same regime should be accessible with the near-resonant laser used in squeezing experiments.

Detection of optomechanically squeezed light can be a powerful calibration tool, since the amount of squeezing is directly related to the total quantum efficiency of the detection. In principle, squeezing could be measured with the heterodyne receiver, however, the experimental setup did not have the heterodyne phase locked (since when collecting power in red and blue sidebands, it is sufficient to let the phase drift and average over all values). The simplest way to detect squeezed light is in direct photodetection. With the near-resonant laser (operationally the locking laser) slightly red detuned, the squeezing, which normally occurs in the phase quadrature of the light, is rotated into the amplitude quadrature which can be measured in direct detection. This entails a slightly modified readout chain, since at some point before the usual heterodyne receiver, the transmitted light from the cavity is split off onto a photodetector. This can be useful in practice since it separates the heterodyne visibility, and any differences in propagation loss can be easily calibrated out. By using the locking beam to drive the cavity to produce squeezed light, we can directly calibrate the detection efficiency ϵ. In Fig. 6.11, with a fixed cooling laser power, the lock power is increased, giving the successive superimposed lineshapes measured in direct detection. With knowledge of the mechanical resonator's damped linewidth and temperature from sideband asymmetry measurements, fits to a model can extract the collection efficiency of the squeezing measurement, ϵ'. In this regime, thermal effects are small compared to collection efficiency, which quickly saturates in almost all of the traces in Fig. 6.11. We find $\epsilon' = 0.50$, consistent with our

Table 6.1: Ratio of radiation pressure to thermal forces in selected publications, in order of publishing date.

Paper Ref.	NJP [19]	RPSN [22]	Squeezing [68]	Backaction limit [3]	Variational readout [31]
R_s	0.091	1.2	5.1	14	3.4

determination of $\epsilon = 0.04$ from the sideband asymmetry measurements in the main experiment. With additional propagation losses of 5% to the heterodyne receiver, a visibility of 0.42, and a factor of 0.5 for a heterodyne measurement, we have $0.5 \times 0.95 \times 0.42^2 \times 0.5 = 0.04$. This verifies that extracting ϵ from the sideband asymmetry measurement is viable and accurate.

6.7 Historical trajectory of device performance

By quantifying the performance of successive devices, a big-picture trend can be seen which informs understanding of current and future capabilities. Table 6.1 shows the performance of notable results in terms of the ratio of radiation pressure to thermal forces, R_s,

$$R_s = \frac{C}{n_{\mathrm{th}}} \frac{1}{1 + (2\omega_m/\kappa)^2} \tag{6.3}$$

The trend is that after publication of initial work in the radiation-pressure dominated regime, the most important quantum measurement publications demonstrate an increasing level of radiation pressure forces dominating the dynamics. Work such as the initial publication on efficient microwave to optical conversion is not in the quantum regime ($R_s = 0.0011$ for noise measurements), although as an initial demonstration of a new technology, one expects it not to be as developed in performance as concurrent work on well-understood systems [42]. As a single metric, it does not tell the entire story of the relevance of individual works. For example, one of our latest publications reports a measurement sensitivity of 5.3 times the SQL, the lowest to our knowledge, and also demonstrates sensitivity off the mechanical resonance below the SQL for its quantum efficiency [31]. These claims, which benefit from both a large R_s as well as a large ϵ are not fully represented in our choice of R_s as a metric.

6.8 Comment on operation in an optical-access dilution refrigerator

This experiment benefited from the much lower bath temperature provided by a dilution refrigerator. Even though this first attempt exhibited a higher bath temperature than that of the bulk cryostat temperature, subsequent work has reduced the magnitude of the RPSN of the locking laser and other auxiliary effects to a level where the mechanical mode can now thermalize to a temperature very close to the bulk as read out via standard cryogenic thermometry. However, choice of our dilution refrigerator design involved much consideration and design work. Initial work I performed on characterizing the 4 K system used for the microwave to optical conversion project informed us that LN2-jacketed bath cryostats produce significant vibrational noise power, even at MHz frequencies, due to turbulence in the liquid as it boils off. At the time, low-vibration pulse-tube technology was in its early stages (and to this day a sub-kelvin low-vibration pulse-tube cryostat simply does not exist). We selected a cryostat built by Cryoconcept that was engineered for optical access by tipping the conventional dilution refrigerator design on its side [99]. The first model was built for a group at LKB in Paris, and its use is described in Ref. [100]. The design allows for thermal contraction to occur along the optic axis, nearly eliminating optical misalignment during cooldown. A side port allows transmission measurements via a 45° mirror mounted at the 4 K stage. A LHe bath and vapor-cooled shields allow for very low vibration compared to other options. The windows were custom-designed by us to achieve the desired thermal performance, using a thermal model to calculate the attenuated 300 K blackbody heat load after passing through the fused silica substrates used for our cold windows, which are placed at the still, 4 K, and both vapor-cooled stages [101]. The use of 1 cm diameter apertures in the windows restricts the solid angle to a level where, combined with the partial attenuation of the fused silica, the heat load at base is only a few microwatts. Moving a shutter that blocks the rear optical access (and associated blackbody radiation) while cold resulted in no increase of the 30 mK base temperature of the refrigerator.

Chapter 7

Electro-optomechanical experiments

7.1 Description via transfer matrix formalism, scattering parameter measurement

The derivation of transfer functions between microwave, optical, and mechanical inputs/ouputs in Chapter 2 establishes a measurement and characterization concept that is directly translatable to experiment. Specifically, by producing coherent excitations with a network analyzer, the input ports of the converter can be probed, and the desired output field's response can be detected and compared to a reference in the network analyzer. By using upper sideband modulation on either the microwave or optical pump, and heterodyne detection of the desired output field to isolate the upper sideband response, the measurement directly corresponds to the transfer function element such as $t_1 = \xi_{a_{\mathrm{out,L}},b_{\mathrm{in,R}}}$ linking the annihilation operators of the particular elements in $\mathbf{a}_{\mathrm{in}}$ and $\mathbf{a}_{\mathrm{out}}$ (here the microwave input and the optical output). This is the process responsible for potentially noiseless transduction between the input and output modes. The transfer fuction's particular form is given by Eq. 2.22, which looks like an optical cavity in transmission, with the relative strengths of the coherent coupling rates Γ_{e} and Γ_{o} determining an impedance-matching condition, and their sum determining the bandwidth of conversion. The transfer function linking lower-sideband excitations (creation operators) represents the amplification or entanglement mode of the device, while cross terms capture nonideal performance. In particular, the element $\xi_{a^{\dagger}_{\mathrm{out,L}},b_{\mathrm{in,R}}}$, representing upconversion of the upper-sideband signal to the lower sideband of the optical pump, corresponds to gain (or equivalently added noise) in the conversion process, placing a fundamental limit on how noiseless

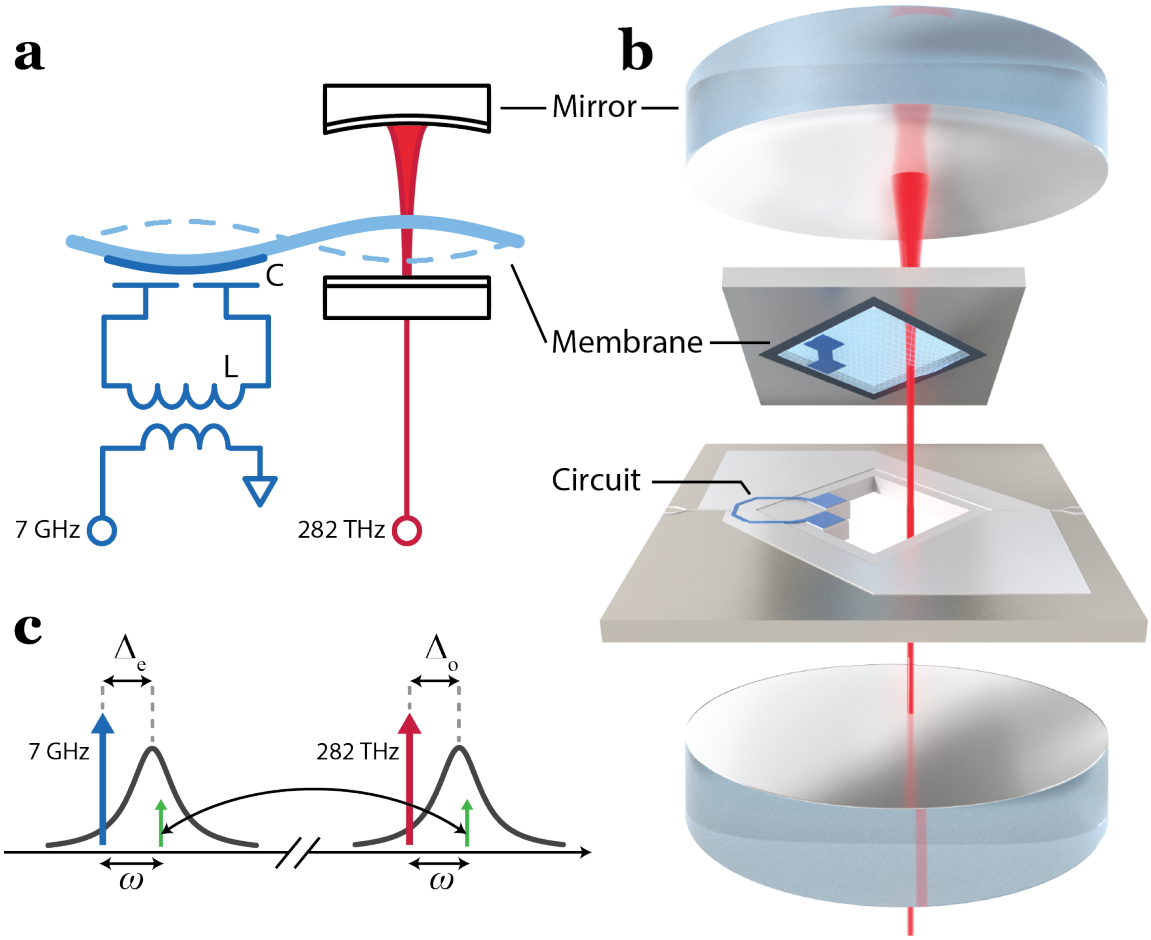

Figure 7.1: a.) Schematic of converter, consisting of an LC circuit and an optical cavity coupled to the same Si_3N_4 drumhead resonator. b.) Frequency-domain picture of the two electromagnetic resonators, the electrical and optical pump tones, and the upper-sideband tone to be upconverted or downconverted. c.) Rendering of the system, showing the optical cavity mirrors, which contain a membrane chip, and a second chip which capacitively coupled to membrane motion via a patterned superconducting Nb circuit. Adapted from Ref. [42].

the converter can be. This process is suppressed in the resolved sideband regime ($2\omega_m > \kappa_{\{e,o\}}/2$) by the two electromagnetic cavities, but plays a finite role in any practical experiment. The effective gain implied by this process is given by Eq. 2.23, where in the following text useful simplifications are provided.

The measurement procedure consists of modulating the signal from a network analyzer (at rf frequencies near ω_m) as an upper sideband on the microwave or optical pumps, and demodulating the reflected pump signals to separate the upper and lower sidebands in detection (Fig. 7.2). The transfer functions of the converter are here referred to simply as t_1, t_2, r_1, and r_2 for reflection and transmission measurements, with $i = \{1, 2\}$ referring to probes originating from the microwave and optical ports, respectively. The question of calibrating out any loss or gain in the experimental setup leads to a interesting result, in that for measurements of t_1 and t_2, there is a calibration-free way to measure the symmetric transmission product $t_1 t_2$ via making four measurements. By moving the pumps far off cavity resonances ω_e and ω_o and making reflection measurements $r'_{1,\mathrm{off}}$ and $r'_{2,\mathrm{off}}$, where the prime denotes the raw, uncalibrated measurement, the electromagnetic cavities both have a reflectivity of 1 and we just measure any loss and gain in the measurement circuit. Then, we have

$$t_1 t_2 = \frac{t'_1 t'_2}{r'_{1,\mathrm{off}} r'_{2,\mathrm{off}}} \tag{7.1}$$

where by dividing out by the losses and gains, $t_1 t_2$ is obtained immediately. Reflection measurements do not benefit from such a trick, but by using a wide probe scan, the relative size of any reflection feature is easily obtained.

Our measurement system is now more sophisticated than our original work in Ref. [42]. In particular, it now has optical heterodyne detection, which can directly measure the desired upper sideband of the pump (rather than inferring it from a measurement of the photon number spectrum in direct photodetection). The converter has also been moved into a dilution refrigerator, substantially reducing the thermal environment n_{th} and potentially enabling quantum-limited performance. This new setup is reflected in Fig. 7.2, and shown in more detail in Fig. 7.3.

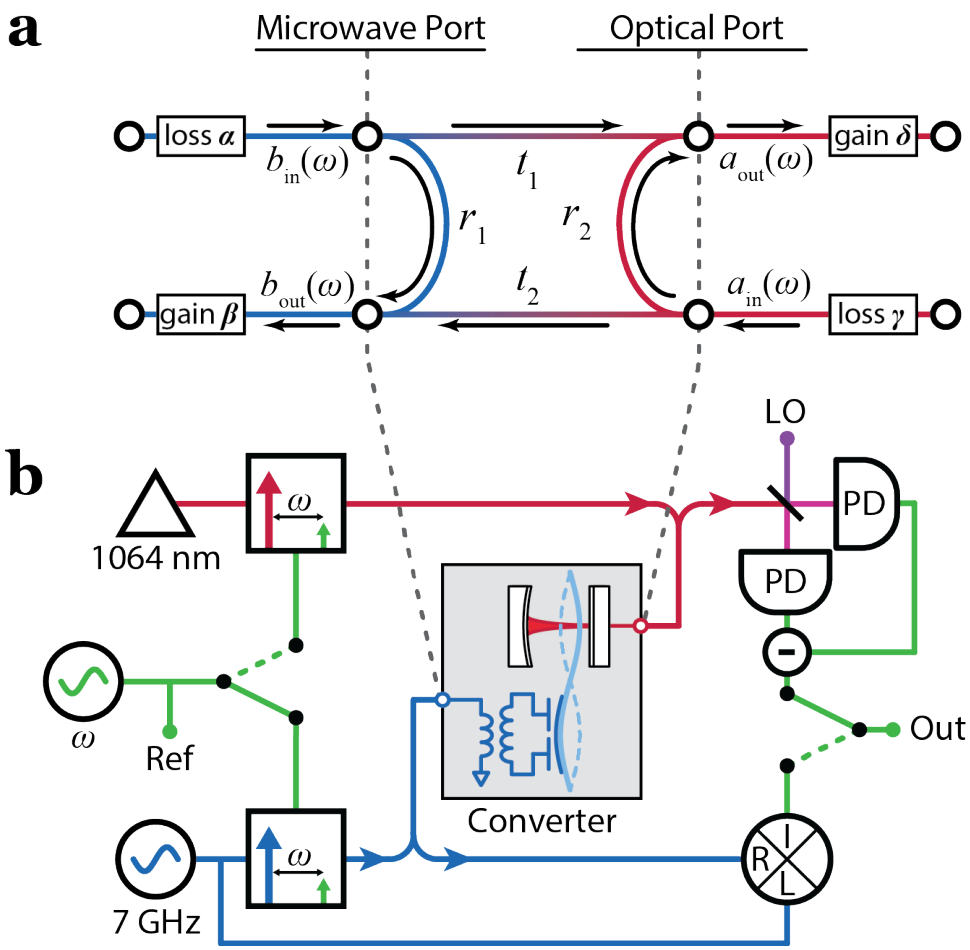

Figure 7.2: a.) Transfer function elements denoting transmission and reflection. Gain and loss in the measurement chain are denoted by α, β, γ, and δ. b.) Simplified experimental schematic. Adapted from Ref. [42]

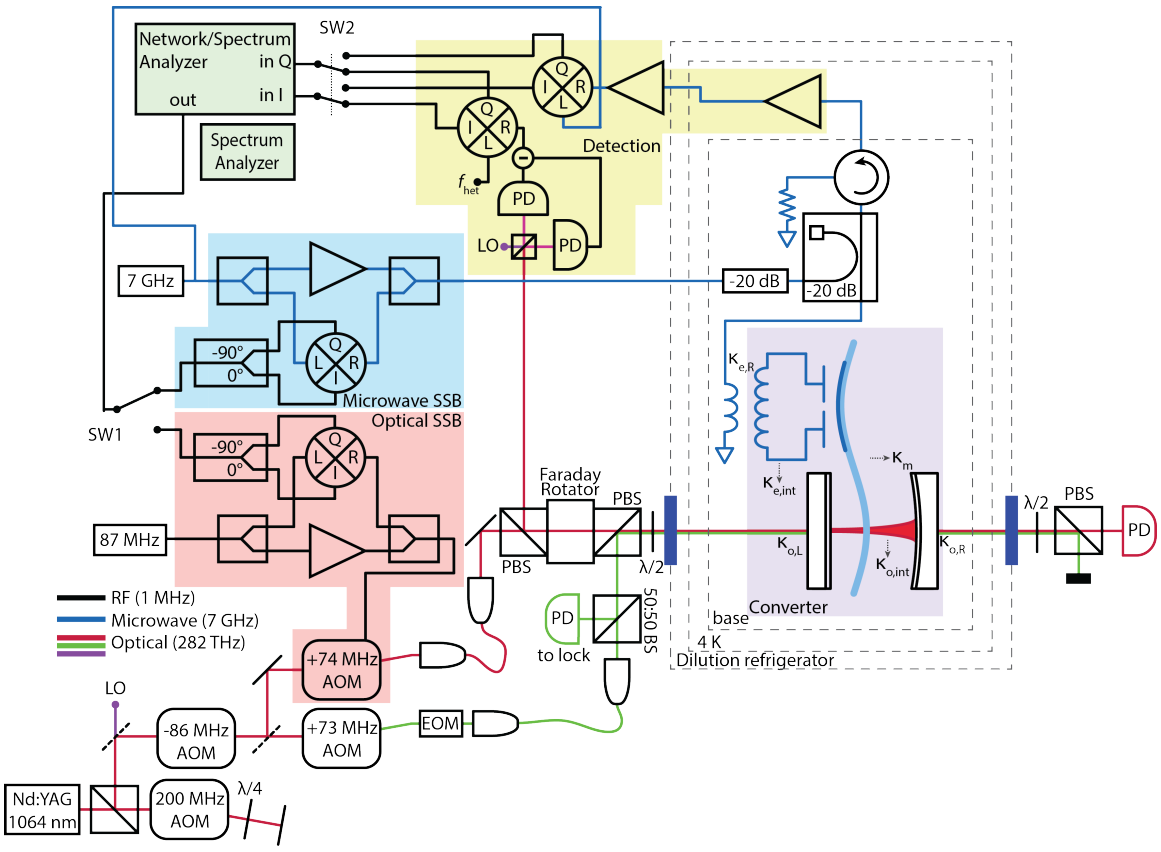

Figure 7.3: Detailed schematic of the converter measurement setup. This version can be compared to the original in the supplement to Ref. [42]: this setup now has optical heterodyne detection and a dilution refrigerator instead of a 4 K cryostat. For a more detailed representation of the optical setup, see Fig. 6.5.

7.2 Comments on modematching in heterodyne

While our original results required a calibration of the effective upper sideband amplitude due to measuring in direct detection, it turns out that this measurement scheme was ideal for measuring the modematching to the cavity ϵ. The modematching factor naturally appears symmetrically in the equations in Chapter 2 because it appears in optical probing and detection of the cavity. Specifically, only the modematched portion of the light drives the cavity, while in direct photodetection the modematching appears again due to the signal fluctuations beating only against the modematched portion of the optical carrier (see supplemental material in Ref. [92]). In heterodyne detection of the optical pump, the measurement of the conventional visibility η applies only to the total optical carrier, while the signal is (in general) emitted into a different spatial mode than the carrier. In effect, this breaks the parallelism of ϵ in the case of direct detection, which allows for the convenient calibration procedure given in Eq. 7.1. While ϵ still appears in the driving term, detection of the emitted signal is set by the overlap of the cavity mode to the local oscillator, not the pump laser. This value, distinct from the conventional η, we can call η', and can be determined by measuring the visiblity of a separate laser transmitted through the cavity from the other side against the local oscillator. Practically speaking, the correspondence $\epsilon \rightarrow \sqrt{\epsilon\eta'}$ should apply to heterodyne measurements of an imperfectly-modematched pump in reflection, although this requires a manual modification of the otherwise self-calibrating upconversion and downconversion efficiency measurements.

7.3 Original results

In this section, I will briefly review the results from our original experiment, which are detailed in both a paper and Reed Andrews's thesis [42, 92]. To clarify the differences between this original experiment and subsequent efforts, I will note that this used the original converter design detailed in Chapter 5 (as opposed to the wireless design), operated at 4 K (instead of 30 - 100 mK), and did not have optical heterodyne detection (though as I noted, the inferred

upper sideband amplitude was calculated and presented in the results). By scanning the probe tone ω across several mechanical modes ($\omega_{\mathrm{m}} = \{380, 560, 1240\}$ kHz), the different responses could be measured (Fig. 7.4). In particular, they differ in apparent efficiency of $|t_1 t_2|$ since they have appreciably different resolved sideband parameters, and thus different amounts of (undesirable) gain $\mathcal{A}$ (see Eq. 2.23). After accounting for $\mathcal{A}$, we infer a bidirectional efficiency of 0.086 ± 0.007, and a coherent transfer bandwidth of 30 kHz. Operating at a bath temperature of 4 K, we did not expect it to operate in the quantum regime. Its noise performance is shown in Fig. 7.5, where as the coherent couplings Γ_{e} and Γ_{o} are increased, the signal to noise increases (and thus added noise n_{vib} decreases).

7.4 Ongoing progress towards the quantum regime

Current work in the group is focused on bringing our converter devices into the quantum regime. The main improvement in this regard is to operate the converter in a dilution refrigerator, bringing the bath temperature from 4 K to 100 mK. My demonstration of backaction-limited cooling was the first time one of our optomechanical cavities was used in a dilution refrigerator; reaching the backaction limit demonstrates the same parameters necessary to convert quantum states. That suggests that reaching the quantum regime is possible for our devices. This section will describe ongoing progress towards that goal, including operation in a dilution refrigerator, incorporating new wireless cavity designs, and improving optical measurement via heterodyne detection.

The wireless converter has been operated a handful of times as the new design is being tested and characterized. Preliminary results show that improvements in conversion efficiency have been successful. The initial cooldown of the converter showed roughly the same $\sim 10\%$ efficiency, while the third cooldown showed a factor of two improvement, to 20%. This is primarily due to improvements in the optical cavity loss, and modematching of the pump beam to the optical cavity's spatial mode, both of which limited previous efficiency. The optical cavity, by using asymmetric mirror transmissions (7 ppm and 96 ppm instead of two 96 ppm mirrors in the first converter), has an improved collection fraction of 0.32, compared to 0.20 (internal loss still plays a large role),

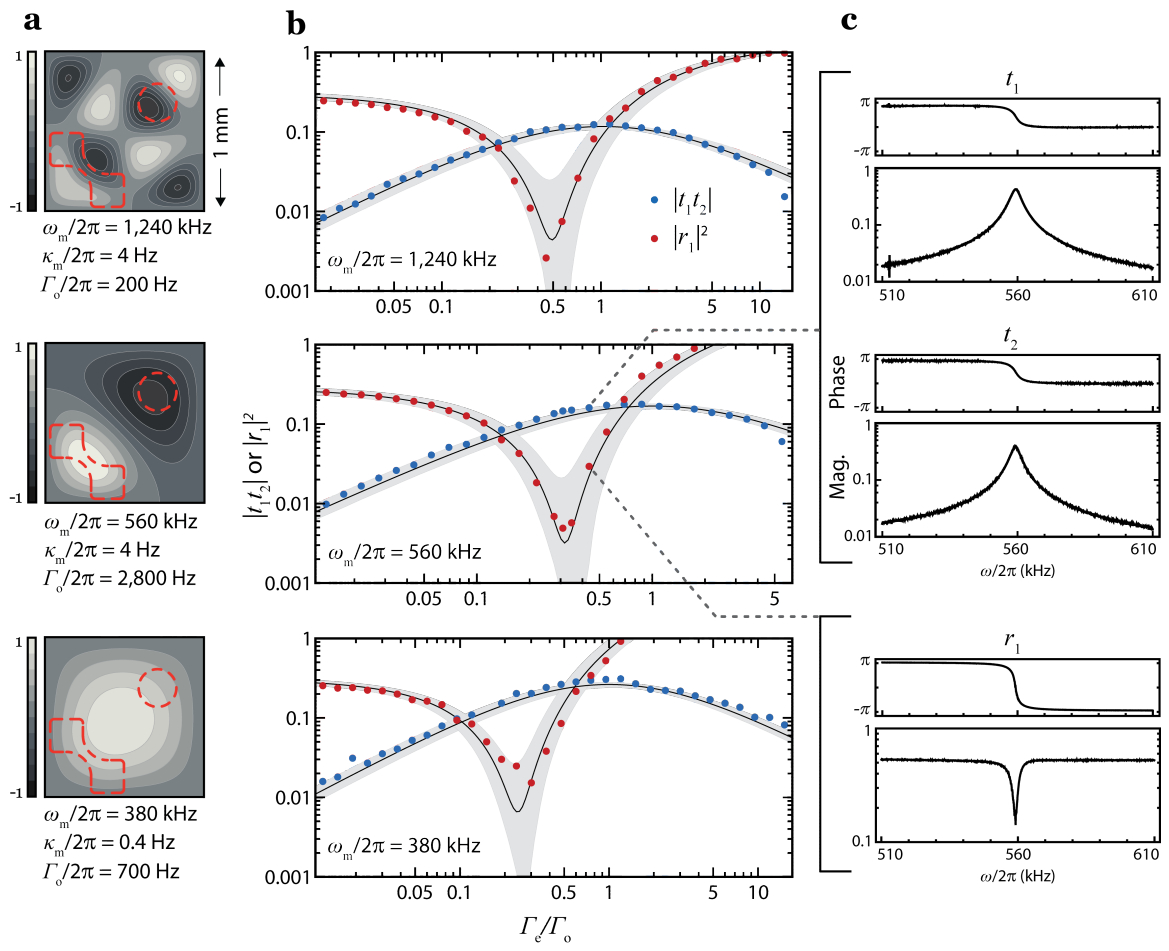

Figure 7.4: a.) Mechanical modeshapes of the modes used for conversion. b.) Power scan of the conversion sweeps, showing the impedance matching condition to maximize efficiency. c.) Individual upconversion and downconversion spectra showing amplitude and phase response. Adapted from Ref. [42].

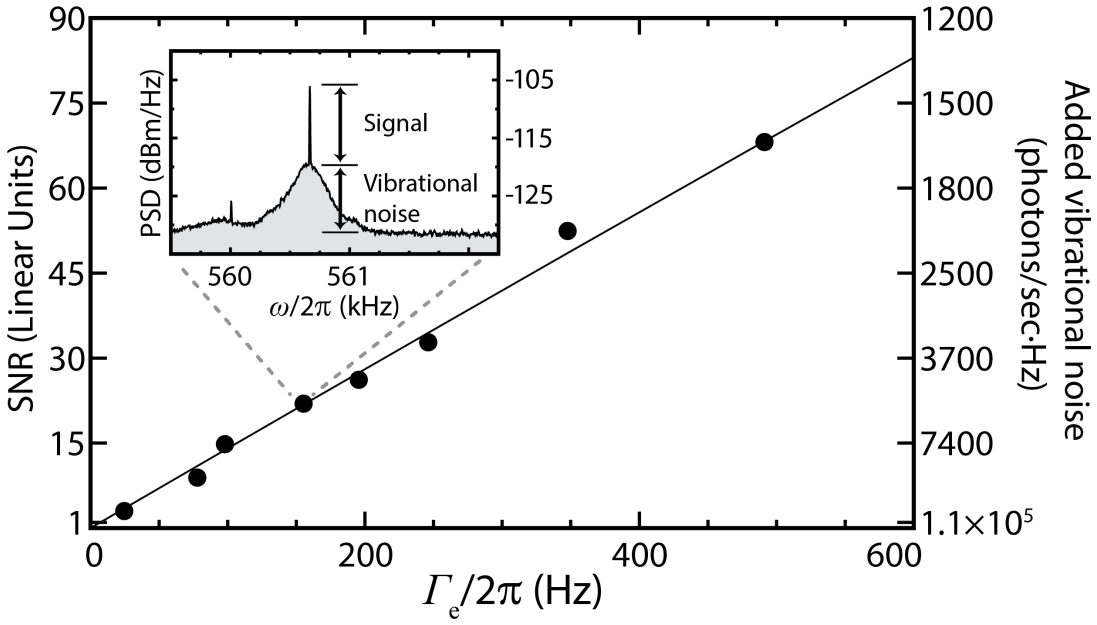

Figure 7.5: Added noise during upconversion at 4 K. Inset: Optical spectrum of upconverted microwave signal on top of damped thermomechanical motion. Adapted from Ref. [42].

while the optical modematching has been increased from 0.5 to 0.85.

The noise properties of the wireless converter are also much improved (due to operation in a dilution refrigerator), but are still not in the quantum regime. While the best parameters from various cooldowns would together allow for quantum-limited performance at $\Gamma_e + \Gamma_o \sim 10$ kHz, technical noise larger than the damped thermomechanical motion causes n_{vib} to saturate (Fig. 7.8). At this point, it is fair to say that ongoing efforts to test and refine the design of the wireless converter stand a good chance of overcoming these obstacles soon. Potential problems include scattered optical light causing loss (or noise) in the superconducting LC circuit, blackbody radiation, or parameter noise in the microwave circuit of other origin.

7.5 Future advances in detection of upconverted quantum states

The ultimate goal of a converter which can upconvert microwave quantum states to optical frequencies will require additional experimental tools to fully realize. While there is progress on many fronts, in particular the creation of on-demand microwave single photons that could serve as the input to the converter [102], the optical setup for detection at the single-photon level has not yet been demonstrated in our lab. The principal problem is to filter the large, coherent pump—which could have as many as 10^8 photons yet is only ω_m detuned in frequency—to allow for detection of single photons. With a frequency spacing in the MHz, an optical filter cavity is perhaps the only practical way to sufficiently filter out such a large signal. With high-quality mirrors commercially available at the < 10 ppm level for cavity ringdown spectroscopy applications [103, 104], such an application is feasible. Using 1 m ROC mirrors in a concentric configuration ($\ell \approx 2$ m), a $\mathcal{F} = 450,000$ cavity has a linewidth of $\kappa = 167$ Hz. Far off resonance, the suppression goes as $(\delta/\kappa)^2 = 3 \times 10^8$ for $\delta = 1$ MHz. This provides sufficient filtering of the pump, which would be reflected from the input mirror and, if necessary, prevented from propagating back into the converter using a Faraday isolator. The crosstalk of the isolator need not be as good as the cavity suppression, since it just needs to attenuate the reflected pump to be a small fraction of the pump driving the converter.

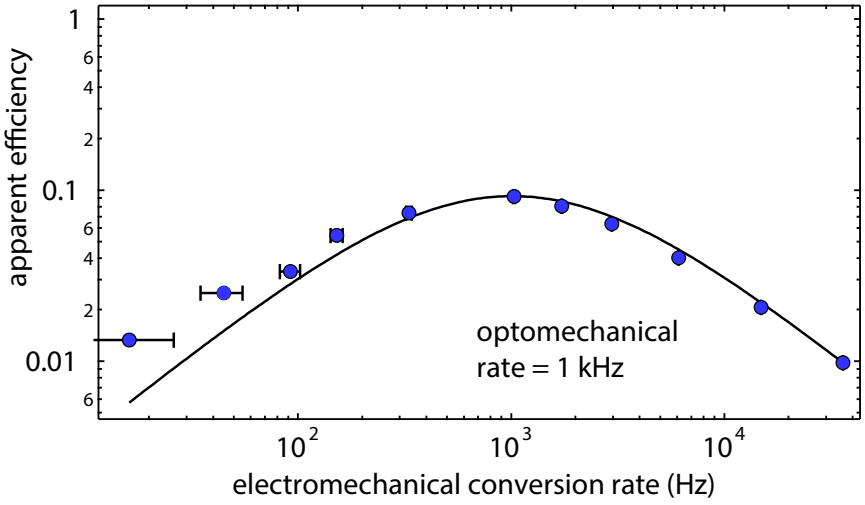

Figure 7.6: Power sweep for first cooldown with the wireless converter design. This achieved similar efficiency to our original converter, at approximately 10%.

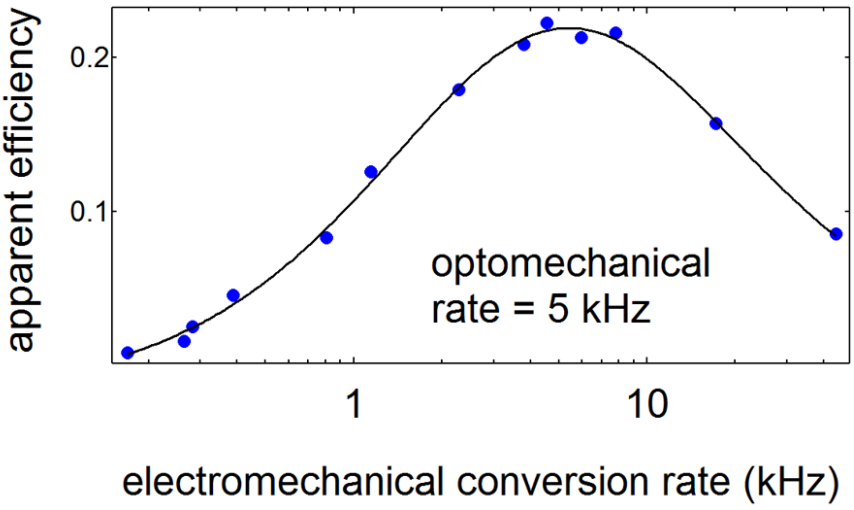

Figure 7.7: Power sweep for third cooldown with the wireless converter design. This achieved our best efficiency to date, approximately 20%.

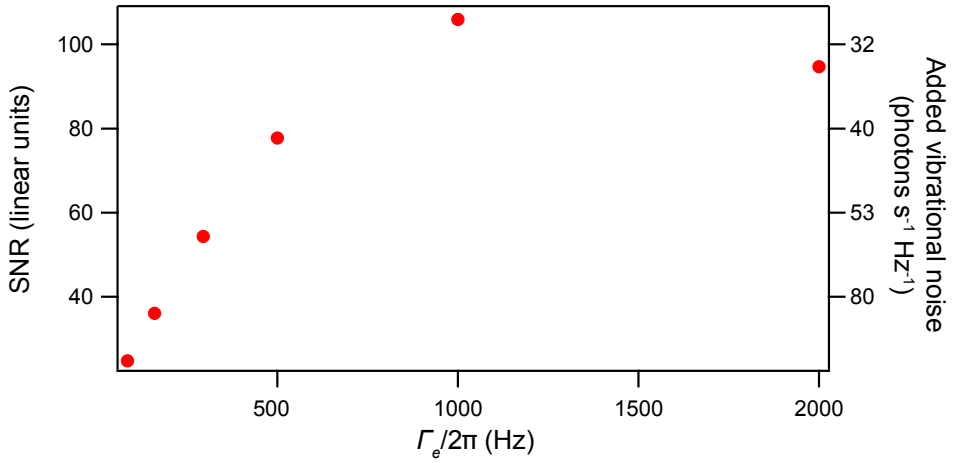

Figure 7.8: Added noise during the first cooldown of the wireless converter design. While much improved from previous results due to operation in a dilution refrigerator, the added noise is limited by technical noise particular to this cooldown, and is not in the quantum regime.

The more troublesome question in this scheme is how to stabilize the filter cavity without introducing additional photons that would be transmitted on cavity resonance. In the typical Pound-Drever-Hall technique, an fm-modulated laser on cavity resonance is used [105, 106]. While in principle the modulation depth could be set to exactly suppress the carrier, this would also reduce the amplitude of the error signal to zero. To reduce the effects of RPSN, we have worked to decrease the power necessary to lock our optomechanical cavities. Yet we still operate at the 100 nW level, which is equivalent to a pump of as many as 10^5 intracavity photons. Suppression at this level via polarization is beyond our usual level of control, but is possible in principle with Glan-Thompson polarizers, which claim an extinction ratio of 10^5. A dual-coating mirror could be used to lock the cavity using a different wavelength of light. This complicates the mirror coating design, although dichroic cleanup filters are commercially available with similar extinction to the best polarizers. A speculative idea to get around this problem is to use a double-barreled cavity which forms two adjacent spatial modes: one for actively stabilizing the cavity length, the second to serve as a seemingly passively-stable filter (Fig. 7.9). This has the benefit of reducing the optical crosstalk to zero, if it proves to be a practical idea.

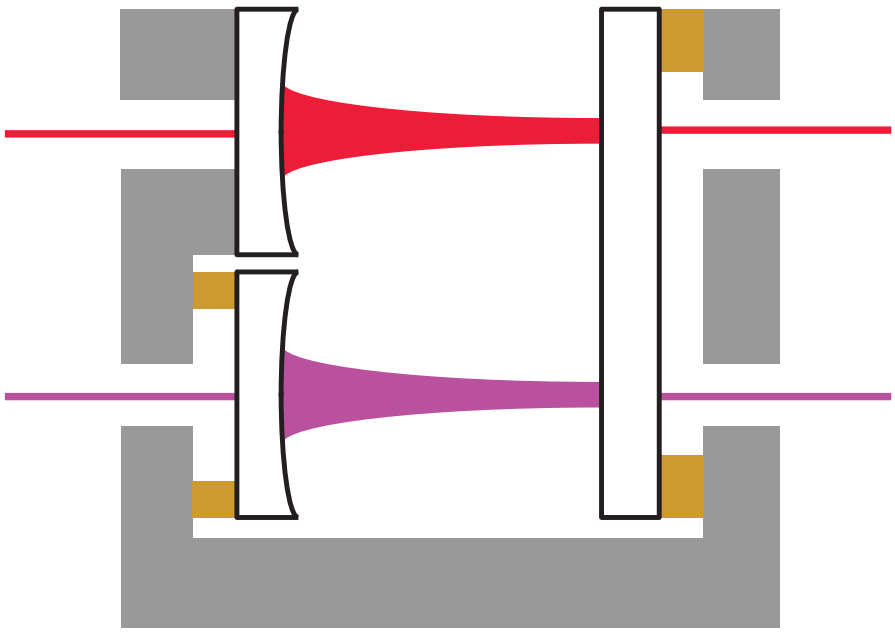

Figure 7.9: Speculative design for a double-barreled cavity, where one spatial mode (red) can be actively stabilized via a piezo actuator common to both cavity modes, thus stabilizing the other spatial mode (magenta) which can be scanned to the desired filter frequency with an additional piezo actuator.

Bibliography

[1] Vladimir B. Braginsky, Yuri I. Vorontsov, and Kip S. Thorne. Quantum nondemolition measurements. Science, 209(4456):547–557, 1980.

[2] Vladimir B. Braginsky and Farid Ya. Khalili. Quantum Measurement. Cambridge University Press, New York, NY, USA, 1992.

[3] R. W. Peterson, T. P. Purdy, N. S. Kampel, R. W. Andrews, P.-L. Yu, K. W. Lehnert, and C. A. Regal. Laser cooling of a micromechanical membrane to the quantum backaction limit. Phys. Rev. Lett., 116:063601, Feb 2016.

[4] Steven Chu, L. Hollberg, J. E. Bjorkholm, Alex Cable, and A. Ashkin. Three-dimensional viscous confinement and cooling of atoms by resonance radiation pressure. Phys. Rev. Lett., 55:48–51, Jul 1985.

[5] Dan M. Stamper-Kurn. Cavity optomechanics with cold atoms. In Markus Aspelmeyer, Tobias J. Kippenberg, and Florian Marquardt, editors, Cavity optomechanics, chapter 13, pages 283–325. Springer, Heidelberg, 2014. Preprint available at `https://arxiv.org/abs/1204.4351`.

[6] Andrew D. Ludlow, Martin M. Boyd, Jun Ye, E. Peik, and P. O. Schmidt. Optical atomic clocks. Rev. Mod. Phys., 87:637–701, Jun 2015.

[7] Immanuel Bloch, Jean Dalibard, and Wilhelm Zwerger. Many-body physics with ultracold gases. Rev. Mod. Phys., 80:885–964, Jul 2008.

[8] D. Leibfried, R. Blatt, C. Monroe, and D. Wineland. Quantum dynamics of single trapped ions. Rev. Mod. Phys., 75:281–324, Mar 2003.

[9] John Clarke and Frank K. Wilhelm. Superconducting quantum bits. Nature, 453(7198):1031–1042, 2008.

[10] R. J. Schoelkopf and S. M. Girvin. Wiring up quantum systems. Nature, 451(7179):664–669, 2008.

[11] M. H. Devoret and R. J. Schoelkopf. Superconducting circuits for quantum information: An outlook. Science, 339(6124):1169–1174, 2013.

[12] Vladimir Braginsky and A. B. Manukin. Ponderomotive effects of electromagnetic radiation. Journal of Experimental and Theoretical Physics, 25(4):653, 1967.

[13] Vladimir Braginsky, A. B. Manukin, and M. Y. Tikhonov. Investigation of dissipative ponderomotive effects of electromagnetic radiation. Journal of Experimental and Theoretical Physics, 31(5):829, 1970.

[14] Wikipedia. `https://en.wikipedia.org/wiki/The_Thing_(listening_device)`. Accessed: 15 March 2017.

[15] J. D. Teufel, T. Donner, Dale Li, J. W. Harlow, M. S. Allman, K. Cicak, A. J. Sirois, J. D. Whittaker, K. W. Lehnert, and R. W. Simmonds. Sideband cooling of micromechanical motion to the quantum ground state. Nature, 475(7356):359–363, 2011.

[16] Jasper Chan, T. P. Mayer Alegre, Amir H. Safavi-Naeini, Jeff T. Hill, Alex Krause, Simon Groblacher, Markus Aspelmeyer, and Oskar Painter. Laser cooling of a nanomechanical oscillator into its quantum ground state. Nature, 478(7367):89–92, 2011.

[17] V. Braginsky and S. Vyatchanin. Gravitational waves and the limiting stability of self-excited oscillators. Journal of Experimental and Theoretical Physics, 47(3):433, 1978.

[18] Carlton M. Caves. Quantum-mechanical radiation-pressure fluctuations in an interferometer. Phys. Rev. Lett., 45:75–79, Jul 1980.

[19] T. P. Purdy, R. W. Peterson, P.-L. Yu, and C. A. Regal. Cavity optomechanics with Si_3N_4 membranes at cryogenic temperatures. New Journal of Physics, 14(11):115021, 2012.

[20] Daniel W. C. Brooks, Thierry Botter, Sydney Schreppler, Thomas P. Purdy, Nathan Brahms, and Dan M. Stamper-Kurn. Non-classical light generated by quantum-noise-driven cavity optomechanics. Nature, 488:476–480, 8 2012.

[21] Amir H. Safavi-Naeini, Simon Grblacher, Jeff T. Hill, Jasper Chan, Markus Aspelmeyer, and Oskar Painter. Squeezed light from a silicon micromechanical resonator. Nature, 500:185–189, Aug 2013.

[22] T. P. Purdy, R. W. Peterson, and C. A. Regal. Observation of radiation pressure shot noise on a macroscopic object. Science, 339(6121):801–804, 2013.

[23] The LIGO Scientific Collaboration. A gravitational wave observatory operating beyond the quantum shot-noise limit. Nature Physics, 7:962–965, 2011.

[24] J. Aasi et al. Enhanced sensitivity of the ligo gravitational wave detector by using squeezed states of light. Nature Photonics, 7:613–619, 2013.

[25] Henning Vahlbruch, Moritz Mehmet, Karsten Danzmann, and Roman Schnabel. Detection of 15 db squeezed states of light and their application for the absolute calibration of photoelectric quantum efficiency. Phys. Rev. Lett., 117:110801, Sep 2016.

[26] E. Oelker, G. Mansell, M. Tse, J. Miller, F. Matichard, L. Barsotti, P. Fritschel, D. E. McClelland, M. Evans, and N. Mavalvala. Ultra-low phase noise squeezed vacuum source for gravitational wave detectors. Optica, 3(7):682–685, Jul 2016.

[27] A. Heidmann, Y. Hadjar, and M. Pinard. Quantum nondemolition measurement by optomechanical coupling. Applied Physics B, 64(2):173–180, 1997.

[28] H. J. Kimble, Yuri Levin, Andrey B. Matsko, Kip S. Thorne, and Sergey P. Vyatchanin. Conversion of conventional gravitational-wave interferometers into quantum nondemolition interferometers by modifying their input and/or output optics. Phys. Rev. D, 65:022002, Dec 2001.

[29] Thomas Corbitt, Yanbei Chen, Farid Khalili, David Ottaway, Sergey Vyatchanin, Stan Whitcomb, and Nergis Mavalvala. Squeezed-state source using radiation-pressure-induced rigidity. Phys. Rev. A, 73:023801, Feb 2006.

[30] S.P. Vyatchanin and E.A. Zubova. Quantum variation measurement of a force. Physics Letters A, 201(4):269 – 274, 1995.

[31] N. S. Kampel, R. W. Peterson, R. Fischer, P. L. Yu, K. Cicak, R. W. Simmonds, K. W. Lehnert, and C. A. Regal. Harnessing quantum correlations for physics beyond the standard quantum limit in broadband displacement detection, 2016.

[32] Jeremy L. O'Brien, Akira Furusawa, and Jelena Vuckovic. Photonic quantum technologies. Nature Photonics, 3:687–695, 2009.

[33] C. Langer, R. Ozeri, J. D. Jost, J. Chiaverini, B. DeMarco, A. Ben-Kish, R. B. Blakestad, J. Britton, D. B. Hume, W. M. Itano, D. Leibfried, R. Reichle, T. Rosenband, T. Schaetz, P. O. Schmidt, and D. J. Wineland. Long-lived qubit memory using atomic ions. Phys. Rev. Lett., 95:060502, Aug 2005.

[34] Iulia Buluta, Sahel Ashhab, and Franco Nori. Natural and artificial atoms for quantum computation. Reports on Progress in Physics, 74(10):104401, 2011.

[35] Stephan Ritter, Christian Nolleke, Carolin Hahn, Andreas Reiserer, Andreas Neuzner, Manuel Uphoff, Martin Mcke, Eden Figueroa, Joerg Bochmann, and Gerhard Rempe. An elementary quantum network of single atoms in optical cavities. Nature, 484(7393):195–200, 2012.

[36] M. D. Reed, L. DiCarlo, S. E. Nigg, L. Sun, L. Frunzio, S. M. Girvin, and R. J. Schoelkopf. Realization of three-qubit quantum error correction with superconducting circuits. Nature, 482(7385):382–385, 2012.

[37] Erik Lucero, R. Barends, Y. Chen, J. Kelly, M. Mariantoni, A. Megrant, P. O'Malley, D. Sank, A. Vainsencher, J. Wenner, T. White, Y. Yin, A. N. Cleland, and John M. Martinis. Computing prime factors with a Josephson phase qubit quantum processor. Nature Physics, 8(10):719–723, 2012.

[38] H. J. Kimble. The quantum internet. Nature, 453(7198):1023–1030, 2008.

[39] T. D. Ladd, F. Jelezko, R. Laflamme, Y. Nakamura, C. Monroe, and J. L. OBrien. Quantum computers. Nature, 464(7285):45–53, 2010.

[40] Mankei Tsang. Cavity quantum electro-optics. Phys. Rev. A, 81:063837, Jun 2010.

[41] Mankei Tsang. Cavity quantum electro-optics. II. input-output relations between traveling optical and microwave fields. Phys. Rev. A, 84:043845, Oct 2011.

[42] Reed W Andrews, Robert W Peterson, Tom P Purdy, Katarina Cicak, Raymond W Simmonds, Cindy A Regal, and Konrad W Lehnert. Bidirectional and efficient conversion between microwave and optical light. Nature Phys., 10:321–326, Mar 2014.

[43] Alfredo Rueda, Florian Sedlmeir, Michele C. Collodo, Ulrich Vogl, Birgit Stiller, Gerhard Schunk, Dmitry V. Strekalov, Christoph Marquardt, Johannes M. Fink, Oskar Painter, Gerd Leuchs, and Harald G. L. Schwefel. Efficient microwave to optical photon conversion: an electro-optical realization. Optica, 3(6):597–604, Jun 2016.

[44] Markus Aspelmeyer, Tobias J. Kippenberg, and Florian Marquardt. Cavity optomechanics. Rev. Mod. Phys., 86:1391–1452, Dec 2014.

[45] J.W. Harlow. Microwave Electromechanics: Measuring and Manipulating the Quantum State of a Macroscopic Mechanical Oscillator. PhD thesis, University of Colorado, Boulder, 2013.

[46] Warwick P. Bowen and Gerard J. Milburn. Quantum Optomechanics. CRC Press, Boca Raton, FL, USA, 2016.

[47] J. Kerckhoff. Power spectral densities of an optomechanical system, 2011. Internal technical note.

[48] Joseph Kerckhoff, Reed W. Andrews, H. S. Ku, William F. Kindel, Katarina Cicak, Raymond W. Simmonds, and K. W. Lehnert. Tunable coupling to a mechanical oscillator circuit using a coherent feedback network. Phys. Rev. X, 3:021013, Jun 2013.

[49] C. K. Law. Interaction between a moving mirror and radiation pressure: A Hamiltonian formulation. Phys. Rev. A, 51(3):2537–2541, March 1995.

[50] Florian Marquardt, Joe P. Chen, A. A. Clerk, and S. M. Girvin. Quantum theory of cavity-assisted sideband cooling of mechanical motion. Phys. Rev. Lett., 99:093902, Aug 2007.

[51] I. Wilson-Rae, N. Nooshi, W. Zwerger, and T. J. Kippenberg. Theory of ground state cooling of a mechanical oscillator using dynamical backaction. Phys. Rev. Lett., 99:093901, Aug 2007.

[52] A. J. Weinstein, C. U. Lei, E. E. Wollman, J. Suh, A. Metelmann, A. A. Clerk, and K. C. Schwab. Observation and interpretation of motional sideband asymmetry in a quantum electromechanical device. Phys. Rev. X, 4:041003, Oct 2014.

[53] M. Underwood, D. Mason, D. Lee, H. Xu, L. Jiang, A. B. Shkarin, K. Børkje, S. M. Girvin, and J. G. E. Harris. Measurement of the motional sidebands of a nanogram-scale oscillator in the quantum regime. Phys. Rev. A, 92:061801, Dec 2015.

[54] T. P. Purdy, P.-L. Yu, N. S. Kampel, R. W. Peterson, K. Cicak, R. W. Simmonds, and C. A. Regal. Optomechanical raman-ratio thermometry. Phys. Rev. A, 92:031802, Sep 2015.

[55] Seán M. Meenehan, Justin D. Cohen, Gregory S. MacCabe, Francesco Marsili, Matthew D. Shaw, and Oskar Painter. Pulsed excitation dynamics of an optomechanical crystal resonator near its quantum ground state of motion. Phys. Rev. X, 5:041002, Oct 2015.

[56] Justin D. Cohen, Sean M. Meenehan, Gregory S. MacCabe, Simon Groblacher, Amir H. Safavi-Naeini, Francesco Marsili, Matthew D. Shaw, and Oskar Painter. Phonon counting and intensity interferometry of a nanomechanical resonator. Nature, 520:522–525, Apr 2015.

[57] Jing Zhang, Kunchi Peng, and Samuel L. Braunstein. Quantum-state transfer from light to macroscopic oscillators. Phys. Rev. A, 68:013808, Jul 2003.

[58] L. Tian and Hailin Wang. Optical wavelength conversion of quantum states with optomechanics. Phys. Rev. A, 82:053806, Nov 2010.

[59] Sh. Barzanjeh, D. Vitali, P. Tombesi, and G. J. Milburn. Entangling optical and microwave cavity modes by means of a nanomechanical resonator. Phys. Rev. A, 84:042342, Oct 2011.

[60] Amir H Safavi-Naeini and Oskar Painter. Proposal for an optomechanical traveling wave phononphoton translator. New Journal of Physics, 13(1):013017, 2011.

[61] C. A. Regal and K. W. Lehnert. From cavity electromechanics to cavity optomechanics. Journal of Physics: Conference Series, 264(1):012025, 2011.

[62] Sh. Barzanjeh, M. Abdi, G. J. Milburn, P. Tombesi, and D. Vitali. Reversible optical-to-microwave quantum interface. Phys. Rev. Lett., 109:130503, Sep 2012.

[63] Lin Tian. Adiabatic state conversion and pulse transmission in optomechanical systems. Phys. Rev. Lett., 108:153604, Apr 2012.

[64] Ying-Dan Wang and Aashish A. Clerk. Using interference for high fidelity quantum state transfer in optomechanics. Phys. Rev. Lett., 108:153603, Apr 2012.

[65] Lin Tian. Robust photon entanglement via quantum interference in optomechanical interfaces. Phys. Rev. Lett., 110:233602, Jun 2013.

[66] S. A. McGee, D. Meiser, C. A. Regal, K. W. Lehnert, and M. J. Holland. Mechanical resonators for storage and transfer of electrical and optical quantum states. Phys. Rev. A, 87:053818, May 2013.

[67] José Capmany and Carlos R. Fernández-Pousa. Quantum model for electro-optical phase modulation. J. Opt. Soc. Am. B, 27(6):A119–A129, Jun 2010.

[68] T. P. Purdy, P.-L. Yu, R. W. Peterson, N. S. Kampel, and C. A. Regal. Strong optomechanical squeezing of light. Phys. Rev. X, 3:031012, Sep 2013.

[69] N. Kampel. Mirror at the end: position sensitivity with classical noise, 2015. Internal technical note.

[70] A M Jayich, J C Sankey, K Børkje, D Lee, C Yang, M Underwood, L Childress, A Petrenko, S M Girvin, and J G E Harris. Cryogenic optomechanics with a Si_3N_4 membrane and classical laser noise. New Journal of Physics, 14(11):115018, 2012.

[71] O. Wipfli. Membrane mirror etalons for cavity optomechanics. Master's thesis, ETH Zürich, 2015.

[72] Christina J. Hood, H. J. Kimble, and Jun Ye. Characterization of high-finesse mirrors: Loss, phase shifts, and mode structure in an optical cavity. Phys. Rev. A, 64:033804, Aug 2001.

[73] D.J. Wilson. Cavity optomechanics with high-stress silicon nitride films. PhD thesis, Caltech, 2012.

[74] I. Tittonen, G. Breitenbach, T. Kalkbrenner, T. Müller, R. Conradt, S. Schiller, E. Steinsland, N. Blanc, and N. F. de Rooij. Interferometric measurements of the position of a macroscopic body: Towards observation of quantum limits. Phys. Rev. A, 59:1038–1044, Feb 1999.

[75] Constanze H ohberger Metzger and Khaled Karrai. Cavity cooling of a microlever. Nature, 432:1002–1005, 2004.

[76] O. Arcizet, P.-F. Cohadon, T. Briant, M. Pinard, and A. Heidmann. Radiation-pressure cooling and optomechanical instability of a micromirror. Nature, 444:71–74, 2006.

[77] Thomas Corbitt, Yanbei Chen, Edith Innerhofer, Helge Müller-Ebhardt, David Ottaway, Henning Rehbein, Daniel Sigg, Stanley Whitcomb, Christopher Wipf, and Nergis Mavalvala. An all-optical trap for a gram-scale mirror. Phys. Rev. Lett., 98:150802, Apr 2007.

[78] J. D. Thompson, B. M. Zwickl, A. M. Jayich, Florian Marquardt, S. M. Girvin, and J. G. E. Harris. Strong dispersive coupling of a high-finesse cavity to a micromechanical membrane. Nature, 452(7183):72–75, 2008.

[79] S. Gr oblacher, J. B. Hertzberg, M. R. Vanner, G. D. Cole, Sylvain Gigan, K. C. Schwab, and M. Aspelmeyer. Demonstration of an ultracold micro-optomechanical oscillator in a cryogenic cavity. Nature Physics, 5:485–488, 2009.

[80] C. Yang. Progress toward observing quantum effects in an optomechanical system in cryogenics. PhD thesis, Yale University, 2011.

[81] B. Zwickl. Progress toward observation of radiation pressure shot noise. PhD thesis, Yale University, 2011.

[82] M. Underwood. Cryogenic optomechanics with a silicon nitride membrane. PhD thesis, Yale University, 2016.

[83] Nobel Media AB. `https://www.nobelprize.org/nobel_prizes/physics/laureates/1920/guillaume-bio.html`. Accessed: 5 October 2016.

[84] T. Kessler, C. Hegemann, C. Grebing, T. Legero, U. Sterr, F. Riehle, M. J. Martin, L. Chen, and J. Ye. A sub-40-mhz-linewidth laser based on a silicon single-crystal optical cavity. Nature Photonics, 6:687–692, 2012.

[85] P.-L. Yu, w T. P., and C. A. Regal. Control of material damping in high-Q membrane microresonators. Phys. Rev. Lett., 108:083603, Feb 2012.

[86] D. J. Wilson, C. A. Regal, S. B. Papp, and H. J. Kimble. Cavity optomechanics with stoichiometric sin films. Phys. Rev. Lett., 103:207204, Nov 2009.

[87] Arpan Roy and Murray D. Barrett. Fabrication of glass micro-cavities for cavity quantum electrodynamics experiments. Applied Physics Letters, 99(17), 2011.

[88] D Hunger, T Steinmetz, Y Colombe, C Deutsch, T W Hnsch, and J Reichel. A fiber fabryperot cavity with high finesse. New Journal of Physics, 12(6):065038, 2010.

[89] N. E. Flowers-Jacobs, S. W. Hoch, J. C. Sankey, A. Kashkanova, A. M. Jayich, C. Deutsch, J. Reichel, and J. G. E. Harris. Fiber-cavity-based optomechanical device. Applied Physics Letters, 101(22), 2012.

[90] Margot Phelps, GariLynn Billingsley, and Liyuan Zhang. First contact brush and pour application procedure. `https://dcc.ligo.org/LIGO-E1000079/public`. Accessed: 22 October 2016.

[91] P.-L. Yu, K. Cicak, N. S. Kampel, Y. Tsaturyan, T. P. Purdy, R. W. Simmonds, and C. A. Regal. A phononic bandgap shield for high-q membrane microresonators. Applied Physics Letters, 104(2):–, 2014.

[92] R.W. Andrews. Quantum signal processing with mechanical oscillators. PhD thesis, University of Colorado, Boulder, 2015.

[93] Tim Menke, Peter S. Burns, Andrew P. Higginbotham, Nir S. Kampel, Robert W. Peterson, Katarina Cicak, Raymond W. Simmonds, Cindy A. Regal, and Konrad W. Lehnert. Reconfigurable re-entrant cavity for wireless coupling to an electro-optomechanical device, 2017.

[94] K. Cicak, D. Li, J. Stong, M. Allman, F. Altomare, A. Sirois, J. Whittaker, J. D. Teufel, and R. W. Simmonds. Low-loss superconducting resonant circuits using vacuum-gap-based microwave components. Applied Physics Letters, 96:093502, march 2010.

[95] J. D. Teufel, Dale Li, M. S. Allman, K. Cicak, A. J. Sirois, J. D. Whittaker, and R. W. Simmonds. Circuit cavity electromechanics in the strong-coupling regime. Nature, 471(7337):204–208, 2011.

[96] Jeremy B. Clark, Florent Lecocq, Raymond W. Simmonds, José Aumentado, and John D. Teufel. Sideband cooling beyond the quantum backaction limit with squeezed light. Nature, 541:191–195, 2017.

[97] Amir H Safavi-Naeini, Jasper Chan, Jeff T Hill, Simon Grblacher, Haixing Miao, Yanbei Chen, Markus Aspelmeyer, and Oskar Painter. Laser noise in cavity-optomechanical cooling and thermometry. New Journal of Physics, 15(3):035007, 2013.

[98] Yi Zhao, Dalziel J. Wilson, K.-K. Ni, and H. J. Kimble. Suppression of extraneous thermal noise in cavity optomechanics. Opt. Express, 20(4):3586–3612, Feb 2012.

[99] Cryoconcept. `http://cryoconcept.com/products/hexa-hor-family/`. Accessed 21 March 2017.

[100] A. G. Kuhn, J. Teissier, L. Neuhaus, S. Zerkani, E. van Brackel, S. Delglise, T. Briant, P.-F. Cohadon, A. Heidmann, C. Michel, L. Pinard, V. Dolique, R. Flaminio, R. Tabi, C. Chartier, and O. Le Traon. Free-space cavity optomechanics in a cryogenic environment. Applied Physics Letters, 104(4):–, 2014.

[101] Rei Kitamura, Laurent Pilon, and Miroslaw Jonasz. Optical constants of silica glass from extreme ultraviolet to far infrared at near room temperature. Appl. Opt., 46(33):8118–8133, Nov 2007.

[102] William F. Kindel, M. D. Schroer, and K. W. Lehnert. Generation and efficient measurement of single photons from fixed-frequency superconducting qubits. Phys. Rev. A, 93:033817, Mar 2016.

[103] FiveNine Optics. `https://fivenineoptics.com`. Accessed: 21 March 2017.

[104] Advanced Thin Films. `http://advancedthinfilms.com/Products/High-Energy-Laser-Mirrors/CRD-Standard-Mirrors`. Accessed: 21 March 2017.

[105] R. W. P. Drever, J. L. Hall, F. V. Kowalski, J. Hough, G. M. Ford, A. J. Munley, and H. Ward. Laser phase and frequency stabilization using an optical resonator. Applied Physics B, 31(2):97–105, 1983.

[106] Eric D. Black. An introduction to pounddreverhall laser frequency stabilization. American Journal of Physics, 69(1):79–87, 2001.